



Dissertation
2011 - 10
November

**Beam Loading Effect and
Adiabatic Capture in SIS-18 at GSI**

Tripti Shekhar Mohite,

(Dissertation der Technischen Universität Darmstadt)

GSI Helmholtzzentrum für Schwerionenforschung GmbH
Planckstraße 1 · D-64291 Darmstadt · Germany
Postfach 11 05 52 · D-64220 Darmstadt · Germany

Beam Loading Effect and Adiabatic Capture in SIS-18 at GSI

Vom Fachbereich Elektrotechnik und Informationstechnik
der Technischen Universität Darmstadt
zur Erlangung des akademischen Grades einer
Doktor-Ingenieurin (Dr.-Ing.) genehmigte

Dissertation

von

Tripti Shekhar Mohite, M.Tech.

Geboren am 15. Juli 1975 in Gwalior, India

Referent: Prof. Dr.-Ing. T. Weiland
1. Korreferent: Prof. Dr.rer.nat. O. Boine-Frankenheim
2. Korreferent: PD Dr. P. Hülsmann

Tag der Einreichung: 15.10.2010

Tag der Verteidigung: 20.01.2011

D17
Darmstadt 2011

Dedicated to My Family

*The End of Education is Character
The End of Culture is Perfection
The End of Knowledge is Love
The End of Wisdom is Freedom
- BABA*

Abstract

For the projected Facility for Antiproton and Ion Research (FAIR) at GSI the upgraded, existing synchrotron SIS-18 will be used as an injector. The increased beam intensity in the upgraded SIS-18 is expected to cause additional collective effects, leading to beam loss or beam quality degradation.

Beam interaction with radio frequency (rf) cavity, resulting in beam loading effect, is an important consideration in the design and operation of high-intensity circular particle accelerators. The steady state and transient perturbation of the rf cavity system by the circulating beam can be harmful to the beam and limit the accelerator performance. Steady state beam loading effect is observed in SIS-18 with single and double rf operations. The supportive simulation and theoretical study is done, to extrapolate the results for the upgraded SIS-18.

In SIS-18 the coasting beam, i.e. an unbunched dc beam, is captured by using the rf cavities. RF capture is one of the potential sources for longitudinal beam quality degradation at high intensities. Therefore this part of the SIS-18 machine cycle requires dedicated studies. The rf voltage ramping time and the initial voltage amplitude are important parameters to be controlled. This study of longitudinal beam dynamics is helpful to determine the optimum type of voltage ramp, in terms of beam quality and total cycle time. A theoretical study has been made in this direction, supported by simulations. In line with that the experiments have been performed in SIS-18.

Kurzfassung

Für das geplante internationale Beschleunigerzentrum für die Forschung mit Ionen- und Antiprotonenstrahlen (FAIR: Facility for Antiproton and Ion Research) an der GSI soll der schon existierende aber modernisierte Synchrotron SIS-18 als Injektor verwendet werden. Es wird erwartet, dass die erhöhte Strahlintensität im modernisierten SIS-18 zusätzliche kollektive Effekte verursacht, die zu Strahlverlust und Minderung der Strahlqualität führt. Wechselwirkungen des Strahls mit der Radiofrequenz- (RF-) Kavität führen zu einem Beam-Loading Effekt, der einen wichtigen Einfluss auf das Design und den Betrieb von Synchrotrons hat, die mit hohen Strahlintensitäten arbeiten. Die stationären und dynamischen Störungen des Kavitätensystems durch den zirkulierenden Strahl können sich nachteilig auf diesen auswirken und limitieren die Effizienz des Beschleunigers. Der stationäre Beam-Loading Effekt wird im SIS-18 im Zusammenhang mit einfach- und doppelharmonischen Operationen beobachtet. Simulationen und theoretische Untersuchungen wurden durchgeführt, um die Ergebnisse der Maschinenexperimente am existierenden SIS-18 auf den modernisierten zu extrapolieren. Im SIS-18 wird der ungebunchte DC Strahl („coasting beam“) durch Radiofrequenzkavitäten gebuncht. Dieser RF-Einfang ist einer der potentiellen Quellen für die Minderung der longitudinalen Strahlqualität bei hohen Intensitäten. Aus diesem Grund muss dieser Teil des Maschinenzyklus genau untersucht werden. Die Anstiegszeit der RF-Spannung und die anfängliche Spannungsamplitude sind dabei wichtige Kontrollparameter. Die Untersuchung dieses Teils der longitudinalen Strahldynamik hilft die optimale Spannungsrampe zu bestimmen, um die optimale Strahlqualität und Umlaufzeit zu erhalten. Theoretische Untersuchungen wurden in dieser Richtung gemacht, um die Simulationen zu bestätigen. Zusätzlich wurden Maschinenexperimente am bestehenden SIS-18 durchgeführt.

Contents

1	Introduction	1
2	GSI and FAIR: An Overview	5
2.1	Accelerator facility at GSI	5
2.2	Heavy-ion synchrotron (SIS)	7
2.3	SIS accelerating cavity	9
2.3.1	Working principle	10
2.3.2	Simplified circuit representation	12
2.3.3	Control loops	15
2.4	FAIR: Motivation behind SIS upgrade program	17
3	Longitudinal Beam Dynamics	21
3.1	Particle acceleration in SIS cavity	21
3.2	Longitudinal equation of motion	23
3.2.1	The Hamiltonian	26
3.2.2	Stationary bucket	28
3.3	Particle distribution	28
3.3.1	Emittance	30
3.3.2	Filamentation and Emittance blowup	32
3.3.3	Double rf System	33
4	Longitudinal Intensity Effects	35
4.1	Longitudinal beam loading	36
4.1.1	Cavity detuning and beam stability	37
4.1.2	Steady-state beam loading	39
4.1.3	Transient beam loading	40
4.2	Longitudinal space charge effect	40
4.3	Voltage induced by a stationary bunch	42
4.4	Longitudinal impedance and coasting beam	43
4.5	Potential well distortion	45
4.5.1	Single rf bucket	46
4.5.2	Double rf bucket	48
4.6	Simulation programme	50

5	Longitudinal Beam Diagnostics in SIS	53
5.1	DC Transformer	53
5.2	Beam position monitor	57
5.3	Schottky pick-up	60
5.4	Digital Signal Processor System	62
6	Adiabatic Capture in SIS	63
6.1	Principle of capture study	63
6.1.1	RF amplitude ramps and dilution factor	64
6.1.2	Initial voltage and momentum spread	67
6.2	Capture measurements	69
6.2.1	Measurement method	70
6.2.2	Settings of parameters	71
6.2.3	Simulation settings	73
6.3	Observation and results	74
6.3.1	Single rf system	74
6.3.2	Double rf system	81
6.3.3	Upgraded SIS	83
7	Beam Loading Measurements	85
7.1	Principle of measurement	85
7.2	Measurement method and instruments	87
7.3	Settings of the parameters	90
7.4	Observations and results	92
7.4.1	For single rf system	92
7.4.2	Double rf system	104
7.4.3	For upgraded SIS	108
8	Summary and Outlook	111
A	Symbols and Abbreviations	115
B	Test Cavity Measurements	121
B.1	Experimental set-up	121
	Bibliography	125
	Acknowledgement	133
	Curriculum vitae	135

List of Figures

2.1	Accelerators and experimental areas at GSI	6
2.2	A principle diagram of SIS ring	7
2.3	A section of SIS ring	7
2.4	An rf frequency and amplitude cycle in SIS	8
2.5	Basic assembly of an rf system with beam	9
2.6	A 3D-model and principle diagram of ferrite cavity in SIS	11
2.7	An approximate equivalent circuit of a cavity	13
2.8	Real and imaginary impedance of ferrite cavity	14
2.9	Block diagram for the amplitude control loop	15
2.10	Block diagram for resonance frequency control loop	16
2.11	Schematic view of FAIR	17
3.1	Demonstration of SIS cavity gap	22
3.2	Demonstration of particle revolution in a synchrotron ring	24
3.3	Demonstration of particle trajectories	27
3.4	An example of a particle distribution in bunch	29
3.5	Illustration of the coasting and bunched beam	31
3.6	Demonstration of filamentation and emittance blowup	32
3.7	RF voltage waveforms for single and double rf systems	33
3.8	A stationary bucket and flattened bunch in drf system	34
4.1	A parallel equivalent circuit of rf cavity with beam	36
4.2	Phasor representation of detuning of cavity	37
4.3	Robinson's stability region in resonance curve of cavity	39
4.4	Radial and longitudinal fields by the beam particles	41
4.5	Keil-Schnell limit and longitudinal impedances in SIS	45
4.6	Numerical solution of bunch form with beam loading effect	47
4.7	Theoretical bunch form with intensity effects in drf system	49
4.8	Bunch form in drf bucket, from numerical solution and simulation	51
5.1	Principle diagram of CT and a photograph of CT in SIS ring	54
5.2	An example of beam intensity recorded in main control room	55
5.3	An example of beam intensity recorded in rf experiment hall	56
5.4	Principle diagram of longitudinal beam pick-up	57
5.5	A BPM in SIS and its conceptual diagram	58

5.6	The Electronic scheme for longitudinal beam pick-up	58
5.7	A photograph of Schottky pick-up in ESR	60
5.8	The electronic scheme for Schottky pick-up	61
5.9	Block diagram of a DSP system in SIS	62
6.1	Different rf voltage amplitude ramps, tested in capturing measurements	65
6.2	Demonstration of phase space with coasting, bunched beams and rf bucket	67
6.3	Simulation showing dependence of DF on coasting beam	68
6.4	Simulations relating the DF with χ	69
6.5	A schematic diagram for the capturing measurements	70
6.6	A block diagram showing the signals measured by using oscilloscope	71
6.7	An example of rf cycle for capture study with srf system	72
6.8	An example of rf ramps for the cavities (h=4, 8) in drf system	73
6.9	Measured Schottky and BPM signals from beam, for srf operation	74
6.10	Measurements showing variation in the DF with t_{ramp}	75
6.11	Simulation showing variation in σ_{rms} t_{ramp}	75
6.12	Bunch forms, from measurements and simulations, for different t_{ramp}	76
6.13	Bunch evolution with time for different ramps	77
6.14	Bunch oscillations, observed in measurements	77
6.15	Influence of frequency and energy mismatch on σ_{rms}	78
6.16	The measurements and simulations, showing increase in σ_{rms} with V_i	79
6.17	Measured bunch form and its evolution with time for V_i of 800 V	80
6.18	Measured Schottky and BPM signals from beam, for drf operation	81
6.19	Measurements and simulations showing variations in ϕ_m with t_{ramp}	82
6.20	Bunch forms, from measurements and simulations, for different t_{ramp}	82
6.21	Measured bunch evolution with time	83
6.22	Simulated bunch length, with intensity effects, in upgraded SIS	84
7.1	The cavity settings for beam loading measurements	86
7.2	Schematic diagram for the measurement of beam loading effect	88
7.3	A block diagram showing the signals recorded by an oscilloscope	89
7.4	RF amplitude ramp for driving cavity in srf system	91
7.5	Measured beam and gap signals from both cavities, in srf operation	92
7.6	Measured bunch forms and frequency components in a bunch	93
7.7	Measured Schottky signal from the coasting beam	93
7.8	The screen shots from the DSP system for gap measurements	94
7.9	The measurements and simulations showing variations in V_b with V_0	96
7.10	The measurements and simulations, showing variations in σ_{rms} with V_0	97
7.11	V_b normalized to ppc for different machine and beam settings	97
7.12	The bunch forms from the simulation and measurement	98
7.13	V_b normalized to ppc for upgraded beam intensity	99
7.14	Measured shunt impedance of the open cavity	99
7.15	Phase relation between I_{rf} and rf voltage V_{rf}	100

7.16	Measured bunch evolution with beam loading effect	100
7.17	Measured response of controller in amplitude control loop	101
7.18	Measured relation between the V_0 and R_s of the driving cavity	102
7.19	The measured variations in I_{bias} in RFCL with V_0	103
7.20	The variations in V_b with respect to V_0 in drf operation	105
7.21	The measured variations in ϕ_m with the V_0 in drf operation	105
7.22	V_b normalized to ppc for drf operation	106
7.23	Frequency components in the bunch with drf operation	106
7.24	Bunch forms, from measurement, simulation and theory, in drf operation .	107
7.25	The simulated V_b with the drf system (h= 2, 4) in upgraded SIS	108
7.26	The simulated bunch form with drf system (h= 2, 4) in upgraded SIS . . .	109
B.1	Block diagram for a measurement on test cavity	122
B.2	Measured variations in cavity parameters with I_{bias}	122

List of Tables

2.1	Some facts about existing SIS	8
2.2	Technical parameters of SIS ferrite cavity	10
2.3	Some parameters of ferrite and compressor cavities	14
2.4	Beam and machine parameters in upgraded SIS	18
2.5	Some parameters of harmonic 2 cavity	19
3.1	Parameters for a non-synchronous particle	23
4.1	Beam, machine and cavity parameters for beam stability	44
4.2	Beam loading parameter, α_{bl} and phase shift, ϕ_{bl} for single rf operation . .	47
4.3	Beam loading, space charge and intensity parameters for double rf operation	49
6.1	Machine, beam and rf parameters settings for capturing measurements . .	72
6.2	The χ for different V_i for the same rf amplitude ramp	79
6.3	Simulation parameters for capture in upgraded SIS	83
7.1	Machine, beam and rf parameters settings for beam loading measurements	90
7.2	Measurement results for open cavity in srf operation	95
7.3	Settings of cavity parameters in simulations for srf operation	96
7.4	Measurement results for driving cavity in srf operation	102
7.5	Measurement results for bunch compressor cavity in drf operation	104
7.6	The simulation settings of cavity parameters for drf operation	106
7.7	Intensity parameter in drf measurements	107
A.1	List of symbols	115
A.2	List of abbreviations	119
B.1	Summary of the measurement results on test cavity	123

Chapter 1

Introduction

The matter that surrounds us turns out to be a hierarchy of visible scale of materials to elementary components of atomic nuclei. Composition of these materials can be studied by bombarding their samples with high-energy ion beams. In the most basic sense, high-energy accelerators represent the man-made machines which provide the possibility to attain those required energy levels in the laboratory environment. Since 1932, specially during the course of last fifty years, the continuous advancements in technology has accentuated the developments in the accelerators [1]. As an evidence, the flux of the intense beam generated in the modern accelerators, is far stronger than the flux of natural source of high-energy particles like cosmic rays. Several pioneering works, such as study of evolution of matter in the universe, discovery of new elements and precise radiotherapy for treatment of complex tumor etc, provide a glimpse on the wide range of promising discoveries that could be possible with modern accelerators and storage rings. Further research and advancement in this direction are mainly based on the supply of high intensity and high quality beams.

Gesellschaft für SchwerIonenforschung (GSI) [2] in Darmstadt, Germany, is an accelerator facility providing beams from light to heavy ions for experiments in various research areas. The planning and preparations for the new international Facility for Antiproton and Ion Research (FAIR) [3, 4], besides this existing facility, are in progress. As per the proposed plan, the linear accelerator and SchwerIonenSynchrotron (heavy-ion synchrotron), SIS-18 [5] at GSI, with modified parameters [6], will be used to inject a high-quality and high-intensity particle beam to the FAIR synchrotron rings [3].

In a synchrotron, the charged particle beam is guided and focused by transverse magnetic field. This field is generated by several types of magnetic elements cascaded in the vacuum chamber of the synchrotron ring. Beam acceleration is effectuated by an alternating longitudinal electrical field [7, 8, 9] generated in the radio frequency (rf) resonator, known as rf cavity, which is excited by a rf power generator. The interaction of the charged particles with the beam surroundings, like vacuum chamber, cavities etc., and with each other are among the limiting factors for the beam intensity [10, 11, 12].

The particle beam passes through the cavity multiple times and attains the desired level of acceleration [14, 15]. While crossing the cavity the beam induces an electromagnetic field in it, thereby creating a decelerating voltage acting on the beam in return. This mutual

effect associated with beam and cavity interaction is known as **beam loading** [16, 17]. It is one of the several current-dependent effects and represents one particular example of the general problem of interaction between electromagnetic fields generated by the beam and its surroundings, in this case cavity impedance [18, 19].

The beam loading involves the beam-induced perturbations in the rf cavity system since it affects the amplitude as well as phase of the cavity voltage [21, 22]. They in turn affect the beam and lead to undesirable beam behavior, like onset of beam instabilities or partial/total particle loss due to an insufficient longitudinal acceptance [8, 12]. Its influence on the beam quality i.e. the area occupied in the longitudinal phase space, is much more visible in case of high-intensity beam. Beam loading causes the cross-coupling between the inherent control loops in the rf system [21, 23], which at high beam loading makes the system unstable.

The study of the beam loading effect in an accelerator should ideally begin with probing the type of the beam loading. It depends upon the properties of the beam as well as cavity. Among several other factors [16, 21, 22], key determinants for the type of beam loading are 1. the pattern of bucket filling; 2. beam intensity and the frequency variations; 3. bunch length and the decay/rise time of cavity. While the steady state beam loading can be compensated by adjusting the detuning [25, 26], the effective compensation of the transient beam loading requires a specially designed low-level rf system [22, 23, 24].

At GSI, for a cooled bunch in the Experimental Storage Ring (ESR) the beam loading effect has already been studied [28, 29]. *This work is the first attempt to study the influence of beam loading on the cavity, and on the longitudinal beam dynamics in SIS-18.*

SIS-18 contains two similar ferrite cavities. Both of these operate at the same frequency, i.e. harmonic four ($h=4$) of the revolution frequency, and form the single rf operation [30]. For a precise estimation of the beam loading knowledge about cavity behavior, specially its resonance settings and the shunt impedance [31, 32], is essential. It is specifically true for the ferrite cavity as its magnetic properties vary with the amplitude of the rf voltage [31, 33]. A prototype of the SIS-18 ferrite cavity is easily accessible. It is exactly similar to the SIS-18 cavity, except the lower capacity of its power supply unit [36]. To develop further understanding about the cavity behavior, several experiments have been performed on the prototype cavity.

Using these experimental results from the prototype cavity as a reference along with an understanding developed about the required longitudinal beam diagnostics, the arrangements are made to conduct the precise measurements of the beam loading effect. These measurements are performed to examine its influence on beam, on the amplitude and phase of the gap voltage and on the stability of the amplitude and resonance frequency control loops [37, 38]. *Along with the beam loading, the impedance observed by the beam for the whole working range of the amplitude of rf voltage has been calculated through the measurements.*

In the present SIS-18 the steady-state beam loading is observed. The available theory in this regard [10, 11, 17] is modified, as per the requirement, for the specific conditions in SIS-18. The entire work is supported by the simulation study performed in a fortran based particle-in-cell code ESME [39, 40]. This code facilitates the study of the longitudinal

beam dynamics under different settings of the rf system. The high-intensity effects have been accurately included in it [41, 42].

Along with the present SIS-18, in-depth study and analysis of the beam loading deserves a special attention in SIS-18 upgrade programme for FAIR. As per the proposed upgrade plan, along with the higher beam intensity the SIS-18 rf system is to be upgraded from the single to double rf system [7, 44] from the stability point of view. In double rf system, two different rf harmonics ($h=2, 4$) are planned to create the flat potential well leading to a flat bunch. Thus the maximum density in the bunch-center gets reduced [45, 46]. Also, the nonlinearity created by the longer bunches in a dual rf bucket increases the well known Landau damping [49]. Hence, a bunch in a dual rf bucket is more stable. A broad-band Magnetic-Alloy (MA) cavity ($h=2$) is planned [50, 51] to form a double rf system with one of the present ferrite cavities ($h=4$) in SIS-18. With the $h=2$ cavity, a transient beam loading may appear. *This work estimates the beam loading effect with the planned broad-band cavity, on the basis of the agreement of the simulation and the theoretical solution with the measurements in the present SIS-18.*

The influence of the electromagnetic field, produced by the mutual interaction among the beam particles, on the beam parameters is known as the **space charge effect** [52, 53, 54, 55]. A **longitudinal impedance** including the influence of the beam loading and space charge effects is defined. The interaction of a stationary bunch with this longitudinal impedance results in the potential well distortion [10, 11]. This potential well distortion in the form of a slant, in the middle of the particle distribution, is theoretically defined in this work. Its results are supported by the simulations.

The whole beam loading study is performed for the bunched beam at injection energy, and the coasting beam at injection is captured by ‘switching ON’ the rf voltage. To estimate the influence of the beam loading on beam quality [56, 57], the stability of the coasting or unbunched particle beam must be assured and any emittance blowup or the filamentation [58, 59, 60, 61] in the beam capturing process must be prevented.

Several studies have been performed at GSI to propose the case of stability of a cooled coasting beam [28, 29, 62] and a case-study for the coasting beam in SIS-18 is in progress [63]. *In this report, the stability of the coasting beam interacting with the longitudinal impedance is studied by inspecting the Keil-Schnell limit [11] in the present as well as for the upgraded SIS-18.*

The **adiabatic capture** prevents the influence of the capturing process on the longitudinal beam phase space area and plays a vital role in ensuring the efficient capturing and quality of the beam. In the adiabatic capturing of the coasting beam, the amplitude of rf voltage (at constant frequency) must be increased gradually to form a bunch structure so that the parameters of synchrotron motion are changed slow enough to keep the distribution of particles at equilibrium throughout the capture process. In SIS-18, there is a rapid bunch formation within ≈ 2 ms. This is nearly twice of the synchrotron period at injection. For adiabatic capture, the capturing time should certainly be more than the current value. But its upper limit is restricted by the limited machine cycle. As per the SIS-18 upgrade plan, this machine cycle will be decreased in order to increase the frequency of particle extraction. Within this faster machine cycle, ≈ 20 ms is the time assigned for

the beam capturing. The meticulous design of rf amplitude ramp parameters, like time for full ‘Turn-ON’ and the voltage amplitude vs time function [59], greatly enhances the possibility of adiabatic capturing. Therefore, *an optimization of these ramp parameters is the major objective of the capture study.*

In case of SIS-18, a minimum biasing essential for the activation of the electronics in rf systems sets a lower limit on the initial voltage of the rf amplitude ramp, approximately 100 V. *A scaling factor, relating the initial voltage with the momentum spread of the coasting beam, is introduced.* Above the threshold value of this scaling factor, the adiabatic capture for the given coasting beam parameters is ensured.

In summary, *this work is devoted for the measurements of the beam loading effect in the present SIS-18. Alongside, the measurements are performed to optimize the rf amplitude ramp parameters for the adiabatic capture of the coasting beam. Both of these measurement studies are supported by the theoretical as well as simulation work, and on the basis of their agreement the predictions are made for the upgraded SIS-18.*

This report is organized as follows:

The subsequent chapter gives an overview about GSI along with some important parameters. Then the relevant details about SIS-18 and rf system, specially ferrite cavity, along with its upgrade plan have been explained.

Chapter 3 explains some relevant concepts about longitudinal beam dynamics like Hamiltonian formalism, principle of phase stability etc.

Chapter 4 introduces intensity effects, their equivalent longitudinal impedance and the potential. Then the stability of the coasting beam and the theory about the potential well distortion in bunched beam is discussed. Then the simulation code ESME is introduced along with an example comparing bunch from theory and the simulations are presented.

Chapter 5 explains the longitudinal beam diagnostics adapted for the capturing and beam loading measurements in SIS-18.

Chapter 6 is explaining the adiabatic capture and its measurements in SIS-18. Here the experimental results are compared with the simulation studies.

Chapter 7 is dedicated to the beam loading measurements. Here the simulation results are also presented in support of the measurements.

Chapter 8 provides the conclusions derived from the above mentioned studies. And a brief discussion about the future possibilities is presented.

Chapter 2

GSI and FAIR: An Overview

The “GSI Helmholtzzentrum für Schwerionenforschung” (Helmholtz center for heavy ion research) is an accelerator facility established in year 1969 in Darmstadt, Germany. It is funded by the Federal Republic of Germany and by the state of Hesse. The facility offers the capability to accelerate ions over a wide range of masses and charges, ranging from protons to Uranium, to velocities approaching the speed of light.

This chapter will help to lay the foundation in order to provide certain relevant insights revolving around the central theme of this work. The existing accelerator facility at GSI is briefed in the beginning, in Sec. 2.1. Then Sec. 2.2 highlights some technical as well as physical parameters of SIS, followed by the description of the rf system in SIS. Thorough understanding of cavity behavior is imperative for precise estimation of beam loading. Therefore, a detailed discussion about ferrite cavity in SIS is presented in subsequent section. The upcoming FAIR facility, which is the primary motivation behind the SIS upgrade plan, and the SIS upgrade plan are briefly presented in Sec. 2.4.

2.1 Accelerator facility at GSI

A schematic view of the GSI is shown in Fig. 2.1. The facility can be broadly divided into three major parts.

- UNiversal Linear ACcelerator (UNILAC)
- Heavy ion synchrotron (SchwerIonen Synchrotron, SIS-18 or SIS)
- Experimental Storage Ring (ESR)

After the first bending section for charge and mass separation, the ions, produced from different ion sources, travel through the 120 m long UNILAC and achieve a velocity of approximately 20% of the speed of light [2]. The UNILAC delivers beams with energies in the range from 3 to 13 MeV/u for heavy ions, with u as the universal atomic mass unit, and up to 15 MeV/u for light ions. This range of energy is set differently by simply choosing different phase relation between the field oscillating in subsequent rf cavities. Its

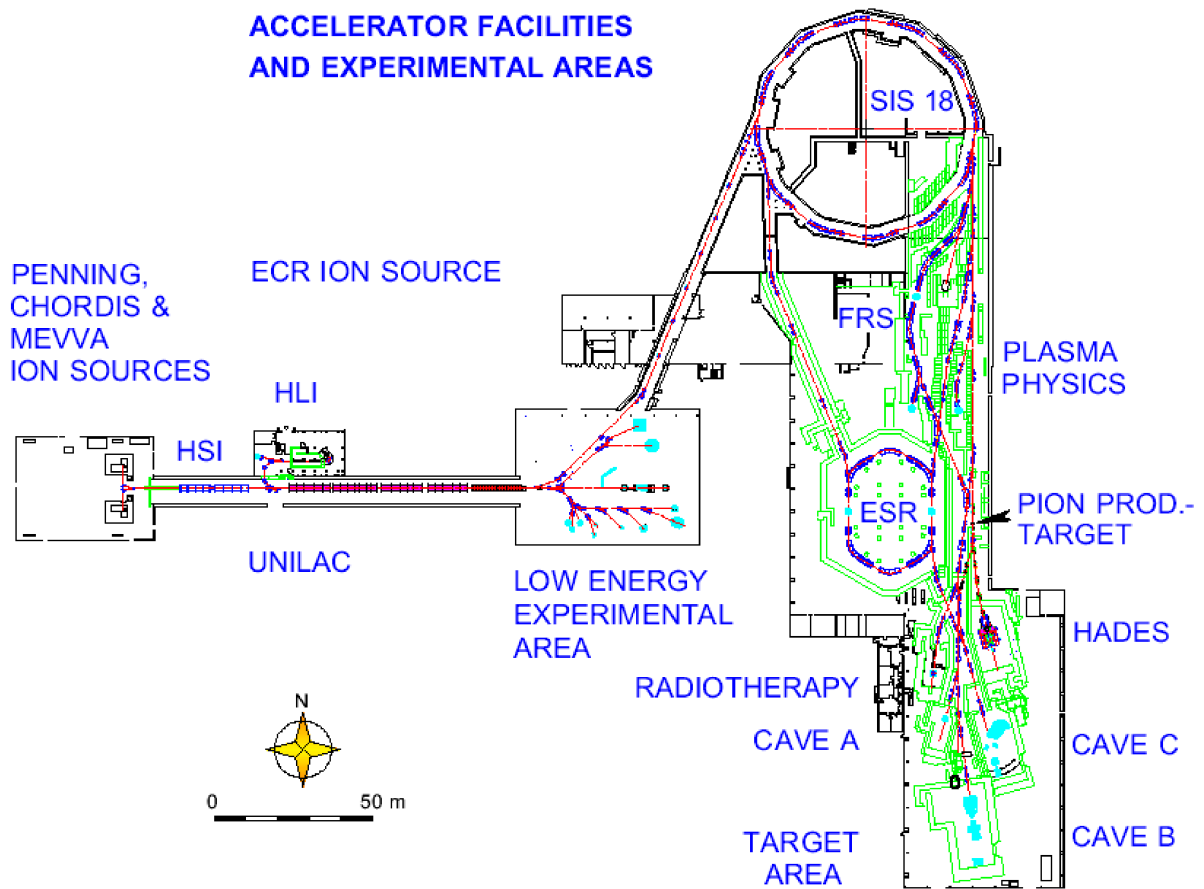


Figure 2.1: Accelerators and experimental areas at GSI. Starting from the left, the ion sources are followed by the UNILAC. The beam is transferred from the low-energy areas to the SIS through the transfer channel. The extracted beam from the SIS is available for experiments in Fragment Ring Separator (FRS), plasma physics, ESR, radiotherapy and various scattering experiments (HADES). This beam can further be extracted or dumped to different caves (Cave A, B and C).

first section is the pre-stripper linac. The present 36 MHz high current pre-stripper has replaced the 25 year old 27 MHz Wideroe type linac in 1999. Besides the energy, pulse strength, repetition frequency and intensity can be chosen individually. The standard energy of the injected beam from the UNILAC to SIS-18 is 11.4 MeV/u. Stripping in a carbon foil before beam entry into the SIS-18 gives 73^+ as the most abundant state of Uranium. These pre-accelerated ions from the UNILAC are injected into the SIS-18 with horizontal multi-turn injection scheme and then further accelerated in SIS up to 90% of the speed of light. The energy of the accelerated ions in the SIS, at magnetic rigidity 18 Tm, lies in the range from 1 GeV for U^{73+} to 4.5 GeV for protons. These high-energy ions

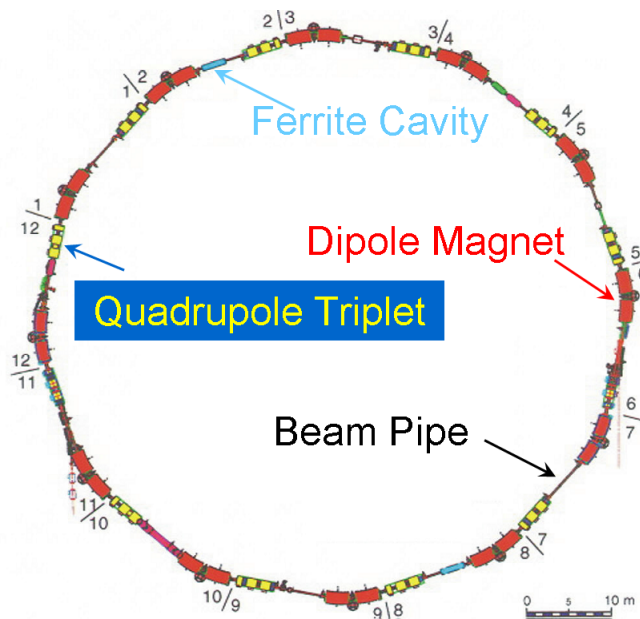


Figure 2.2: A principle diagram of SIS ring. Different components, as mentioned in Table 2.1, are distributed along the circumference of the ring. Two accelerating cavities (called as S02BE1 and S08BE2) are in section 2 and 8 respectively.

from SIS can be extracted to different experimental areas by slow extraction or delivered to ESR by fast extraction. At constant energy, it can be accumulated or stored in the SIS or ESR for several hours.

2.2 Heavy-ion synchrotron (SIS)

The heavy-ion synchrotron with the circumference of 216.72 m consists of 12 identical lattice sections, as shown in Fig. 2.2. Each section is equipped with two dipoles, one

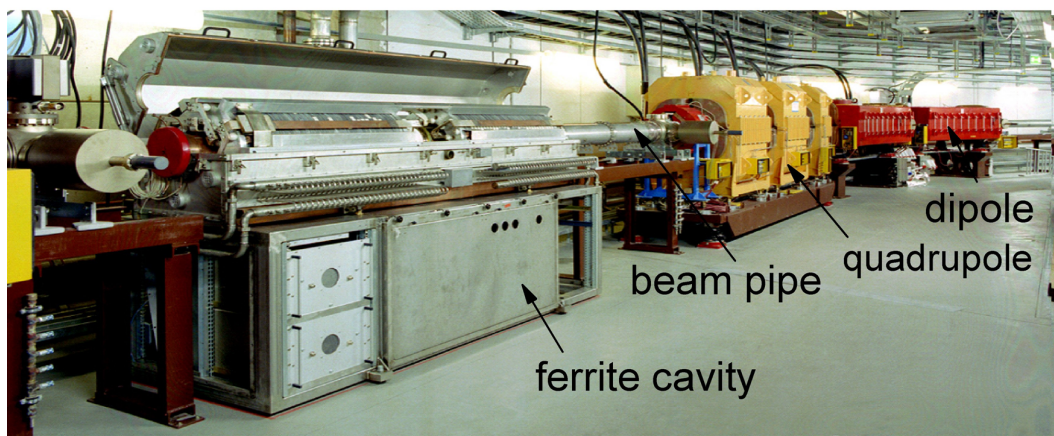


Figure 2.3: A picture showing section 2 of SIS ring (Fig. 2.2) in the tunnel. It shows the beam pipe, accelerating cavity, a quadrupole triplet and a dipole duplet.

Maximum bending power	18 Tm
Magnets	24 Dipoles, 1.8 T 12 Quadrupole triplet lenses 12 Sextupole lenses
Magnet Power	Dipoles 3.6 kA at 12 kV Field Ramp 10 T/s
Rf Acceleration	2 Cavities with maximum voltage, 16 kV Frequency Span 0.8-5.6 MHz
Vacuum	operational 10^{-10} Torr bakable to 300°C
Beam Diagnostics	12 Position Monitors 2 Phase Probes 1 DC Transformer 1 fast and 1 slow Pulse Transformers 1 Beam Scraper 1 Residual Gas Monitor

Table 2.1: Some facts about the existing SIS. The beam diagnostic instruments and components are distributed along the SIS circumference.

quadrupole triplet and one sextupole along with two identical ferrite cavities in sections 2 and 8 (Fig. 2.3). Table 2.1 displays key features and components of SIS [5].

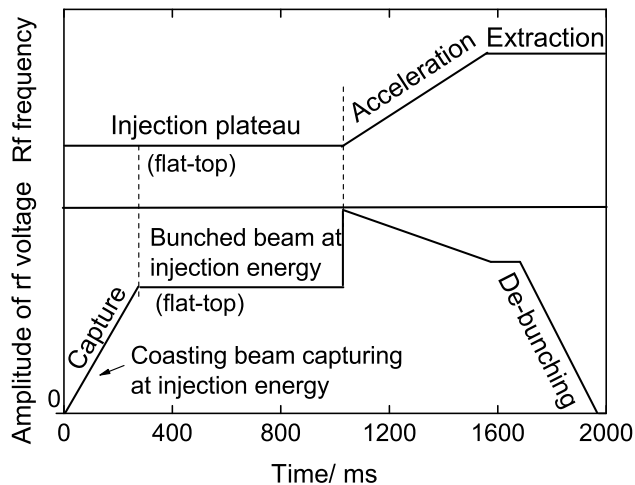


Figure 2.4: An example of rf frequency and amplitude cycle in SIS. It indicates a constant energy for the whole injection plateau and that the coasting beam from the UNILAC is captured at the injection energy.

The bunched beam from the UNILAC is injected into the SIS. As no rf voltage is applied in SIS at this instant, it appears here as continuous dc beam, called as coasting beam. This coasting beam is captured in SIS by switching on the rf voltage. The SIS rf cycle has different steps of injection, capture, acceleration, de-bunching and extraction (Fig. 2.4). The period between beginning of injection and of acceleration is called injection plateau. During the multi-turn injection, an ion-pulse, with a duration of 1 to 400 μs , is injected from UNILAC to SIS. To increase the beam intensity (ppc), multi-multi turn injection is performed by injecting several pulses per cycle. Capture is followed by acceleration, which is achieved by increasing the rf frequency. Here the rf amplitude is decreased to keep the size of the rf-bucket [7] constant. After acceleration, the beam can be extracted fast at same energy or frequency. And the another possibility is slow extraction, where beam is de-bunched by slowly decreasing the rf amplitude followed by extraction to some experimental hall.

2.3 SIS accelerating cavity

In an accelerator, a controlled acceleration of the charged particles requires a continuous energy transfer through an external source. To fulfill this requirement, the electric field

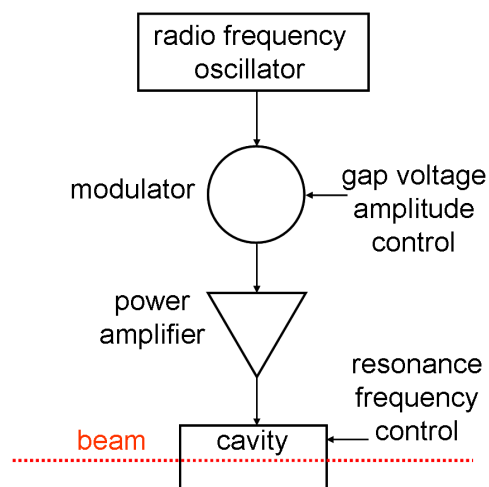


Figure 2.5: The simple rf assembly with its basic control system and beam. The controlled rf power (at certain frequency) from rf oscillator is amplified by the power amplifier and transferred, through a cavity gap, to the beam.

in a synchrotron is needed in the direction of motion of the particles. This electric field, produced by the rf system, imparts the energy to the beam through the rf cavity [32, 34].

A minimum rf installation, as shown in Fig. 2.5, is a simple power amplifier assembly where the cavity is excited by the signal from an oscillator. Different feedback loops are required to control the frequency and amplitude of the rf signal from the beam stability

point of view [17, 20, 22, 23]. The frequency of the oscillator signal is to be accurately controlled so as to center the beam in the beam pipe. It is to be adjusted, along with the signal amplitude, as per the requirements of the rf cycle (Fig. 2.4).

2.3.1 Working principle

Rf system in SIS consists of two identical ferrite accelerating cavities [37] placed in diagonally opposite sections as shown in Fig. 2.2. Recently, a new Magnetic Alloy (MA) cavity, with the purpose of bunch compression, is installed [50, 67] in section 2 of the SIS ring.

- Ferrite persists a wide range of magnetic, electrical and mechanical properties. It provides a reliable and flexible means of tuning particle accelerator rf cavities with efficient use of power [33].
- SIS accelerating cavity consists of two identical coaxial line, quarter-wave, ferrite filled resonators [31, 32, 34]. Technical parameters of the cavity are explained in Table 2.2.

Rf peak accelerating voltage	V_0 / kV	16
Core material	–	Philips FXC8C12 mod
Relative permeability	μ_r	500 to 1000
Number of ferrite rings	N_{ring}	2×32
Number of bias windings turns	$N_{winding}$	6
Bias current range	I_{bias} / A	8 to 800
Dimensions of ferrite rings	$D_0/D_i/t$ / mm	498/ 270/ 25
Cavity length	L_{cav} / m	3.2
Type of power amplifier	Power tetrode	Siemens RS 2054SK
RF power from power amplifier	P_{cav} / kW	50
Maximum rf (anode) current	I_a / A	6.5
Rf input to power amplifier	$V_{pp}/ P_{rf}/ f_{rf}/ V/ W/ MHz$	230(peak to peak)/500/0.8 to 5.6

Table 2.2: Technical parameters of SIS ferrite cavity in Fig. 2.6.

- An increased inductance in ferrite cavity, as compared to an air-filled cavity (with same dimensions), is achieved at the cost of increased core or rf losses [31, 33], mainly eddy current and hysteresis losses. Here the ferrite cores are laminated to reduce the eddy current loss.
- Both, dc bias and rf windings can be seen in the principle diagram in Fig. 2.6. A dc current in the bias windings, called bias current, is varied to adjust the operating point on the hysteresis curve such that the ferrite stores energy through the domain rotation alone [31]. This way the hysteresis losses can be reduced effectively.

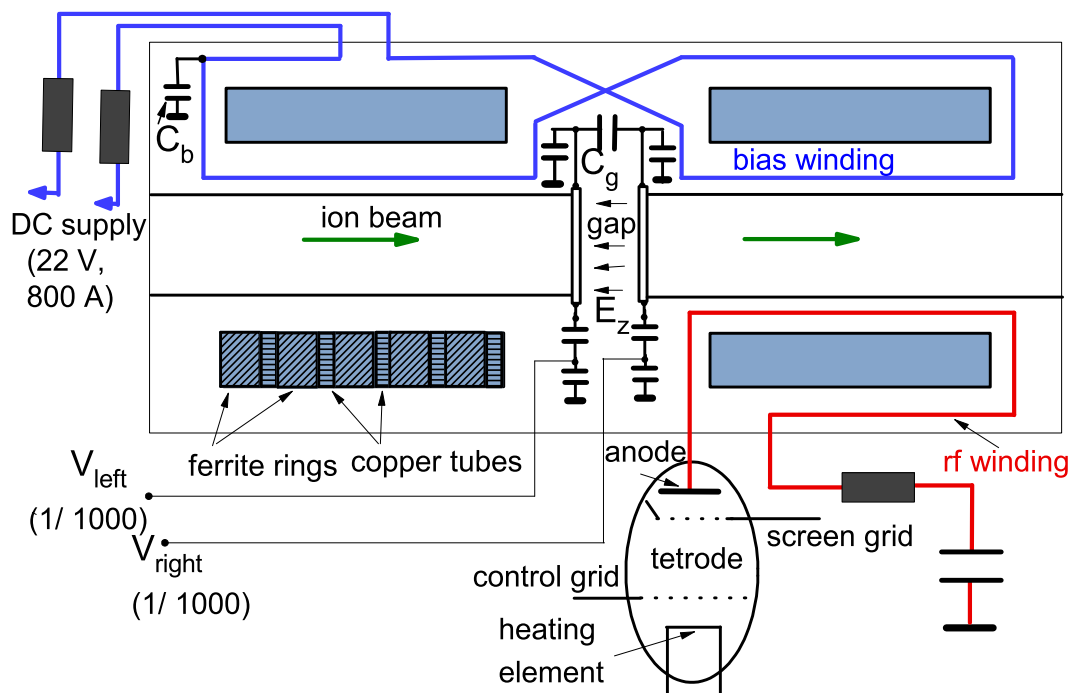
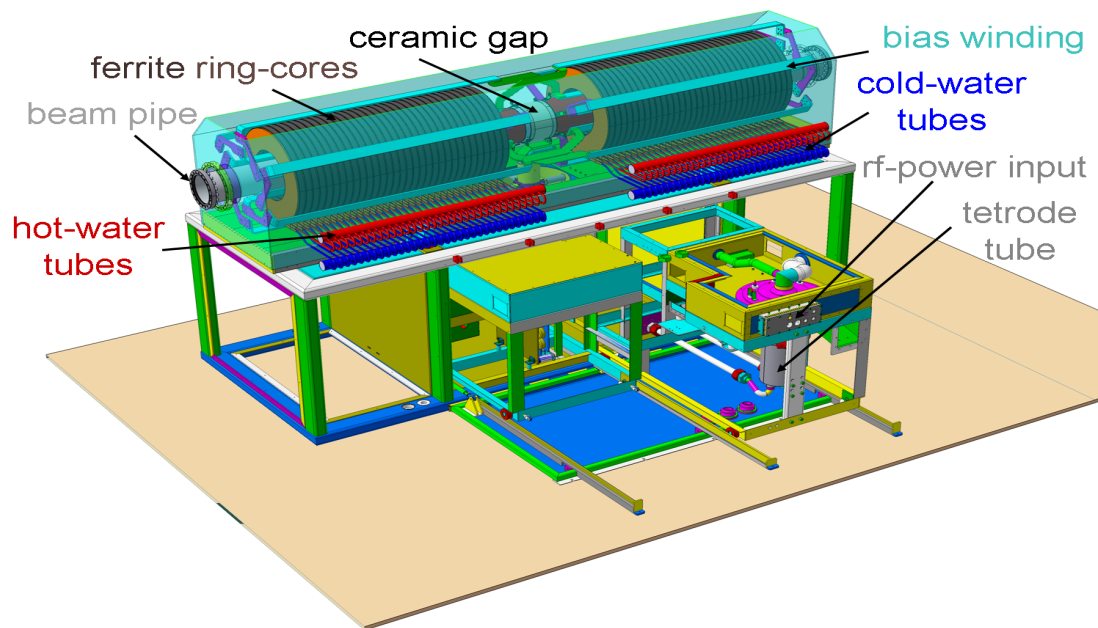


Figure 2.6: A 3D-model and the principle diagram of SIS ferrite cavity, showing rf and bias windings, tetrode tube, copper tubes, cavity gap and the electric field in the gap.

- The bias field is in parallel to rf field but in opposite direction in each half of the cavity. It provides a strong coupling between two halves of the cavity.
- Rf power is supplied by a tetrode tube and is coupled to the core through the rf winding. A magnetic field is induced in the inductor formed by the ferrite core and appears as electric field across the gap capacitor (C_g in Fig. 2.6) .
- The bias winding is arranged as a figure of eight around the ferrite stacks in two halves, producing a balanced rf voltage on each winding and no rf voltage on the ferrite bias source. Additionally a bias capacitor (C_b in Fig. 2.6) is connected to ground the rf signal.
- The dielectric losses result in an increase in temperature and thereby increase in shunt impedance of the ferrite core. To minimize these losses, while being exposed to the magnetic field produced by rf winding, the ferrite core should be shielded from the electric field in the cavity. For this purpose, the ferrite cores are sandwiched by copper tubes. The running water through the tubes acts as a cooling medium for the cavity.
- A capacitor is formed between the ceramic plates connecting the two resonators. A voltage divider is formed with some additional capacitors as shown in Fig. 2.6.
- Electric field in the cavity gap is in the longitudinal direction of motion. Hence imparts energy to the ion beam.
- A virtual ground exists in the middle of the accelerating gap and the voltages on the resonators are in anti-phase [37]. Hence the gap-voltage is measured across the left or right half-gap and the virtual ground. Twice of this voltage (or peak to peak value of the half-gap voltage) is the amplitude of the gap-voltage.

2.3.2 Simplified circuit representation

Electrically, the cavity near a resonance can be modeled as a parallel resonant circuit [23, 17, 18] as shown in Fig. 2.7. By a proper transformation from the rf oscillator to the cavity gap, the power amplifier can be represented by a current source I_g in parallel with the impedance, R_{gen} . This is the impedance for a fixed working point and considering resonance in the tube assembly with transmission line connecting to cavity [18]. Here the cavity is represented by using the lumped parameters L_c , C and R_{cav} . The inductance of cavity material (ferrite) is represented by L_c , the equivalent capacitance of the cavity along with the capacitance formed by gap electrodes (C_g in Fig. 2.6) is represented by C .

Quality factor Q , also known as the figure of merit for a cavity, accounts for the losses in dielectric and in the conducting walls. It relates the stored energy and energy loss in a cavity per cycle and is defined as the ratio of stored energy to energy consumed per period i.e.

$$Q_0 = \frac{U\omega_r}{W}. \quad (2.1)$$

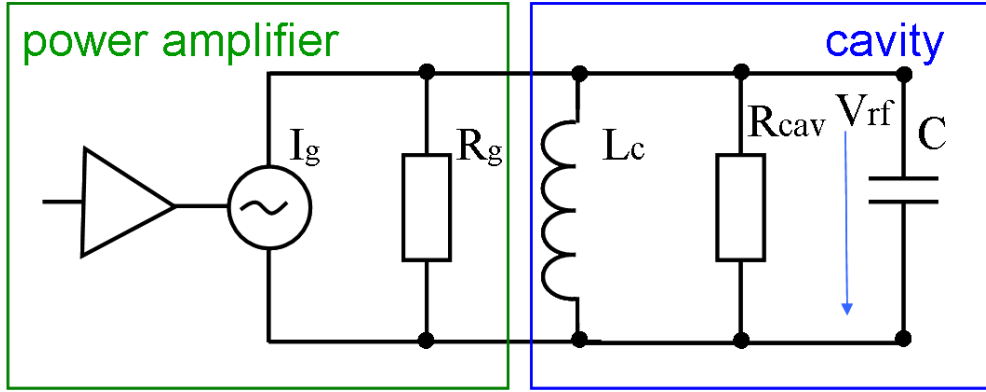


Figure 2.7: A parallel equivalent circuit for cavity, near its resonance frequency. Its all components are presented in terms of lumped parameters.

Here U is the stored energy, W is the power lost in the cavity (is average rate of energy lost for loaded cavity) and ω_r is the natural resonant frequency of the cavity. It is defined as

$$\omega_r = \frac{1}{\sqrt{L_c C}}.$$

The shunt impedance (R_{cav}) is one of the important parameters of rf cavity in accelerators [31, 32, 34]. It represents the power (P) absorbed by the cavity at resonance to maintain a peak voltage V_0 across its gap. It is defined as

$$R_{cav} = \frac{V_0^2}{2P}. \quad (2.2)$$

In case of ferrite cavity, its magnetic permeability varies with the rf voltage and hence its shunt impedance. Further, an effective cooling provision in the cavity (Fig. 2.6) prevents a rise in its shunt impedance due to increase in temperature.

The shunt impedance for the cavity (Fig. 2.8) together with the generator (observed by beam, shown in Fig. 2.5) is

$$R_s = R_{cav} || R_{gen}. \quad (2.3)$$

For maximum power transfer from rf generator (power amplifier assembly) to cavity, the impedances of both the circuits should be matched [35, 68, 69]. Therefore, the working point of the tube (Fig. 2.6) can be chosen so that, in relation,

$$R_{gen} = \frac{R_{cav}}{\beta_c} \quad (2.4)$$

the coupling coefficient, β_c , between cavity and rf generator adjusted to unity for the practical operating range of cavity (and for the given beam intensity).

The behavior of the SIS cavity with the resonance frequency corresponding to injection energy in SIS is shown in Fig. 2.8.

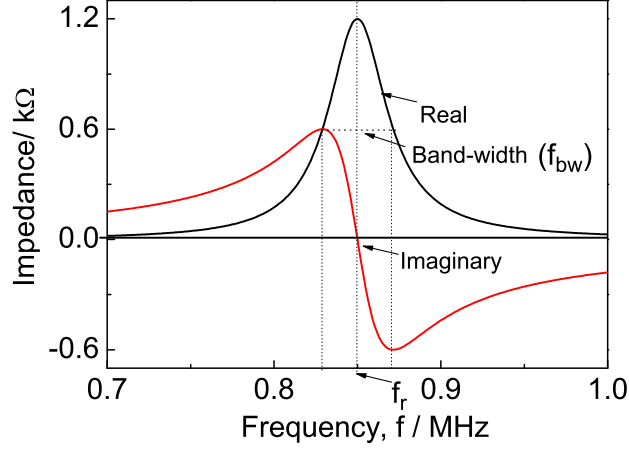


Figure 2.8: Cavity resonance curve showing the variations in real and imaginary impedances at and around resonance. The parameters for the cavity are $Q=20$, $R_s=1.2\text{ k}\Omega$ and resonance frequency $f_r = \frac{\omega_r}{2\pi} = 0.85\text{ MHz}$ and $f_{bw} = 21.25\text{ kHz}$

The amplitude of the cavity impedance at a frequency ω can be expressed as,

$$Z = \frac{R_s}{(1 + iQ\frac{\omega^2 - \omega_r^2}{\omega\omega_r})}. \quad (2.5)$$

And in Eq. 2.5 (also elsewhere unless mentioned specifically) loaded quality factor,

$$Q = Q_0/(1 + \beta_c), \quad (2.6)$$

with Q_0 as the quality factor of the cavity alone (without power amplifier). Another readily

Type of cavity	Q_0	frequency range/ MHz	$R_s/ \text{k}\Omega$
Ferrite	10 to 40	0.8 to 5.6	2
Bunch Compressor	5	0.8 to 5.6	1.7

Table 2.3: Some technical parameters of SIS ferrite and compressor cavities .

measurable parameters for a cavity is, rise or fall time T_r as

$$T_r = \frac{2Q}{\omega_r} \quad (2.7)$$

and it helps to represent the cavity behavior. Furthermore, by using the obtained resonance behavior of cavity, at certain resonance frequency and Q value, its bandwidth can be calculated. It is defined as

$$f_{bw} = (f_h - f_l) = \frac{f_r}{Q}. \quad (2.8)$$

These frequencies (f_l and f_h) correspond to the half-power points. The amplitude of the impedance and hence the power absorbed at these frequencies is half of that corresponds to the resonance frequency.

2.3.3 Control loops

The block diagram in Fig. 2.5 indicates the basic controls scheme to be adopted in an rf system in an accelerator and is applicable for the SIS as well. An Amplitude Control Loop (ACL), in Fig. 2.9, keeps the amplitude of gap-voltage as per the rf cycle and the Resonant Frequency Control Loop (RFCL), in Fig. 2.10, assures an efficient power transfer from the power amplifier to the cavity by keeping them in resonance with each other (i.e. $\omega_r = \omega_{rf}$) [36, 37, 38]. Both of these control loops, collect the gap-voltage through the capacitive gap-voltage divider (Fig. 2.6).

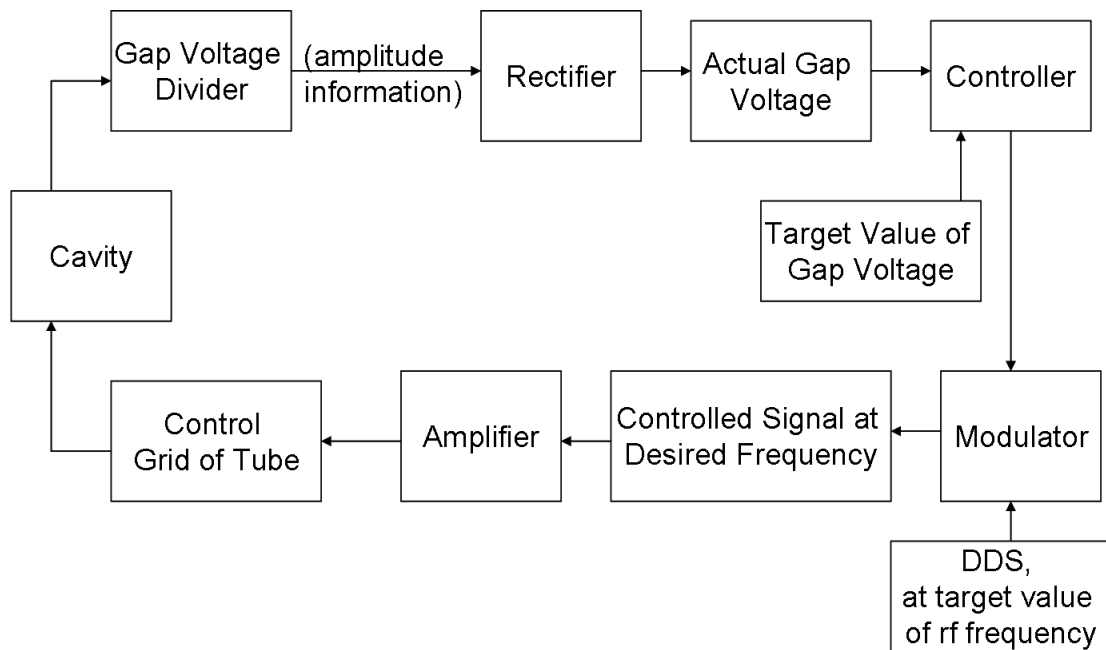


Figure 2.9: Block diagram for the amplitude control loop.

Amplitude Control Loop (ACL)

As shown in Fig. 2.9, the controller compares the rectified or dc amplitude of the actual cavity gap-voltage with its target value. The controller output is then modulated with the target value of rf frequency, which is produced by using digital frequency generator using Direct Digital Synthesis (DDS) technique, explained in detail in Ref. [97, 98]. This rf voltage is amplified and further activates the control grid of the power amplifier (i.e. tetrode in Fig. 2.6). The control grid is an important key in a tetrode tube for controlling the voltage (or anode current) amplification provided by it. Finally the tetrode tube adjusted to new working point now drives the cavity.

Resonance Frequency Control Loop (RFCL)

A fine tuning is achieved for the condition when the anode current from power amplifier is

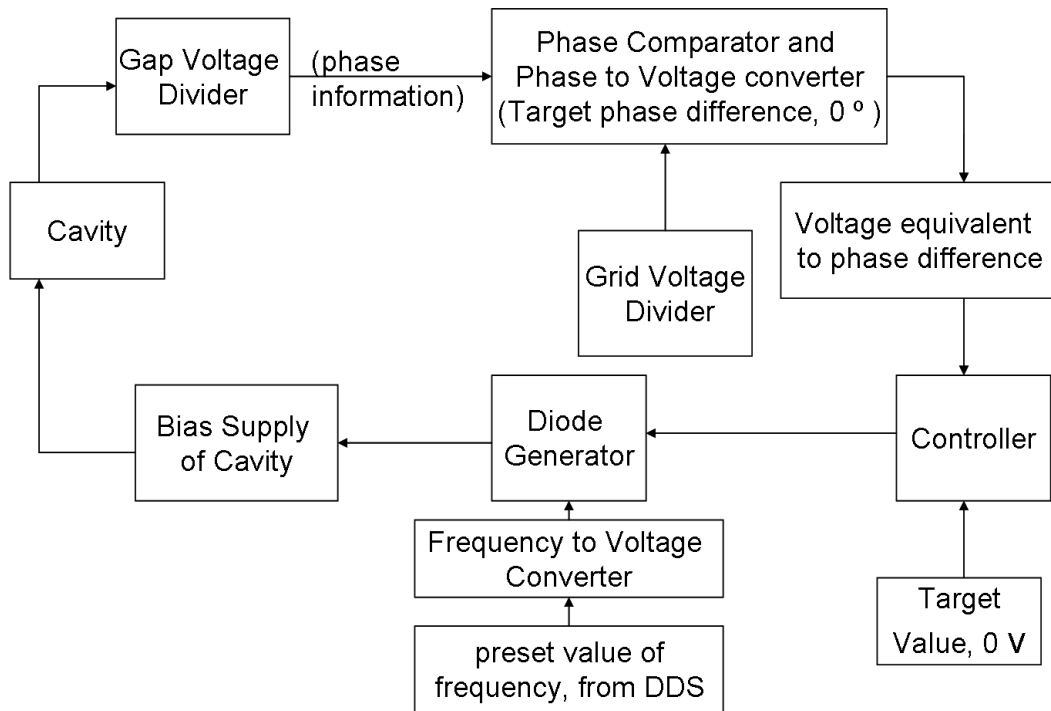


Figure 2.10: Block diagram for the resonance frequency control loop.

in phase with the cavity gap voltage. To achieve this, the phase of the measured gap-voltage is compared with the control grid voltage collected through a voltage divider (1/20). Then the voltage equivalent of this phase difference is compared to its target value, i.e. 0 V. Later a dc signal equivalent to this voltage signal is produced in diode generator. This diode generator works at the voltage equivalent of frequency from the DDS signal. This output controls the bias current which influences the inductance or permeability of ferrite cores and thereby controls the resonance frequency of the cavity.

2.4 FAIR: Motivation behind SIS upgrade program

In order to meet the ever increasing demands of high intensity beams, a new Facility for Antiproton and Ion Research (FAIR), in Fig. 2.11, is proposed besides the existing facility at GSI. It will be a next generation, international accelerator facility built upon the past

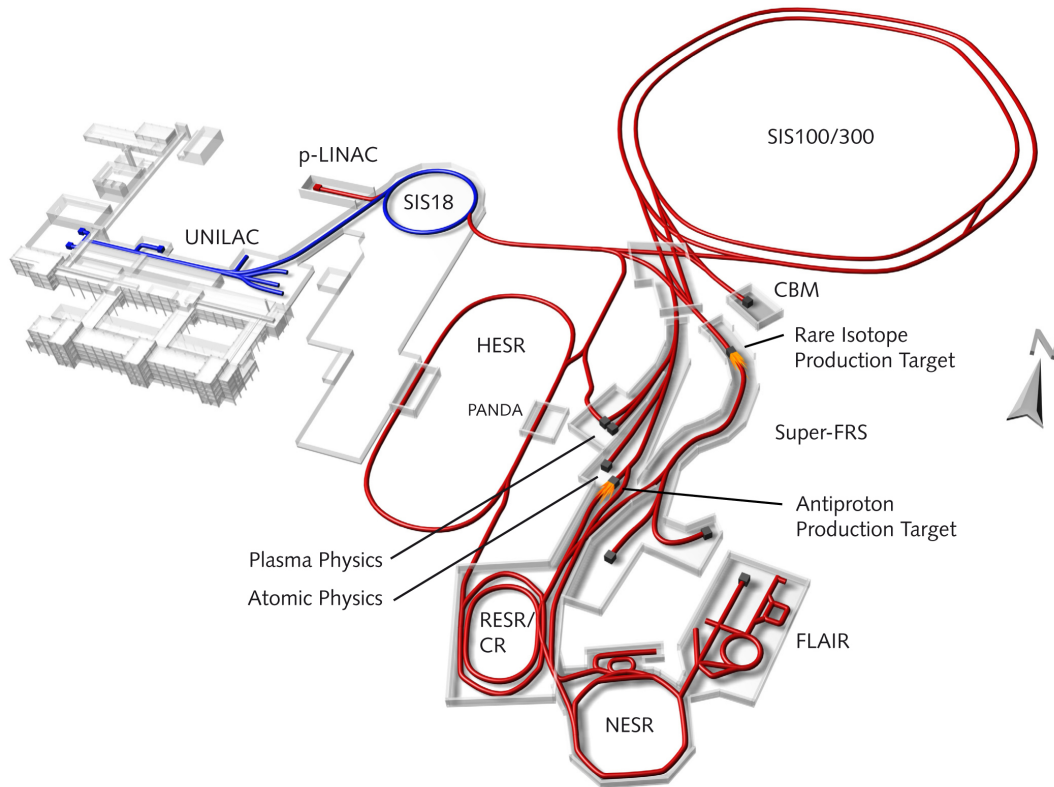


Figure 2.11: Schematic view of present (in blue) and future (in red) facilities with experimental areas (in grey) at GSI, consisting of: superconducting double ring synchrotron SIS100/300; the antiproton production and the rare isotope production targets; the superconducting fragment separator (Super-FRS); the collector and cooler double ring (CR and RESR); two storage rings (HESR and NESR) and the proton linac (p-linac) for the antiproton physics program.

experiences and technological developments already made at GSI. As the name suggests, FAIR will supply heavy ion and antiproton beams. Apart from the several cooler and storage rings at its heart will be a superconducting double ring facility (SIS-100/300) with a circumference of 1083 m. The suffix numbers are indicating their maximum magnetic rigidity [12]. The double-ring synchrotron will provide ion beams of unprecedented intensities as well as of considerably increased energy.

GSI accelerators will serve as booster to SIS-100, which demands, as shown in Table 2.4, the targeted beam intensities for FAIR to go well beyond the capacity of SIS. Hence, SIS

Reference ion	Existing SIS		Upgraded SIS	
	U^{28+}	Ar^{18+}	U^{28+}	Ar^{18+}
Maximum beam intensity/ ppc	$2 \cdot 10^{10}$	$2 \cdot 10^{10}$	$2 \cdot 10^{11}$	$5.8 \cdot 10^{11}$
Machine cycle/ s	3.3	3.3	0.37	0.37
Maximum energy/ GeV/ u	0.2	1.7	0.2	1.7
Type of rf operation	Single rf		Double rf	

Table 2.4: Few beam and machine parameters in existing SIS18, which are to be upgraded from FAIR point of view.

upgrade is an integral part of the FAIR project. For high intensity proton beams, which are required for antiproton production, a separate proton linac (p-linac) as an injector to the SIS will be constructed. Along with this, the upgrade activity needs several technical developments. The efforts in this direction have already been initiated. Key highlights are as follows:

- For the improvement of ultra-high vacuum system NEG (Non-Evaporable Getter) coating is applied to the beam pipe. The NEG coating ($\approx 1\mu\text{m}$) reduces the static pressure in the section between the vacuum pumps [70], for example in dipole and quadrupole chambers. The beam pipe has already been partially replaced by the coated one.
- A dynamic vacuum during beam operation of the order of 10^{-11} to 10^{-12} mbar is required. But at injection, the charge exchange of ions like Ur^{28+} occurs to achieve higher ionic states [70]. These ions after leaving their orbit hit the wall. A large number of gas molecules are liberated due to this ion-induced desorption. And increased gas pressure results in the beam loss in walls until the beam intensity dropped significantly. To prevent this process the collimators, thick blocks with suitable material properties and dimensions, are installed in different sections behind the dipole magnets [71].
- The beam quality is defined by the area occupied by the number of particles in the beam. High intensity beam occupies almost whole machine acceptance. And the Non linear fields and lattice errors produced by a high intensity beam results in deformed closed orbit [72]. Therefore, the closed orbit is to be corrected not only to maintain the beam quality but also to exploit the machine acceptance by preventing the beam loss [73].

- The collective effects in the bunched beams, at various beam intensities, are studied as they play an important role in the damping of longitudinal oscillations [74].
- The stability study of an intense coasting beam is an important aspect. The coherent transverse instabilities of such a beam under the influence of space charge have been inspected [75].
- With increasing beam intensity, collective effects shall play more visible role and must be properly compensated to ensure good quality and high intensity beam [76]. In this context, beam loading study and its compensation are among the main design issues. In this PhD work, the beam loading effect due to the ferrite cavity in the present SIS is studied.

An upgrade of present single rf to the double rf system [44, 45], is one of the important motives under SIS upgrade program. In the new rf system, two cavities, i.e. one of the present ferrite cavities and a new Magnetic Alloy (MA) cavity, will work at different frequencies. Some properties of the new MA cavity are mentioned in Table 2.5. An

Parameter	Q_0	frequency range/ MHz	$R_s/ k\Omega$
Value	0.3	0.8 to 5.6	1.7

Table 2.5: Some technical parameters of planned harmonic 2 cavity for double rf operation in upgraded SIS.

influence of the beam loading and space charge effects, on the beam in a double rf system is studied in the present work.

- To have an adiabatic capture of beam [30, 59] in the upgraded SIS, this study is aimed to assure the conservation of longitudinal emittance and hence the beam quality. Also, the duration of machine cycle (Table 2.4) is to be decreased in order to increase the number of particles extracted per second [77]. A limitation of the time period, available from the fast machine cycle is considered as the most important constraint in the study.

Chapter 3

Longitudinal Beam Dynamics

In synchrotron a charged particle beam is steered by the bending magnetic field which is perpendicular to the particle trajectory, i.e. transverse direction. And an electric field, in the direction of particle motion i.e. the longitudinal direction, imparts energy to the beam for acceleration and also for compensating the energy lost in the ring [16]. The longitudinal particle motion under the influence of electric field generated by the rf cavity can be explained by the longitudinal beam dynamics.

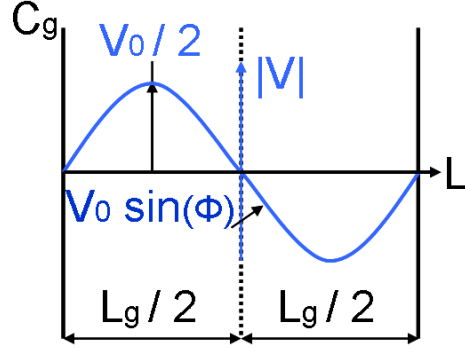
In this report, the whole study about beam capturing and beam loading in SIS is carried out at injection energy. Therefore, the longitudinal beam dynamics is described here for the stationary bucket formed at injection energy. In general, the frequency of longitudinal oscillations is much less than the frequency of transverse oscillations and hence, to a reasonable approximation, they are considered as decoupled.

This chapter provides the information in following sequence. Beginning with the principle and requirement of particle acceleration, the principle of phase stability for single particle motion under the influence of general rf force is explained by formalizing the Hamiltonian function. It is followed by an explanation about the behavior of an ensemble of particles as a distribution function. Thereafter, some important features of rf bucket as well as of bunch are discussed.

3.1 Particle acceleration in SIS cavity

In order to impart electrical energy to the charged particles, a special physical environment is created to produce a field in longitudinal direction of motion and it is called the accelerating cavity (Sec. 2.3). The degree of particle acceleration depends on the instantaneous phase of the rf wave seen by the particle while travelling through it. The rf system (Fig. 2.5) in a synchrotron should fulfil the conditions of synchronicity and longitudinal phase stability [11, 30]. By synchronicity, it is meant that the frequency of rf system f_{rf} should be locked to the frequency of particle revolution f_0 in the ring (otherwise the accelerating voltage will be averaged to zero). It is expressed as $f_{rf} = hf_0$, where integer h is known as harmonic number [11, 20, 30].

Figure 3.1: A schematic diagram showing the SIS cavity gap, where L_g is 0.1 m and C_g is 250 pF.



For a systematic acceleration, the phase of the rf field must reach a specific value at the arrival of the reference particle in the beam. This phase is called synchronous phase (ϕ_s). The Longitudinal phase focusing is achieved by adjusting the synchronous phase [35]. The time-dependent electric field in the rf cavity gap, as shown in Fig. 2.6, is given by

$$E_z(t) = E_{z0} \sin(2\pi f_{rf} t + \phi_s),$$

and electrical energy imparted to the particle at each traversal through the cavity ΔU is written as [9]

$$\Delta U = q \int_{-L_g/2}^{L_g/2} E_z(t) dt, \quad (3.1)$$

where q is charge of the particle and suffix z indicates the longitudinal component of the field, as shown in Fig. 2.6. It can be shown that

$$\Delta U = qE_{z0}L_g T_{tr} \sin(\phi_s).$$

Depending upon the gap-length, L_g (Fig. 3.1) and the revolution frequency of particles, the longitudinal field may vary inside the gap as well. If a particle takes finite time to cross the cavity, the energy gained due to the presence of electric field in the cavity gap is averaged over the transit time. The influence of the gap-length on this energy is reflected by the transit time factor,

$$T_{tr} = \sin(hL_g/2R)/(hL_g/2R),$$

explained in [7, 20], with R as mean radius of synchrotron ring. It shows that along with machine and cavity dimensions it depends on the rf frequency or harmonic number as well. In case of SIS ferrite cavities, the gap length L_g , in Fig. 3.1, is 0.1 m and R is 34.49 m. Here, the single rf system with the harmonic number 4 has the transition time, T_{tr} of 0.9999. In this case the rf voltage seen by the particle is defined as

$$V_{rf} = E_{z0}L_g \sin \phi_s = V_0 \sin \phi_s, \quad (3.2)$$

where V_0 is the maximum amplitude of rf voltage.

The synchronous particle adheres to the ideal plan for the accelerator system. It crosses the cavity at the desired point of time to receive the expected quantum of energy (Eq. 3.1).

For a stationary beam, synchronous particle receives no energy from the accelerating system (ϕ_s is zero or π). But all the other particles in the beam, which are displaced in phase or time with synchronous particle (Fig. 3.2), receive different energies. Longitudinal equation of motion explains the motion of other (non-synchronous) particles with respect to the reference (synchronous) particle.

3.2 Longitudinal equation of motion

The parameters for the non-synchronous particles are summarized in Table 3.1. There

Revolution frequency	$\omega = \omega_0 + \Delta\omega$
Particle energy	$E = E_0 + \Delta E$
Particle momentum	$p = p_0 + \Delta p$
Angular position in the ring	$\theta = \theta_0 + \Delta\theta$
Phase position on rf wave	$\phi = \phi_s + \Delta\phi$

Table 3.1: The relation between the parameters for synchronous and non-synchronous particles. All quantities with suffix are referring to synchronous particle.

will be a distribution of energy or momentum produced due to the phase position or displacement of particle with respect to the synchronous particle, as shown in Fig. 3.2. A two dimensional space defined by the phase and energy (or momentum) coordinates is called longitudinal phase space. The motion of non-synchronous particles in longitudinal phase space with respect to synchronous particle is described by forming the equation of motion, explained in several textbooks [7, 11, 12, 13] and other literatures [8, 9, 72].

The energy gained in one turn by a particle entering the accelerating station with phase ϕ is

$$\Delta E = V_0 q \sin \phi. \quad (3.3)$$

If this change in energy is smooth in one turn then $\frac{dE}{dt} = \frac{\Delta E}{T_0}$, where T_0 is the revolution time, i.e. the time taken for one revolution around the synchrotron orbit by synchronous particle. For a relativistic charged particle with velocity v and mass m , the change in momentum (Δp) is related to the change in energy. Its total energy is given by

$$E^2 = E_0^2 + p^2 c^2, \quad (3.4)$$

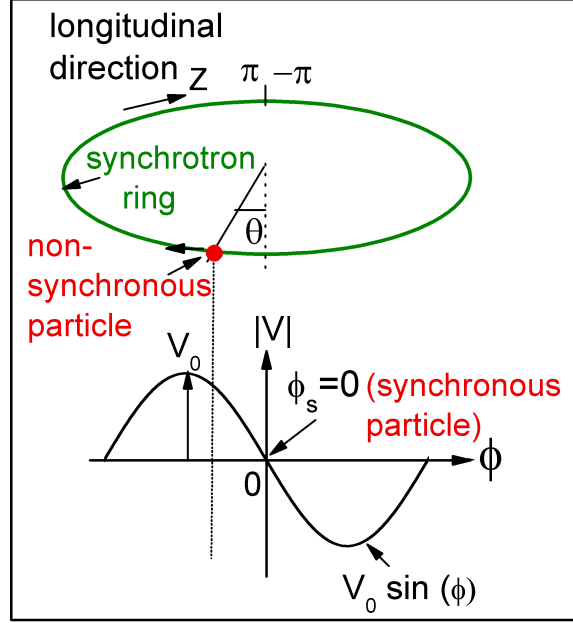


Figure 3.2: A schematic diagram to explain the revolution of particles in the SIS ring and their corresponding position on rf wave. The synchronous particle has phase position (ϕ_s) zero hence receiving no energy from the field which is in the longitudinal direction of motion, Z .

with E_0 as rest mass, momentum $p = \gamma m_0 v$ and $E = \gamma m_0 c^2$, where Lorentz factor or relativity coefficient

$$\gamma = \frac{1}{\sqrt{1 - \beta^2}}. \quad (3.5)$$

The derivative of total energy in Eq. 3.4 with respect to time can be written as

$$2E \frac{dE}{dt} = 2pc^2 \frac{dp}{dt}, \quad (3.6)$$

which for smooth and continuous variations with time can be simplified to $\Delta E = v \Delta p$. Hence, the variation in momentum is $\Delta p = (T_0/L)qV \sin \phi$.

As per the definition of non-synchronous particle (Table 3.1) Δp is the deviation in its momentum (p) from that of synchronous particle (p_0). So the momentum spread in phase space is defined as

$$\delta = \frac{\Delta p}{p_0} = \frac{qV_0(\sin \phi - \sin \phi_s)}{\gamma m_0 v}, \quad (3.7)$$

and variation in the momentum spread with respect to time is

$$\dot{\delta} = \frac{qV_0(\sin \phi - \sin \phi_s)}{L\gamma m_0 v}. \quad (3.8)$$

This relation (Eq. 3.8) is the **first longitudinal equation of motion** defining the momentum variations.

The revolution time for non-synchronous particle is $\tau = L/v$, with L as its path length. For smooth variations in these parameters with respect to their corresponding values for synchronous particle we get, $(\Delta\tau/T_0) = (\Delta L/L_0) - (\Delta v/v_0)$. Here, change in path or orbit length is related to the particle momentum through “momentum compaction factor”, α_p [8, 9]. This is the characteristic of a particular accelerator and is defined as $(L - L_0)/L_0 = \alpha_p(p - p_0)/p_0$. It can be seen that, the particle with higher momentum will take longer orbital path and will reach to the cavity later.

Also, by using the definition of γ (Eq. 3.5) and its relation to the total energy (Eq. 3.4) and momentum variations, it can be related to the momentum spread as $\frac{d\beta}{\beta} = \frac{1}{\gamma^2} \frac{dp}{p_0}$. Thus, the time variations can be simplified to,

$$\frac{\Delta\tau}{T_0} = -\frac{\Delta\omega}{\omega_0} = \eta \frac{\Delta p}{p_0}, \quad (3.9)$$

where $\eta = (1/\gamma_t^2) - (1/\gamma^2)$, with $\alpha_p = 1/\gamma_t^2$. Here γ_t is the transition limit of γ above which, change in path length dominates over change in velocity. Below this transition limit, particle with higher momentum has higher velocity than synchronous particle and hence it reaches the gap earlier. As can be seen in Fig. 3.2, it encounters the rf wave at lower phase angle and hence receives less energy (Eq. 3.3) and vice versa. This reduction in phase and energy (or momentum) is the cause of the stable oscillations of non-synchronous particles in longitudinal phase space. This phenomenon is the very basis of operation of synchrotron and is known as the principle of phase stability [14, 15].

The phase difference (Table 3.1) with respect to the synchronous particle for smooth variations is

$$\Delta\phi = \phi - \phi_s = -h\Delta\theta, \quad (3.10)$$

where change in angular position, θ , is related to the revolution frequency ($\theta = \int \omega dt$) and the negative sign indicates that particle with higher revolution frequency will reach the gap early and phase difference will be reduced and vice versa. This way the phase change in one turn is,

$$\frac{\Delta\phi}{T_0} = -h\Delta\omega,$$

and for smooth variations, by using Eq. 3.9, we get this phase change per turn as,

$$\frac{d\phi}{dt} = h\eta\delta\omega_0. \quad (3.11)$$

The equation 3.11, relating the phase change per turn to the momentum spread and other beam and machine parameters, is the **second equation of motion**. It can be combined with first equation of motion (Eq. 3.8) to form a single second-order differential equation,

$$\frac{d^2\Delta\phi}{dt^2} + \omega_s^2(\sin\phi - \sin\phi_s) = 0. \quad (3.12)$$

Here, for small oscillation amplitude,

$$\omega_s = \sqrt{\frac{qVh \cos \phi_s}{RLm^*}}, \quad (3.13)$$

with effective mass $m^* = -\gamma m/\eta$, is known as synchrotron frequency. It is the frequency of oscillations of non-synchronous particle around the synchronous particle with synchrotron period $T_s = 2\pi/\omega_s$, as the time for one synchrotron oscillation. For stable oscillations ω_s must be a real quantity. For which below transition ($\gamma < \gamma_t$) with $\phi_s = 0$, η should be negative.

The two equations of motion can be rewritten, with the use of Eqs. 3.8, 3.11 and 3.13, in terms of canonically conjugate coordinates [9] ϕ (phase displacement) and $\dot{\phi}$ (phase velocity) of particle.

$$\left\{ \begin{array}{l} \frac{d\phi}{dt} = \dot{\phi}; \\ \frac{d\dot{\phi}}{dt} = -\omega_s^2 \sin \phi \end{array} \right.$$

With the help of following Hamiltonian equations [9, 78]

$$\left\{ \begin{array}{l} \frac{d\phi}{dt} = \frac{\partial H}{\partial \dot{\phi}}; \\ \frac{d\dot{\phi}}{dt} = -\frac{\partial H}{\partial \phi} \end{array} \right.$$

the total energy of the system can be formulated.

3.2.1 The Hamiltonian

A Hamiltonian, signifying the total energy of the system,

$$H = \frac{\dot{\phi}^2}{2} + \omega_s^2(1 - \cos \phi), \quad (3.10)$$

and in general case,

$$H = \frac{\dot{\phi}^2}{2} + \omega_s^2 Y_{rf}(\phi). \quad (3.11)$$

Here the first term corresponds to kinetic energy and second term to potential energy [78] with rf potential

$$Y_{rf} = \frac{1}{V_0} \int_0^\phi V_{rf}(\phi_1) d\phi_1, \quad (3.12)$$

for a particle with phase displacement of ϕ . The particle trajectories in the longitudinal phase space can be calculated by using the Hamiltonian and can be represented as

$$\dot{\phi}(\phi) = \pm \sqrt{2[H_0 - \omega_s^2 Y_{rf}(\phi)]}, \quad (3.13)$$

where H_0 is the value of Hamiltonian, calculated for the initial value of coordinates ϕ and $\dot{\phi}$. For different energies, closed and open particle trajectories in phase space can be derived

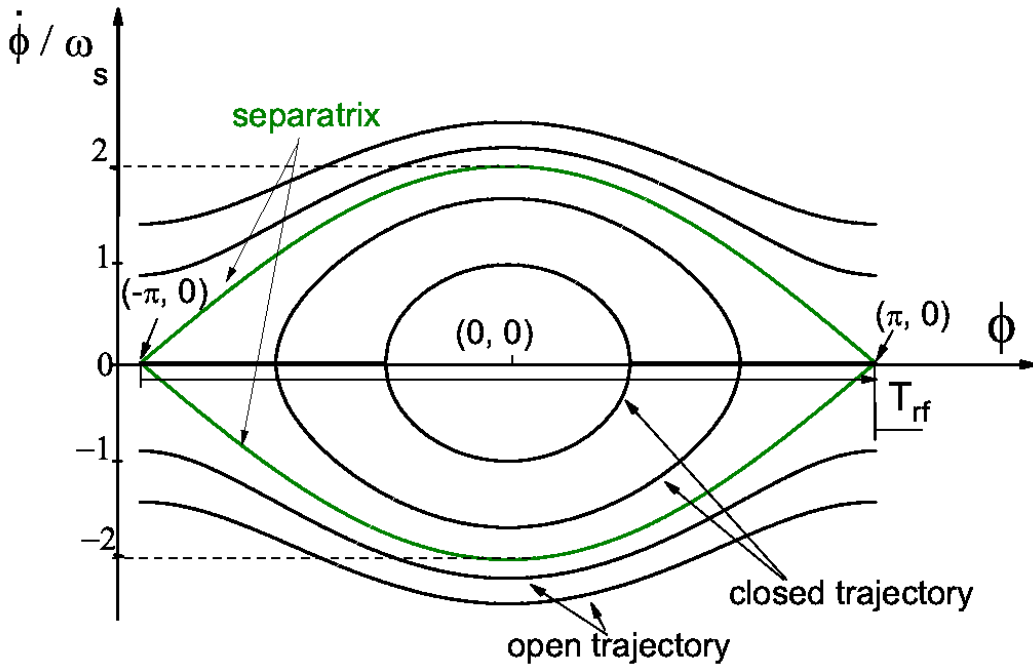


Figure 3.3: The stationary bucket, the stable and unstable trajectories formed by non-synchronous particles around the synchronous particle. The synchronous particle is with coordinate $(0,0)$. For SIS, the length of this stationary bucket at injection energy is $1.18 \mu s$ (against revolution period of $4.77 \mu s$) and bucket height depends upon the ω_s (Eq. 3.13) i.e. upon the amplitude of rf voltage along with other machine and beam parameters. A typical value of $f_s (= \omega_s / 2\pi)$ for SIS is 1 kHz.

from the Hamiltonian. These two types of trajectories are illustrated in Fig. 3.3. One type describes the oscillations about equilibrium points separated by 2π along abscissa and are elliptical for small amplitude oscillations. The other one possess no phase boundaries and is distorted for large amplitude oscillations. The boundary line between the two types of particle trajectories are called separatrices and the area within the separatrices is called rf-bucket. In case of $\phi_s = 0$ (or π), the average energy gain due to the phase oscillations vanishes. In this condition no resultant particle acceleration is achieved and hence the rf-bucket is known as stationary bucket.

3.2.2 Stationary bucket

The bucket formed at constant energy is called stationary bucket. For the given machine parameters and rf voltage it has the largest height and the largest area as compared to accelerating bucket (for $\phi_s \neq 0$ or π). Such buckets are symmetric around the rf phase (Fig. 3.3) which is either zero for $\gamma < \gamma_t$ or π for $\gamma > \gamma_t$. The bucket length is 2π with respect to ϕ and $2\pi/h$ with respect to θ . The height of a stationary rf bucket gives the maximum momentum deviation a particle may achieve during synchrotron oscillation. It is known as momentum acceptance of the accelerator and is defined as,

$$\left(\frac{\Delta p}{p_0}\right)_{rf} = \frac{2}{h\eta} \frac{\omega_s}{\omega_0}. \quad (3.14)$$

For a stationary bucket, the bucket width extends over 2π , which permits (theoretically and for ideally adiabatic processes) to capture continuous beam with the higher efficiency as compared to an accelerating bucket. This is the reason, why the beam injection from linear accelerator to synchrotron is normally performed at injection energy (constant rf frequency) and is true for SIS as well. For SIS rf cycle this region of constant energy (Fig. 2.4) at injection is called as injection plateau. In the present work both adiabatic capture and beam loading studies have been carried out in SIS at injection plateau.

At present the single rf system in SIS is used for creating four buckets ($\omega_{rf} = 4\omega_0$) with all of them equally filled. The particles inside the bucket are arranged in different form, depending upon the type of bucket and the other beam and machine parameters, as explained in the following section.

3.3 Particle distribution

Until now only the interaction of single particle with external electromagnetic fields has been discussed. Practically, the interaction of the beam, as a whole, is required to find its longitudinal beam parameters and its behavior in presence of these fields. In reality the rf bucket is filled by the collection of particles in the form of bunch, arranged in a certain distribution. This distribution should be stationary in time (a matched distribution), which implies that it should be invariant under the influence of synchrotron oscillation of individual particle. All distributions in longitudinal phase space which are the functions of Hamiltonian $f_1(H)$ (Eq. 3.11) can be considered as matched distributions.

The phase projection of longitudinal distribution (Fig. 3.4), is defined as line density,

$$\lambda(\phi) = \int_{-\infty}^{\infty} f(\phi, \dot{\phi}) d\dot{\phi}. \quad (3.15)$$

Generally, both longitudinal distribution and line density are normalized to unity i.e.,

$$\int_{-\infty}^{+\infty} \int_{-\infty}^{+\infty} f(\phi, \dot{\phi}) d\phi d\dot{\phi} = 1;$$

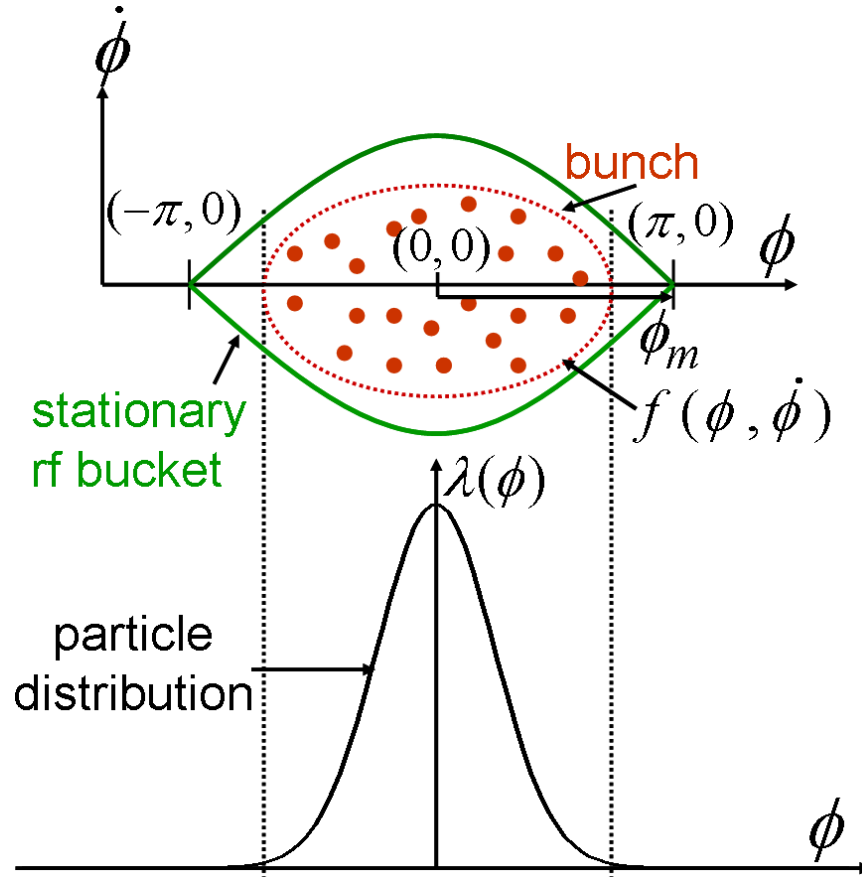


Figure 3.4: The upper part is the stationary bunch with synchronous particle at center with coordinate $(0, 0)$ and the lower part shows the distribution of particles, as per the Eq. 3.15, in this bunch.

$$\int_{-\infty}^{+\infty} \lambda d\phi = 1.$$

Elliptic and Gaussian are among the widely used distributions. Specially, Gaussian is the most frequently observed one in SIS. But, as the particle at the bunch boundaries are too diverged to produce a significant current to be sensed by the pickup probes (Sec. 5.2), virtually the maximum bunch length is limited by the bucket boundaries.

As the particles in the bunch are oscillating in position and velocity, there is a continuous exchange between their potential and kinetic energies. As a result, their energy distribution is also Gaussian. As Hamiltonian represents the total particle energy, so for a Gaussian particle distribution:

$$f(H) = f_0 \exp\left(-\frac{H}{2H_{rms}}\right),$$

where f_0 is a normalizing constant and $H_{rms} = \dot{\phi}_{rms}^2/2$ is the Hamiltonian which is pro-

portional to the rms value of the energies of the particles in a bunch.

Also, from the definition of Hamiltonian (Eq. 3.11) and of line density (Eq. 3.15),

$$\lambda(\phi) = \lambda_0 \exp\left(-\frac{Y(\phi)}{\sigma^2}\right),$$

where $Y(\phi)$ is the total potential. In general, for a double harmonic system it can be expressed as,

$$Y(\phi) = (1 - \cos \phi) - \alpha(1 - \cos n\phi), \quad (3.16)$$

with $\alpha = 0$ for single rf and is nonzero for double harmonic rf system. σ is the rms bunch length proportional to the rms value of the particle phase velocity

$$(\sigma = \dot{\phi}_{rms}/\omega_s) \quad (3.17)$$

and λ_0 is the normalizing coefficient (normalized line density).

For single rf, the line density can be expressed as

$$\lambda(\phi) = \lambda_0 \exp\left(-\frac{1 - \cos \phi}{\sigma^2}\right). \quad (3.18)$$

The expansion of the cosine series can be approximated, by neglecting the higher order coefficients, for small oscillation amplitudes to a Gaussian function as

$$\lambda(\phi) \simeq \frac{1}{\sqrt{2\pi}\sigma_{rms}} \exp\left(-\frac{\phi^2}{2\sigma^2}\right). \quad (3.19)$$

Here, rms bunch length, σ_{rms} is related to the ϕ_m (Fig. 3.4) as $\phi_m = \sqrt{5}\sigma_{rms}$. The relation between Full Width Half Maximum (FWHM) and the corresponding rms value for a Gaussian curve [73] is useful for finding the σ_{rms} for the curve. For example, the rms bunch length, σ_{rms} for a Gaussian bunch is

$$\sigma_{rms} = \frac{FWHM}{2\sqrt{2 \cdot \ln 2}}. \quad (3.20)$$

The bunch length and bunch forms (or potential well distortion) are the properties which are used to study the influence of beam intensity on bunch stability in an accelerator. The study of SIS, under the influence of some specific beam intensity effects, is explained in the following chapter.

An area occupied by the collection of particles, in the longitudinal phase space, depends upon the beam and machine properties and is explained in the following section.

3.3.1 Emittance

During synchrotron oscillations, a particle oscillates between extremes of momentum and phase with respect to the synchronous particle, which results in a steady longitudinal distribution of particles, called particle bunch. The area occupied in longitudinal phase space

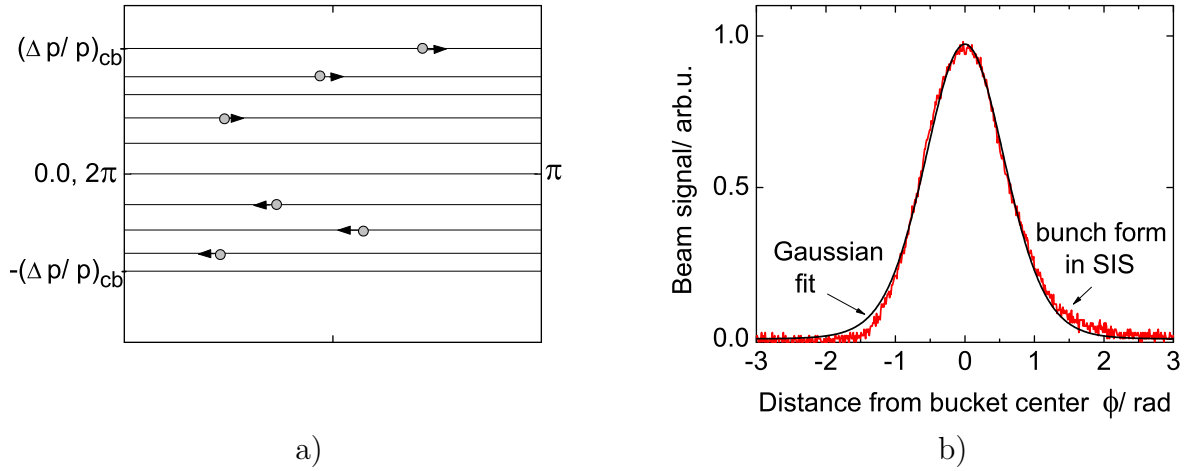


Figure 3.5: a) An illustration of coasting beam in SIS with $(\Delta p/p)_{cb} = 1 \cdot 10^{-3}$ at injection energy of 11.4 MeV/u for Ar^{18+} ions. b) The bunch in the SIS, fitted to Gaussian form.

by this distribution is called emittance. It signifies the bunch temperature, as explained in Ref. [12]. The maximum longitudinal excursion of particles from the bunch center, as shown in Fig. 3.8, defines half-bunch length.

Among many ways of defining the emittance, rms emittance [64, 65] is the most common and accurate one, as it can be calculated for any arbitrary particle distribution. For a continuous distribution of N particles with coordinates $(\Delta\phi_i, \Delta\dot{\phi}_i)$ it can be formulated as

$$\varepsilon_{rms} = \frac{4}{N} \sqrt{\sum_{i=1}^N \Delta\phi_i^2 \sum_{i=1}^N \Delta\dot{\phi}_i^2 - \left(\sum_{i=1}^N \Delta\phi_i \Delta\dot{\phi}_i\right)^2}. \quad (3.21)$$

A direct way of calculating the occupied phase space area is to fit an encircling ellipse around a certain fraction of the assembled particles. It is called elliptic emittance. The limitation with this method is that it may include plenty of empty space when the particle distribution is totally non-elliptic. An un-bunched DC beam is called coasting beam. In principle, the definition of rms emittance (Eq. 3.21) is applicable for coasting beam as well [12]. A uniform particle distribution with a maximum momentum spread of $(\Delta p/p)_{cb}$ in the ring can be represented as shown in Fig. 3.5 a. The rms emittance of this beam can be defined as,

$$S_{coast} = 2\pi 2\sqrt{5}\delta_{cb}. \quad (3.22)$$

Here δ_{cb} , the rms value of momentum spread of coasting beam is taken as $\frac{1}{\sqrt{5}}(\Delta p/p)_{cb}$.

For a Gaussian bunch, observed in SIS in Fig. 3.5 b, the bunched beam area in terms

of its bunch length, ϕ_m and ω_{s0} can be defined as,

$$S_{bunch} = 2\omega_{s0} \int_{-\phi_m}^{\phi_m} \sqrt{\frac{\phi_m^2}{2} - Y_{rf}(\phi)} d\phi. \quad (3.23)$$

Here the maximum bunch length ϕ_m is obtained by fitting the bunch profile and is $\simeq \sqrt{5}\sigma_{rms}$ for single rf. To keep its numerical volume invariant, the emittance is generally defined as a product of energy and time i.e. in the units eVs.

As mentioned in Sec. 2.2, a coasting beam in SIS is captured by ‘switching ON’ the rf system. One of the main constraints here is to preserve the emittance during this process.

3.3.2 Filamentation and Emittance blowup

As per the Liouville’s theorem, the motion of phase space density distribution behaves like an incompressible fluid [79]. In an accelerator with no random dissipation of energy,

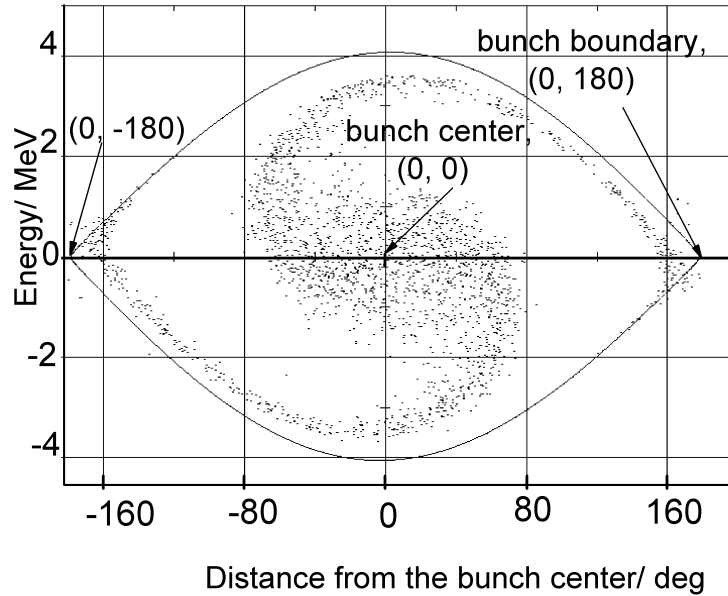


Figure 3.6: The capturing of Ar^{18+} coasting beam in SIS with δ_{cb} as $5 \cdot 10^{-4}$ by using single rf wave with 100 V and 6 kV initial and final amplitude of voltage respectively. The capturing time of 0.5 ms is $2 T_s$ in this case.

and without coupling between longitudinal and transverse planes, emittance is to be preserved throughout the rf cycle. However, during the different rf gymnastics performed in the accelerator, the boundary of occupied phase space area can become arbitrary. This structuring is called the filamentation of particles. This arbitrary complexity adds infinite number of phase space to the actual bunch and appears as an increase in emittance or as

emittance blowup. This phenomena does not violate the Liouville's theorem, as in spite of the filamentation over the whole bucket, the microscopic phase space is still preserved [11].

Generally, the non-adiabatic rf gymnastic or nonlinearities produced by the beam generated fields is the source of filamentation and emittance blowup. An example of it is shown in Fig. 3.6, where a continuous beam is injected in a large rf bucket. The situation can be altered by reducing the rf voltage to the level of energy spread. In this case, the acceptance efficiency is equal to the overlap of bucket and beam in phase space. A sophisticated method of beam capturing, called adiabatic capture, is explained in detail in [30, 59]. The slow and systematic rise of rf amplitude, V_0 , in such a capture process prevents the growth of emittance and allows the capture of almost all particles. For an adiabatic capture the choice of rf ramp parameters, like time for 'switching ON' the full rf and the time to rf amplitude function are important. With the aim of adiabatic capture in SIS, different ramps have been tested and their parameters are optimized. The details are explained in a separate chapter devoted for the adiabatic capture.

3.3.3 Double rf System

The potential well and the type of particle distribution highly depends upon the nature of the rf waveform (Fig. 3.7). When all cavities in an accelerator functions at the same

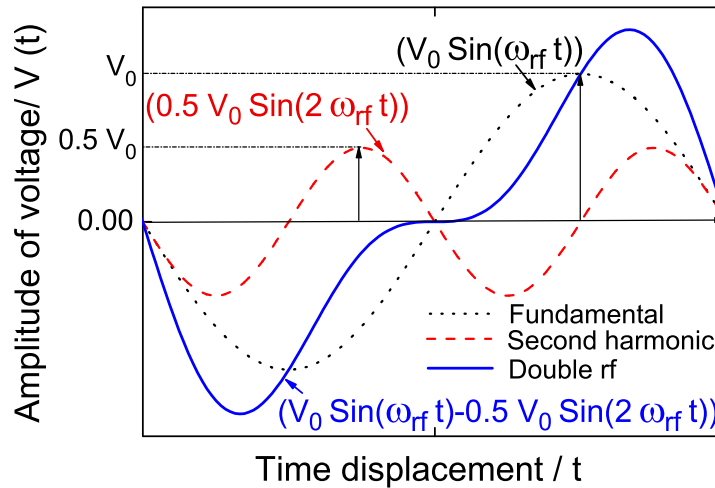


Figure 3.7: The waveforms for fundamental rf wave, its second harmonic and the combination of these two as double rf wave, as planned for SIS.

frequency, it results in a single rf operation. In case of double rf operation [44, 47], the cavities function at two different frequencies. The two ferrite cavities in the present SIS are

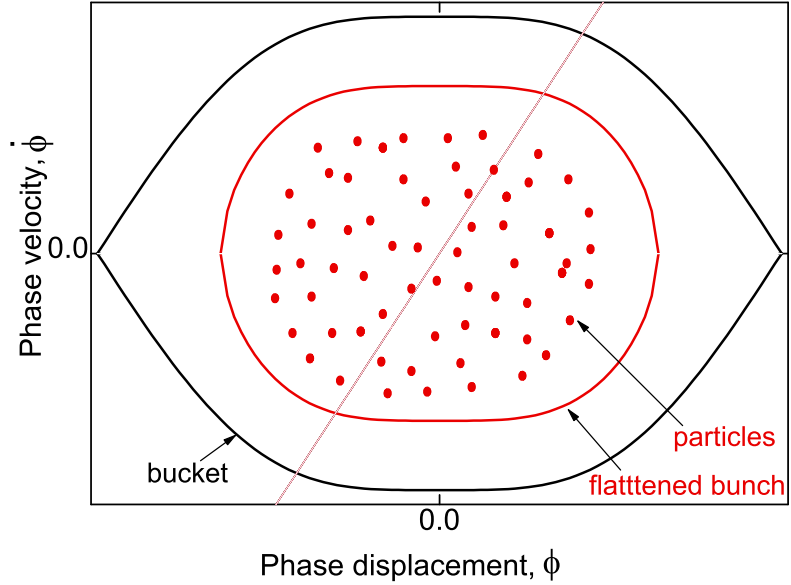


Figure 3.8: An illustration of a flattened bunch under the influence of a stationary double rf bucket formed by the double rf wave shown in Fig. 3.7.

working at the harmonic 4 of the f_0 . In the upgraded SIS (Sec. 2.11), one of these cavities will be replaced by the $h=2$ cavity (Table 2.5) to form the double rf system. This new rf system is aimed to produce flattened longitudinal particle distribution and will provide a sufficient bucket area for faster ramping (Table 2.4).

A double rf system was first installed and tested in the Cambridge Electron Accelerator in 1971 [43]. The frequency and amplitudes of two rf wave (with different frequencies) in double rf system can be adjusted to achieve the flattened potential well. A double rf wave for a stationary bucket can be defined as

$$V_{rf} = V_0 \sin(\omega_{rf}t) - \alpha V_0 \sin(n\omega_{rf}t), \quad (3.24)$$

with α as the fraction of amplitude of the fundamental wave. For SIS, this wave with $\alpha = 0.5$ and with second harmonic i.e. $n=2$ is illustrated in Fig. 3.7. The bucket formed by and the bunch under the influence of such an rf system is demonstrated in Fig. 3.8. The flattened potential well leads to a flat bunch in the center and the maximum density in the bunch center gets reduced. In other words, a higher bunching factor, i.e. the ratio of average to peak current, is achieved [7, 47, 55]. Nonlinearity created by the flat bunches in a dual rf bucket increases the Landau damping [44, 45, 46, 47]. Hence, the bunch in a dual rf bucket is more stable than in a single rf bucket. In the flat region of bunch, the amplitude of external rf voltage is zero and the beam loading effect may become crucial. This effect and its influence on the particle distribution for different type of rf systems is explained in the following chapter.

Chapter 4

Longitudinal Intensity Effects

An energy loss or gain during the beam interaction with its surroundings can significantly modify the dynamics of particle motion. In case of frequency domain approach, adopted in present work, the beam surrounding is represented by frequency dependent impedances [11, 16]. These impedances are strongly coupled to the beam in case they have common components at the same frequency. The longitudinal components of these impedances are considered here, which can be categorized as narrow-band (with $Q \gg 1$) and broad-band (with $Q \approx 1$) as they have different influences on beam.

The ferrite cavity in SIS (Sec. 2.3) comes under the category of narrow-band impedance. The fields induced by beam in such structures are limited to a small frequency width, much less than the revolution frequency f_0 . They can have components at fundamental as well as higher frequencies. And they persist for a long time depending upon cavity parameters like its Q factor and rise time (Subsec. 2.3.2). The Magnetic Alloy cavity (Table 2.5) planned for the upgraded SIS represents a broad-band impedance. Its bandwidth is much larger than the f_0 and fields induced in it by the beam damp faster [16]. The beam cavity interaction represents one of the specific cases of beam interaction with its surroundings and is called beam loading effect [11, 16, 17, 18, 23].

Along with the excitation of electromagnetic field in external impedance, many particles contained in a high intensity beam represent a sizeable charge and current. It acts as a source of electromagnetic fields called self-fields and this effect is called as space charge effect [11, 53, 54, 55].

With the goal to study the beam loading effect in SIS, theoretical description of beam loading effect is presented in the beginning of this chapter. It is followed by the description of the space charge effect. The shunt impedance of the cavity and impedance equivalent of space charge effect are two components of the longitudinal impedance considered in this study. The voltage induced by a stationary bunch in this impedance is derived in the preceding section. The coasting beam stability in SIS is estimated under the influence of this impedance. Thereafter, the influence of this impedance on the bunch form is described and estimated numerically, with single and double rf buckets, for the upgraded SIS. At the end, the simulation programme used throughout this study will be presented.

4.1 Longitudinal beam loading

In an accelerator the performance of the rf system depends highly on its interaction with particle beam. An intense particle beam can induce a significantly strong electric field in a cavity, which is compatible to the external field from the power amplifier (Sec. 2.3). This induced field can modify the magnitude as well as phase of the cavity voltage, which

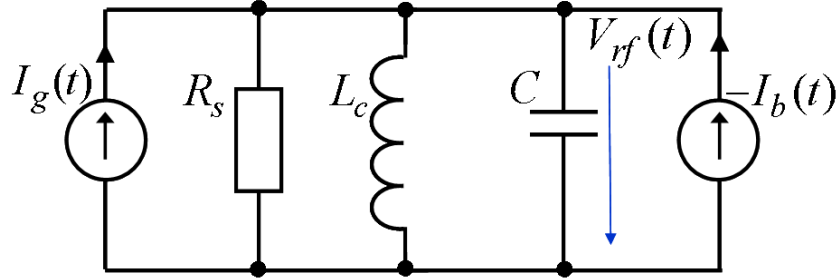


Figure 4.1: A parallel equivalent circuit of rf cavity along with the power amplifier and beam current sources. Here R_s is representing the impedance of rf system observed by beam i.e. the shunt impedance of the cavity along with the power amplifier.

subsequently influences the beam and leads to undesirable beam behavior like the onset of instabilities or particle loss by lack of longitudinal acceptance. Thus the beam loading can restrict the maximum beam current that can be stably accelerated otherwise. In Fig. 4.1, the cavity is modeled similar to the Fig. 2.7 except that, along with the power amplifier, the beam current is also considered. As the velocity of particles (and therefore the beam current) is nearly constant (as $T_{tr} \approx 1$ for SIS) while crossing the cavity, it is realistic here to have the rigid beam consideration [11, 16, 18]. Such a beam is represented as an ideal current source with the consideration that the stored energy of the beam can create enormous instantaneous rf power which is much higher than the capacity of the power amplifier.

An ideal coupling between a tuned cavity and power amplifier is considered i.e. $\beta_c = 1$. Here R_s represents the impedance, which is a combination of shunt impedance of cavity along with the impedance at the final stage of power amplifier of rf system (Eq. 2.3) observed by the beam. The shunt impedance and the lumped parameters of cavity have been defined in Subsec. 2.3.2. The generator and beam currents, I_g and I_b (Fig. 4.1) can be related by using Kirchoff's current law as,

$$I_g + I_b = I_t.$$

These currents contribute to the total gap-voltage.

Fig. 4.2 a, represents the circuit behavior at $f_r = f_{rf}$, where V_{rf} and I_b are in quadrature for a stationary bucket; for acceleration, their phase difference is $\phi_s + \pi/2$. The gap-voltage

V_g is changed under the influence of beam loading voltage V_b to

$$V_{rf} = V_g + V_b = I_t R_s. \quad (4.1)$$

For the cavity tuned to resonance, the amplitude $V_b = I_b R_s$ is maximum, and for off-resonance conditions R_s is replaced by Z in Eq. 4.1

$$V_{rf} = I_t Z = I_t R_s \cos\psi \exp(j\psi),$$

with impedance $Z = R_s + jX$ and reactance $X = \omega L - (1/\omega C)$.

The V_{rf} in phase with the I_g represents the best operating point for the power amplifier, which minimizes the required power transfer to the cavity [16]. Due to the beam loading effect, the angle between these two vectors is changed to ψ (Fig. 4.2 a). The ψ , represents the angle by which the cavity is detuned (to ω), from its resonance frequency, due to the beam loading effect. Also, at beam injection, in adiabatic capture and in fast extraction, where beam current changes abruptly, this effect can influence the beam stability [17, 23]. The cavity detuning and beam stability are discussed in the following section.

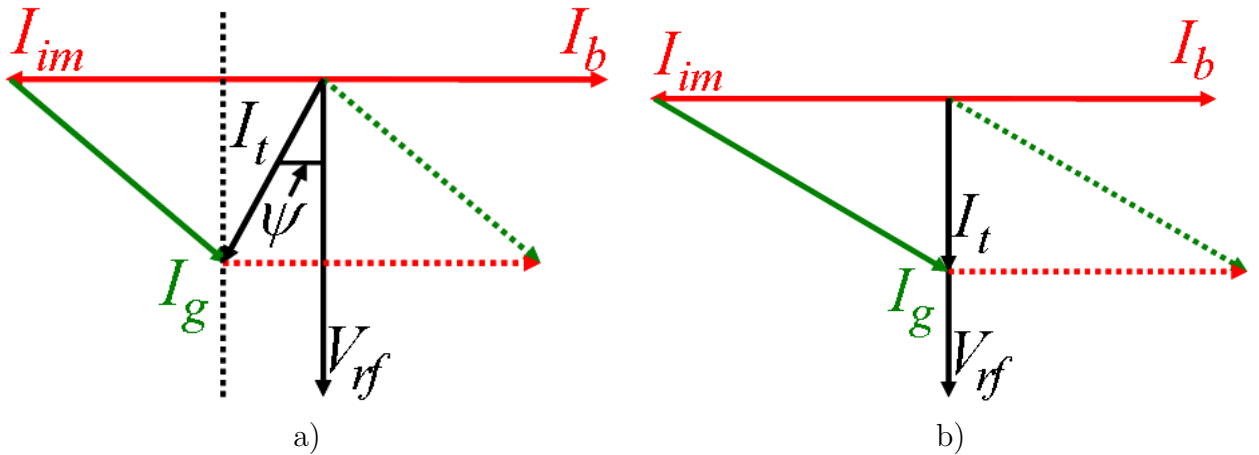


Figure 4.2: a) Phasor diagram showing that the I_b along with I_g is giving the total current I_t . It results in the phase difference ψ between I_t and gap-voltage V_{rf} . b) The phase difference due to beam loading, in phasor a, is compensated by detuning the cavity by angle ψ .

4.1.1 Cavity detuning and beam stability

The beam loading effect in a synchrotron, on the basis of its influence, can be divided in two parts. First is to maintain the efficiency of the power transfer from power amplifier to the cavity. Secondly, to maintain the synchronous phase, which influences the stability of the beam.

For a uniform beam intensity around the SIS ring, with given cavity parameters and for enough time after injection, the stationary situation can be considered. At frequency

$\omega_r = \omega_{rf}$ the voltage and current vectors in Eq. 4.1 can be represented as in Fig. 4.2 a. For a cavity detuned from its resonance condition, the current I_t varies along the dotted line (Fig. 4.2 a) with the tuning to compensate for the reactance, jX of the cavity (with R_s constant). SIS cavity is equipped with a resonance frequency control loop (Subsec. 2.3.3) to maintain the I_g and V_{rf} in phase condition by tuning the cavity back by angle ψ as shown in Fig. 4.2 b. But in some cases the cavity tuning range is not large enough to compensate the steady beam loading and the rf generator must work on the reactive load to deliver the reactive power. Furthermore, the amplitude control loop in SIS rf system (Subsec. 2.3.3) adjusts the amplitude of I_g to compensate for I_b (or any other effect) and this keeps the amplitude of V_{rf} at its desired value.

Above a certain threshold value of the beam current, not only the amplitude but the phase angle between I_b and V_{rf} i.e. ϕ_s also changes. It results in the coupling of the control loops and finally ends with an unstable behavior of the system [23]. Relative beam loading is characterized by the ratio $|I_b|/|I_{g0}|$, with I_{g0} as the generator current required to produce the voltage V_{rf} in a tuned cavity with negligible beam loading. SIS is equipped with a Digital phase control loop (Sec. 5.4) to control the phase of the gap-voltage and hence to maintain the phase stability.

In an accelerator there are situations, like beam capturing or fast extraction, where I_b changes rapidly. In such cases the resulting variations in V_{rf} must be damped fast enough, in time $< T_s$, in order to avoid its influence on the longitudinal phase space, like mismatch, subsequent blow up or even loss of particles. Such situation, due to the beam capturing in SIS, is studied in this work.

Below transition, the beam loading voltage works against the external focusing force of rf system so that a significant beam loading may result in increase in the bunch length and hence subsequent increase in the emittance. Also a trial of tuning the cavity back ($\psi = 0$) may excite phase oscillations which may lead to instability. Robinson's stability criterion [26, 27] is applied to assure the beam stability in this situation. Below the transition this criterion is always fulfilled or, in other words Robinson damping [26] always exists in the system if $\omega_r > \omega_{rf}$ or $\psi > 0$ [7, 11, 16]. The detuning is defined as

$$\tan \psi = 2Q \left(\frac{\omega_r}{\omega_{rf}} - \frac{\omega_{rf}}{\omega_r} \right), \quad (4.2)$$

for $\omega_{rf} \approx \omega_r$ and is simplified to

$$\tan \psi = 2Q \left(\frac{\omega_r - \omega_{rf}}{\omega_r} \right). \quad (4.3)$$

At the same time below transition, increase in frequency corresponds to decrease in momentum gain (Eq. 3.9). Fig. 4.3 is showing the resonance curve of the cavity with $\omega_r = \omega_{rf}$ and the stable region for the tuning. For the stability in longitudinal phase space, cavity should be tuned to $\omega_r > \omega_{rf}$.

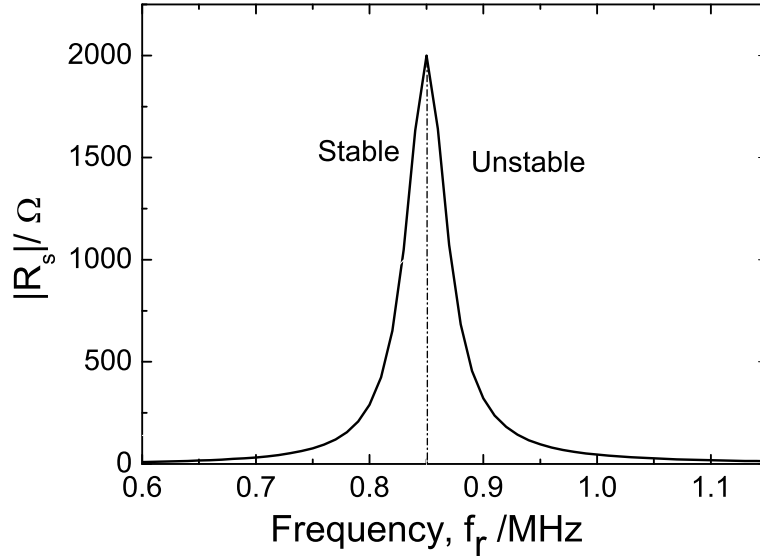


Figure 4.3: A resonance curve showing the region of tuning from beam stability point of view.

4.1.2 Steady-state beam loading

The phasor representation in Fig. 4.2 is valid only when the beam loading voltage is sinusoidal. Due to the finite Q of the cavity, the moment the beam leaves the cavity the beam loading voltage starts decaying exponentially. Then, like a step function, it will charge up again and finally this whole cycle, which is similar to the charging and discharging of capacitor, is a sawtooth wave rather than sinusoidal. This can be described with the help of a Fourier series. Only if the falling time of cavity is large enough so that the decay is negligible to be observed by the following bunch, beam loading voltage is more likely sinusoidal and can be represented by one component at rf (or cavity) frequency. This condition can be expressed as the falling time of cavity T_f is much larger than the distance between two bunches T_{rf} .

$$T_f = \frac{2Q}{\omega_r} \gg T_{rf} = \frac{2\pi h}{N_b \omega_{rf}}, \quad (4.4)$$

where N_b is the number of bunches. In case of SIS, large bunches with $\sigma_{rms} \approx 0.3$ to 0.9 , its ferrite cavity with Q factor of ≈ 30 and rise time of $\approx 11\mu s$ at injection energy. Its T_r is $\approx 10T_{rf}$, rf period. It indicates that, for SIS with 4 long bunches, there will not be a significant fall in sine wave to be recognized by the following bunches while passing through the cavity. Hence only the steady-state beam loading is expected. The $h=2$ cavity (Table 2.5), with Q factor of ≈ 0.3 , $T_r \approx 0.1T_{rf}$ at injection energy, does not fulfil the condition of steady-state beam loading. As its bandwidth (≈ 5 MHz) is much higher than f_0 , several higher harmonics of f_0 can induce a type of collective bunch instability due to

the beam loading [16].

4.1.3 Transient beam loading

A transient beam loading may occur under the following circumstances: for a ring with non-uniform beam intensity, ie. when empty bucket or hole exists for further rf manipulations, at injection when rf voltage is increased slowly for beam capturing or when the condition for steady state mentioned in Eq. 4.4 is not fulfilled. In these situations, rapid changes in I_b are encountered and, at some point, the amplitude of beam loading voltage V_b (or I_b) may become compatible to V_{rf} (or I_g). The resulting variations in amplitude as well as in phase of V_{rf} must be damped not only precisely but also in the time much faster than the synchrotron period to avoid the consequences like mismatch (mentioned earlier), emittance blow up and in worst case the particle loss. Still the vector diagram in Fig. 4.2 is valid but these vectors only at f_{rf} are not enough to describe it. It can be described with the consideration of rf cavity with band limited modulation around f_{rf} . To restore the desired phase and amplitude of vectors, amplitude and tuning loops get active. Simultaneously, a fast beam phase control loop [21] should be active to restore the stable phase angle between I_b and V_{rf} . As mentioned in Subsec. 4.1.1, a digital control system in SIS [98, 99] maintains this phase angle.

4.2 Longitudinal space charge effect

All particles in the beam with same charge, results in a repulsive force between the particles. The influence of this force, which works against the external force, can be manifested as longitudinal impedance, potential well distortion and longitudinal tune shift etc. To quantify this effect, consider a uniformly distributed continuous beam with radius a and with a line charge density $\lambda(z) = h\lambda(\phi)/R$ in a beam pipe with radius b . Its self-field results in a radial electric field

$$E_r(r, z) = \begin{cases} \frac{q\lambda(z)}{2\pi\epsilon_0} \frac{r}{a^2} & r \leq a \\ \frac{q\lambda(z)}{2\pi\epsilon_0} \frac{1}{r} & r > a \end{cases}, \quad (4.5)$$

and an azimuthal magnetic field as

$$B_\varphi(r, z) = \begin{cases} \frac{\mu_0 q \lambda(z) \beta c}{2\pi} \frac{r}{a^2} & r \leq a \\ \frac{\mu_0 q \lambda(z) \beta c}{2\pi} \frac{1}{r} & r > a \end{cases} \quad (4.6)$$

Other field components can be neglected for the case where bunch length (ϕ_m , in meters)

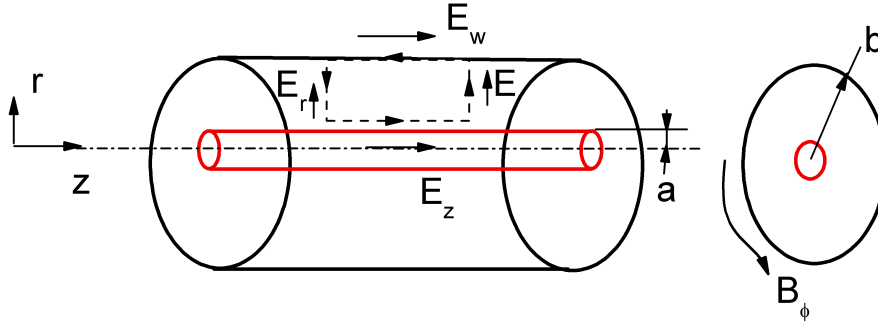


Figure 4.4: The schematic diagram showing the radial and longitudinal fields produced by the beam particles. The closed path for the integration is also shown.

is much higher than the beam pipe radius (b , in centimeters). The electric field produced by the space charge can be calculated by applying the Faraday's law of electromagnetic induction (Stoke's theorem) i.e.

$$\oint \vec{E} \cdot d\vec{l} = -\frac{d}{dt} \oint \vec{B} \cdot d\vec{A}, \quad (4.7)$$

for the fields mentioned in Eqs. 4.5 and 4.6. The integration for the closed path and the fields are as shown in Fig. 4.4 results in

$$(E_z - E_w)dz + \frac{q}{4\pi\epsilon_0}g_0[\lambda(z + dz) - \lambda(z)] = -\frac{\mu_0 q \beta c}{4\pi} \frac{\partial \lambda(z)}{\partial t} dz,$$

with geometry factor $g_0 = 1 + 2 \ln(b/a)$ [53] for a circular beam pipe. It can be modified for different geometries [12, 54]. For a conducting wall ($E_w = 0$) the electric field can be expressed as,

$$E_z = -\frac{qg_0}{4\pi\epsilon_0\gamma^2\beta c} \frac{\partial \lambda(z)}{\partial t}.$$

As the space charge field is to be integrated for the frame which is rotating with the beam, it results in a constant line density λ_z . Hence the space charge voltage per turn V_s can be related to this field as

$$V_s(z) = 2\pi R E_z = -\frac{qg_0\beta c Z_0}{2\beta\gamma^2} \frac{\partial \lambda(z)}{\partial t}, \quad (4.8)$$

with $Z_0 = \sqrt{\mu_0/\epsilon_0} \approx 377\Omega$ is the impedance for free space and μ_0 and ϵ_0 are respectively the permeability and the permittivity for free space. Furthermore, as the Eq. 4.8 shows that this effect scales to $1/\beta\gamma^2$, space charge is an important issue in low and medium energy accelerators.

The force exerted by these self-fields on individual particle of the same beam can be represented in terms of a reactive impedance in the path of the beam, called space charge impedance, X_s . It is defined as

$$X_s = \frac{Z_n^s}{n} = \frac{iZ_0g_0}{2\beta\gamma^2}, \quad (4.9)$$

and the voltage induced due to this impedance at n^{th} harmonic can be calculated by using Eq. 4.14. By following the definition of rf voltage from Eq. 3.12 the space charge potential for a stationary bunch profile can be extracted by intergrading the space charge voltage in Eq. 4.8,

$$Y_s(z) = q\beta_0c \frac{RX_s}{V_0} [\lambda_0 - \lambda(z)], \quad (4.10)$$

and in terms of phase angle ϕ ,

$$Y_s(\phi) = q\beta_0c \frac{RX_s}{V_0} \frac{h^2}{R^2} [\lambda_0 - \lambda(\phi)]. \quad (4.11)$$

This potential can be added to the rf potential to find the bunch distribution with space charge. A typical value of the X_s at injection energy to SIS is $\approx 3.4\text{k}\Omega$, with beam radius is 1/4 of the beam pipe radius.

The shunt impedance of cavity and the longitudinal space charge impedance, are collectively taken here as longitudinal impedance of a ring. The voltage induced in this impedance during the interaction with a stationary bunch depends on their components at common frequency.

4.3 Voltage induced by a stationary bunch

To derive the voltage induced in an impedance by a stationary bunch, the frequency components of beam current are to be known. These frequency components are obtained by the Fourier transformation of the beam current. The line density spectrum has discrete frequency components at $\omega = nh\omega_0$, where n is an integer. The Fourier spectrum for the beam current,

$$I_b(\phi) = qN \frac{\beta ch}{R} \lambda(\phi),$$

of a symmetric bunch with N particles can be expressed as

$$I_b(\phi) = I_{dc} + 2 \sum_{n=1}^{\infty} I_n \cos(n\omega t),$$

where the DC component of beam current is

$$I_{dc} = qN\beta ch/R \quad (4.12)$$

and I_n , the current component at higher frequencies is,

$$I_n = \frac{1}{2\pi} \int_{-\pi}^{\pi} I_b(\phi) \exp(-in\phi) d\phi. \quad (4.13)$$

The voltage induced in the longitudinal impedance $Z_n^{\parallel}(= Z^{\parallel}(n\omega_0))$ interacting with the beam current in Eq. 4.13 is,

$$V_{ind}(\phi) = -2 \sum_{n=1}^{+\infty} I_n Z_n^{\parallel} \exp(in\phi), \quad (4.14)$$

which can be simplified for its component at f_{rf} as

$$V_{ind}(\phi) = -2I_1 Z_1^{\parallel} \exp(i\phi). \quad (4.15)$$

Furthermore, a factor Γ is defined, to compare the DC current to the component at fundamental frequency, as

$$\Gamma = \frac{I_{rf}}{I_{dc}} = 2 \frac{I_1}{I_{dc}}, \quad (4.16)$$

where factor 2 includes the symmetrical current components at f_{rf} and $-f_{rf}$.

The additional voltage $V_{ind}(\phi)$ depends on the type of impedance and on the coordinate ϕ and it does not include the time variable. The time dependence appears if the dipole oscillations are included in the procedure above. Without dipole oscillations, the effective voltage seen by the bunch is time independent and is written as

$$V_{tot} = V_{rf}(\phi) + V_{ind}(\phi). \quad (4.17)$$

In case of cavity V_{ind} is equivalent to V_b and the higher the cavity bandwidth the more current harmonics will contribute to

$$V_b(\phi) = I_{rf}(\phi) R_s. \quad (4.18)$$

Similar to rf potential, in Eq. 3.12, the beam loading potential is defined as,

$$Y_b = q\beta c \frac{hR_s}{RV_0} \int_0^{\phi} \lambda(\phi) d\phi, \quad (4.19)$$

and it depends on the beam intensity and shunt impedance of the cavity. For the bunch in SIS with cavity bandwidth f_b of the order of a few kHz and the revolution frequency f_0 of few hundreds of kHz, the maximum power should go with the fundamental of ω_{rf} .

4.4 Longitudinal impedance and coasting beam

A coasting beam in the synchrotron ring interacts with the longitudinal impedance and its stability remains as an important pre-requisite for the efficient beam capturing in SIS. An

upper limit for the longitudinal impedance is derived by applying the Keil-Schnell criterion [10, 11, 12].

$$\frac{|Z^{\parallel}|}{n} \leq \frac{FE\beta^2|\eta|(\Delta p/p)_{cb}^2}{qI_{dc}}. \quad (4.20)$$

To compare the impedance for different accelerators, the normalized longitudinal impedance, $|Z^{\parallel}|/n$, is used. By respecting the limit, the longitudinal instability in the coasting beam can be prevented. The beams with high intensity and low momentum spread are prone to

Beam and machine parameters	
Ion species	Ar ¹⁸⁺
Total Energy, E/ GeV	37.7
β	0.155
η	0.94
$(\Delta p/p)_{cb}$	$1 \cdot 10^{-3}$
I_{dc} (present/ upgraded SIS)/ mA	12.2/ 35.5
Geometry factor, g	2.83
Cavity and space charge impedances/ k Ω	
X_s	3.36
R_s (ferrite cavity)	5.0
R_s (h=2 cavity)	1.7

Table 4.1: The beam, machine and cavity parameters to find the stability of the coasting beam and corresponding Keil-Schnell limit. The dc beam current I_{dc} is 12.2 mA, which is the maximum stable beam current for the ion Ar¹⁸⁺, in present SIS.

the longitudinal instability because the stability limitation depends inversely on the total beam current, i.e. I_{dc} , and is proportional to the square of the momentum spread of the coasting beam, $(\Delta p/p)_{cb}$.

The stability of the coasting beam before capture, while interacting with the longitudinal impedance, in present and upgraded SIS (Sec. 2.11), is studied. The form factor, F, in Eq. 4.20, is taken as unity, which is true for most of the bell-type momentum distributions [12]. The F, along with the SIS parameters mentioned in Table 4.1, gives the Keil-Schnell limit for the $|Z^{\parallel}|/n$, 3.87 k Ω . The ferrite cavity and the space charge impedances (R_s and X_s respectively) are considered as the main contributors to the $|Z^{\parallel}|$ of the ring. The R_s

is taken from the test cavity measurements (Table B.1) and the X_s (Eq. 4.9) is calculated by using the beam parameters and g factor in Table 4.1. The Fig. 4.5 a, indicates that,

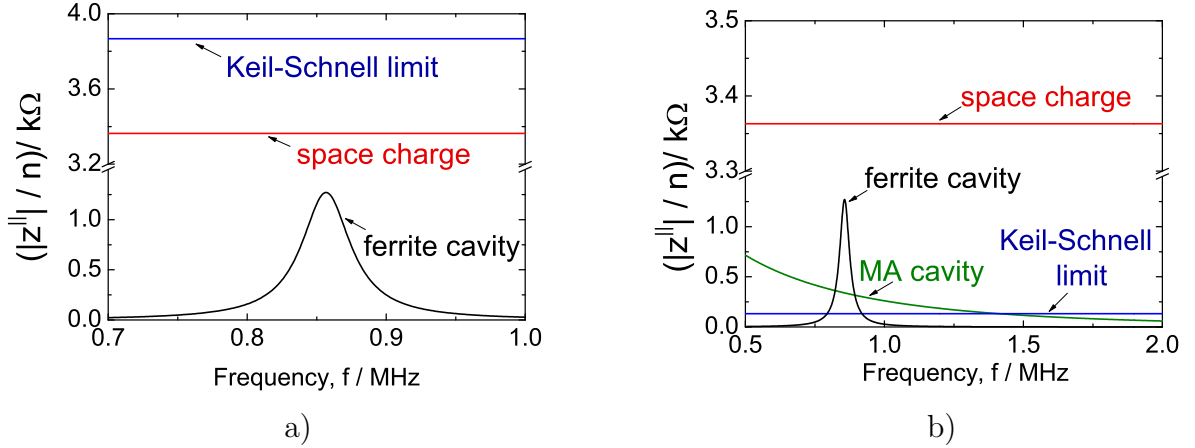


Figure 4.5: a) Keil-Schnell stability limit (Eq. 4.20) for the coasting beam with the space charge reactance, X_s and the shunt impedance, R_s of one of the ferrite cavity in the present SIS. b) The upper limit for the upgraded SIS, with enhanced beam intensity. Here, in addition to the impedances in Fig. a, the R_s for $h=2$ cavity is also considered.

for the given parameters in SIS and summarizing all these impedances, the longitudinal impedance is within the stability limit.

For the upgraded SIS, the R_s for the $h=2$ cavity (Table 2.5) is added in the $|Z^{\parallel}|$ of the ring and the parameters in Table 4.1 are used to calculate the stability limit i.e. 133 Ω for this case. Fig. 4.5 b, shows that for the given parameters and with the enhanced beam intensity in SIS, the cavity impedances are exceeding the limit only in the certain frequency region. *In summary, the longitudinal impedance in upgraded SIS is exceeding the stability limit and needs compensation to avoid the longitudinal instability in coasting beam.*

4.5 Potential well distortion

The equation of the longitudinal phase space motion, Eq. 3.12, indicates the dependence of particle distribution on the time variations of the rf field (Fig. 3.7). This external field, or voltage, is modified by the fields induced due to the intensity effects (Eq. 4.17), which consequently modifies the particle distribution (Sec. 3.3). This effect is called potential well distortion [10, 11, 12, 16]. As the type of rf system has influence on bunch, the effect is described for the single and double rf systems. This effect is introduced in the following section. Estimations for the SIS, with present and upgraded beam intensities, is presented. For both the cases, the cavity impedance is considered as uniformly distributed along the circumference of the ring.

4.5.1 Single rf bucket

The potential $Y(\phi)$ in the Hamiltonian (Eq. 3.11) is modified from Y_{rf} (Eq. 3.12) to $Y_{rf} + Y_b + Y_s$ with the consideration of the beam loading potential Y_b (Eq. 4.19) and space charge potential Y_s (Eq. 4.11). This additional potential modifies the line density, in Eq. 3.18, to

$$\lambda(\phi) = \lambda_0 \cdot \exp[-\alpha_{rf} Y_{rf} + \alpha_{bl} \int_0^\phi \lambda(\phi) d\phi + \alpha_{sc} [\lambda_0 - \lambda(\phi)]], \quad (4.21)$$

with α_{rf} as rf, α_{sc} as the space charge and α_{bl} as beam loading coefficients. The rf coefficient

$$\alpha_{rf} = \frac{1}{\sigma_{rf}^2}, \quad (4.22)$$

depends on the machine and beam parameters through σ_{rf} , where

$$\sigma_{rf} = \frac{h\eta\beta c}{R\omega_s} \left(\frac{\Delta p}{p} \right)_{rms}. \quad (4.23)$$

The space charge coefficient

$$\alpha_{sc} = \frac{qN\beta c X_s}{\sigma_{rf}^2 R V_0} \quad (4.24)$$

and the beam loading coefficient

$$\alpha_{bl} = \frac{qN\beta c R_s}{\sigma_{rf}^2 R V_0}, \quad (4.25)$$

along with the parameters mentioned in Eq. 4.23 depends upon the beam intensity (N) and specifically on the space charge impedance X_s and the shunt impedance of cavity (R_s).

The bunch form in Eq. 4.21 with the consideration of only beam loading effect is reduced to

$$\lambda(\phi) = \lambda_0 \cdot \exp[-\alpha_{rf} Y_{rf} + \alpha_{bl} \int_0^\phi \lambda(\phi) d\phi]. \quad (4.26)$$

As the resistive component extracts energy from the bunch, the whole bunch is shifted to compensate for this loss and, thereby, to maintain the stability in longitudinal phase space [10, 16]. As the new bunch forms modify the beam loading potential (Eq. 4.19), an iterative program is written in Mathematica [94] to find the stable solution of Eq. 4.26 for the final bunch form. The phase shift, ϕ_{bl} , introduced by the beam loading, is derived by applying the condition of constant peak line density λ_0 in Eq. 4.26 under the influence of a constant real impedance. Hence

$$\lambda'(\phi_{bl}) = 0 = \lambda_0 \left[\alpha_{rf} \sin \phi_{bl} - \alpha_{bl} \left(\lambda_0 - \frac{1}{2\pi} \right) \right],$$

where the dc part from the line density is subtracted as it does not contribute to the beam loading effect. Its further solution gives

$$\phi_{bl} \approx \frac{\alpha_{bl}}{\alpha_{rf}} \left(\lambda_0 - \frac{1}{2\pi} \right), \quad (4.27)$$

where the ratio α_{bl}/α_{rf} indicates the amplitude of the beam loading voltage in comparison to that of the external rf voltage.

An example of phase displacement of bunch in single rf bucket in SIS is shown in Fig. 4.6. The machine and beam parameters are mentioned in Table 4.1. Here, instead of

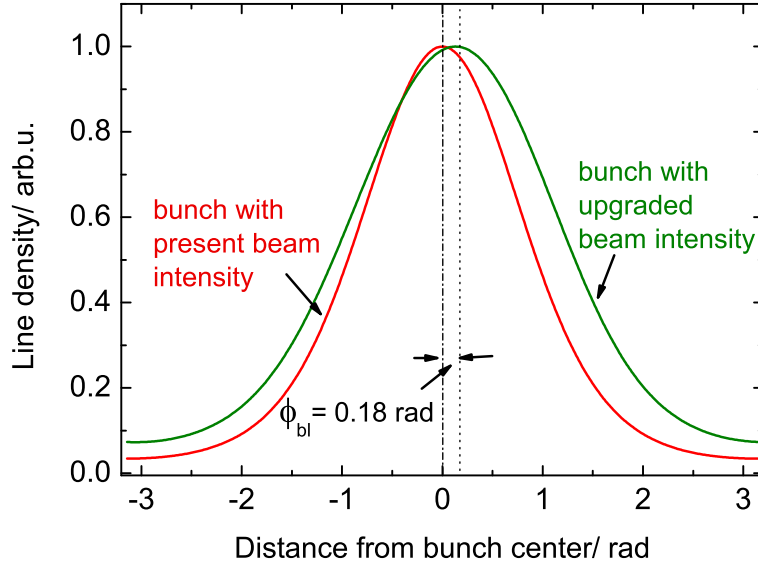


Figure 4.6: The bunch form demonstrates the phase shift under the influence of beam loading effect produced by the MA cavity in upgraded SIS. Bunch form with intensity effects in current SIS is coinciding with the one with no intensity effects.

Intensity in SIS	α_{bl}	ϕ_{bl}/rad
Present	0.05	0.0
Upgraded	1.42	0.18 (or 10^0)

Table 4.2: Beam loading parameter, α_{bl} and phase shift, ϕ_{bl} for present and upgraded SIS for single rf operation with h=2 cavity.

coasting beam, it is the stationary bunch with V_0 as 6 kV for h=2 cavity. The $(\Delta p/p)_{rms}$, in Eq. 4.23, is calculated by considering the matched bunch i.e. the rms emittance of the bunched beam (Eq. 3.21) remains same as the rms emittance of the coasting beam before bunching.

For the single rf operation, with the present and the upgraded beam intensities in SIS, h=2 cavity is considered here. The results are summarized in the Table 4.2. For the upgraded beam intensity, the α_{bl} of 1.42 produces a significant phase shift, ϕ_{bl} (Eq. 4.27), of 10^0 . For the bunch in the present SIS, α_{bl} is too low and its influence on the bunch

is insignificant. In this case the bunch (Fig. 4.6) is coinciding with the one assuming no beam loading effect ($\alpha_{bl} = 0$).

4.5.2 Double rf bucket

The double rf bucket in SIS is aimed to create flat bunches, as explained in Subsec. 3.3.3. The amplitudes of two rf waves (Eq. 3.24) are adjusted so as to have no effective external rf in the middle region of the bunch. As a result, the beam loading voltage is effective in this region. The relation for the bunch form, in Eq. 4.21, for this middle region is reduced to

$$\lambda(\phi) = \lambda_0 \cdot \exp[\alpha_{sc}[\lambda_0 - \lambda(\phi)] + \alpha_{bl} \int_0^\phi \lambda(\phi) d\phi]. \quad (4.28)$$

This relation, with the coefficients α_{bl} (Eq. 4.25) and α_{sc} (Eq. 4.24), shows that the beam loading and space charge effects decide the bunch form in this region. Here again, an iterative program is used to find the final bunch form. It can be expressed as

$$\lambda \approx \lambda_0 + \left(\frac{d\lambda}{d\phi} \right) \Big|_{\lambda=\lambda_0} \phi,$$

by neglecting the higher-order derivatives. The derivative for Eq. 4.28 is

$$\frac{d\lambda}{d\phi} \Big|_{\lambda=\lambda_0} = \frac{\alpha_{bl} \lambda_0^2}{1 + \alpha_{sc} \lambda_0}, \quad (4.29)$$

and it results in the bunch form,

$$\lambda \approx \lambda_0(1 + A\phi). \quad (4.30)$$

An intensity parameter A is introduced here as

$$A = \frac{\alpha_{bl} \lambda_0^2}{1 + \alpha_{sc} \lambda_0}. \quad (4.31)$$

For a given beam intensity, it indicates the slope introduced, in the middle region of bunch, under the influence of the beam loading and space charge effects. The Eq. 4.30, shows that this slope is introduced by the beam loading (α_{bl}) and a compensation to this effect is provided by the space charge (α_{sc}).

Bunch forms for the double rf system with present and upgraded beam intensities are shown in Fig. 4.7. The tilted bunch form, with the slope due to the beam loading effect, represents the case of upgraded SIS. The beam, cavity and space charge parameters are mentioned in table 4.1. The V_0 as 6 kV for the h=2 cavity in the double rf system (Subsec. 3.3.3). The parameters, α_{bl} , α_{sc} and A, for the present and upgraded SIS, are summarized in the Table 4.3. The intensity parameter (Eq. 4.31) A, results in a slope of 16^{-0} in the middle part of bunch. The distorted bunch form is clearly visible in this case,

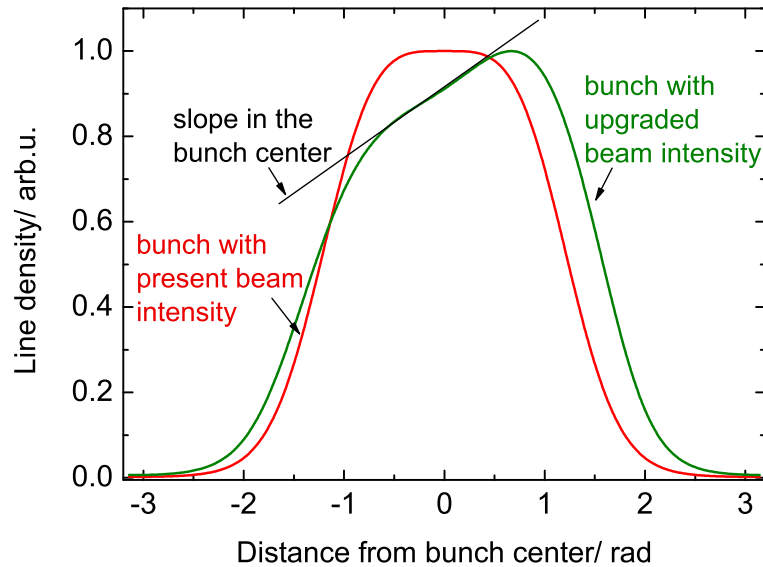


Figure 4.7: The numerical solution of Eq. 4.28 for bunch form under the influence of beam loading and space charge effects, for Ar^{18+} ion, in double rf system in upgraded SIS with MA cavity.

Intensity in SIS	α_{bl}	α_{sc}	A
Present	0.05	0.1	0.02
Upgraded	1.42	2.81	0.13

Table 4.3: Beam loading, space charge and intensity parameters for present and upgraded SIS for the double rf operation with $h=2$ cavity.

in Fig. 4.7. For the present SIS, A is too low (0.02) to produce any visible effect. And, the bunch form is coinciding to the one with no intensity effects.

The model for the potential well distortion, as mentioned above, is applicable for the broad-band cavity due to the consideration of the distributed R_s in the ring.

The iterative programme used for deriving the final stable bunch form assumes the double rf bucket to be produced by the two identical cavities. But, in reality, the planned double rf in upgraded SIS will be produced by the two different type of cavities i.e. a ferrite and a magnetic alloy cavity. With simulation programme it is possible to overcome these limitations.

4.6 Simulation programme

Accelerator in itself is a complex machine for its functioning depends not only on several parameter settings, but also on the electronics around including the beam diagnostics. The simulation makes it possible to create a virtual ideal machine, where the beam with its surroundings can be studied by avoiding any errors introduced by its surroundings (eg. vacuum chamber) and the beam diagnostics. In the present work, a Fortran based simulation code ESME [39] developed by Prof. J.MacLachlan (from Fermi National Laboratory) in 1988 is used.

ESME models the beam behavior in a synchrotron, or in a storage ring, under the influence of rf system [40]. Here, the evolution of the energy-azimuth coordinates is extracted by iterating a map corresponding to single-particle equations of motion [39, 40]. The energy and phase of the i^{th} particle relative to the synchronous particle (the s^{th} particle) are tracked, at regular intervals along the ring, by using two difference equations,

$$\vartheta_{i,n} = \left[\frac{\tau_{s,n-1}}{\tau_{s,n-1}} \vartheta_{i,n} + 2\pi \left(\frac{\tau_{i,n}}{\tau_{s,n}} - 1 \right) \right]_{\text{mod } (\pi)},$$

$$E_{i,n} = E_{i,n-1} + eV(\varphi_{s,n} + h\vartheta_{i,n}) - eV(\varphi_{s,n}),$$

with τ as the revolution period, ϑ as the azimuthal phase position of a particle with energy E and φ as its phase with respect to synchronous particle in rf wave. ESME defines the default values for all the ring and beam parameters.

To simulate a specific beam in SIS ring, the important parameters which have been introduced are γ_t , ring radius, beam energy, rest mass and atomic number of accelerating particle along with the initial momentum spread of coasting beam and the type of particle distribution in bunched beam. The rf cavities are distributed symmetrically around the ring. Both cavities in SIS are placed with a phase difference of 180° . For the rf system, the voltage amplitude ramp is introduced by defining initial, final voltages and ramping time. Different values of these parameters along with the type of amplitude ramp, like iso-adiabatic, parabolic or linear, are chosen for simulating the capturing process [59, 66] in SIS. For the stationary bucket (Sec. 3.2.2), the rf frequency is calculated in ESME by using the injection energy of the beam with the goal to have matched bunch i.e. to match the bunch center with the bucket center. The planned double rf system for SIS (Sec. 3.3.3) is simulated by inserting appropriate harmonic numbers, phase difference and amplitudes of fundamental and second harmonic. The modelling of multiple rf systems, longitudinal beam loading and space charge effects is done here by using the linux version of ESME2000 and ESME2003. ESME adopts macro-particle (maximum 1×10^5) approach for calculating these effects in both, time and frequency, domains. For beam loading calculations, cavity parameters like R_s , Q and f_r (Sec. 2.5) are introduced in a separate data file [42]. The beam and a conducting-wall beam pipe with radius (4 and 10 cm respectively) along with the number of charged particles in the ring are introduced for simulating the space charge effect [41].

In order to quantify the properties of the distribution, several outputs like energy, momentum, rms emittance, rms bunch length, the beam loading and space charge voltages,

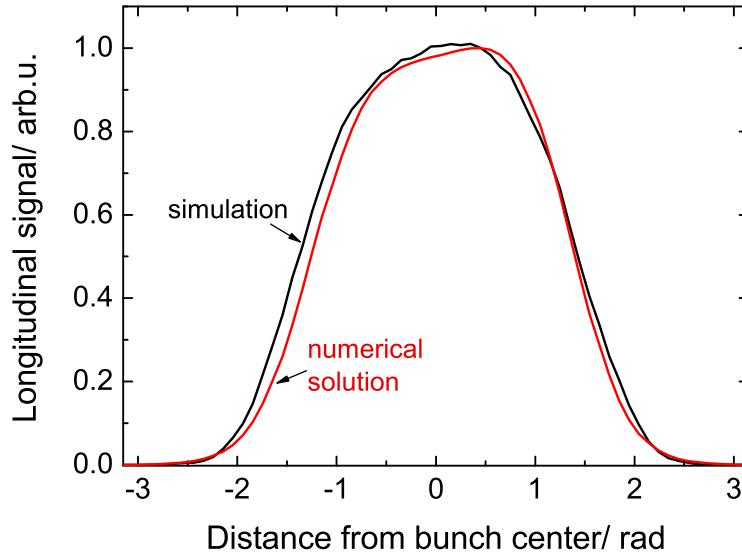


Figure 4.8: The bunch form under the influence of beam loading and space charge effects, for Ta^{61+} ion, in double rf bucket from numerical solution (Eq. 4.28) and ESME simulations.

bunching factor, rf amplitude ramps etc. have been plotted as a function of time. The information about the bunch form is collected as an ASCII file and plotted, as per the requirement, to compare it with the numerical calculations or the measurements.

Fig. 4.8 shows the example of the bunch form, from ESME simulations, along with the bunch form from the numerical solution of Eq. 4.28. The influence of beam loading and space charge effects results in α_{bl} , α_{sc} and A , for Ta^{61+} ion, as 0.34, 0.57 and 0.09 respectively. *The good match of simulated bunch form with the one from numerical calculations (Eq. 4.28) is helpful in planning the measurements on SIS and also for predicting the effects for the upgraded SIS.*

The simulations are benefitted with the flexibility to choose the different type of cavities and their frequencies and it could overcome the limitations of the numerical solutions. But, on the limitation side, it cannot predict the exact beam loading, unless the exact value of the R_s is known. Further, the influence of the beam loading on the control loops and the type of beam loading can be confirmed through the measurements only.

Chapter 5

Longitudinal Beam Diagnostics in SIS

This chapter explains the beam diagnostics [82, 83] adopted for the longitudinal beam loading and adiabatic capturing measurements in SIS. These measurements need a record of beam intensity, bunch form and the momentum spread of coasting and bunched beams.

A precise measurement of beam intensity, along with the accounting for the unwanted fluctuations, is required corresponding to other quantities like gap-voltages and beam signal measured in parallel during the experiments. Therefore the intensity is recorded directly and continuously at the output of a DC transformer, which is designed and manufactured at GSI [84, 85] and explained in Sec. 5.1. Then the description about Beam Position Monitor (BPM) [83, 88], which is used to detect the longitudinal bunch form is presented. This time-domain signal is observed by using an oscilloscope. It is followed by the description about Schottky pick-up, which is used to collect the frequency-domain information from the beam. This information is observed by using a spectrum analyzer and is used to calculate the momentum spread of coasting beam [83, 89]. Further, the Digital Signal Processing (DSP) system, which is used to measure and control the phase difference between beam current and gap-voltage (Fig. 4.2), or between the gap voltages, is explained. This DSP system is programmed and customized at GSI as per the specific requirements [98, 99].

5.1 DC Transformer

Beam current in a particle accelerator is commonly measured by passing the beam through the toroidal core with high magnetic permeability of a Current Transformer (CT) [85]. Here the beam acts as primary winding (Fig. 5.1 a) and the secondary winding on the core is magnetically coupled to it [86, 87]. Due to the high permeability the field lines are guided through the toroidal core such that only the azimuthal component is effective. Hence, it keeps the signal strength nearly independent of the beam position inside the vacuum pipe. The voltage induced in the secondary winding, $V(t)$, is equivalent to the beam current, I_b .

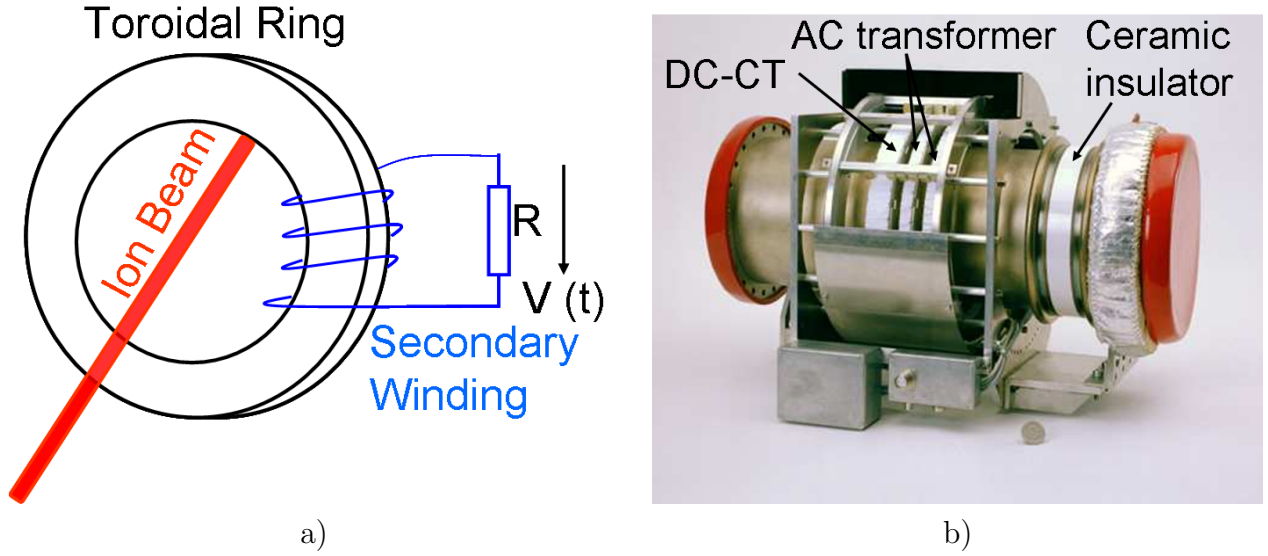


Figure 5.1: a) Principle diagram for Current transformer used for beam current measurement. It is showing the ion beam through the toroidal core. The current induced in the secondary winding is collected as the voltage drop, $V(t)$ across resistor R . b) A photograph of DC-CT in SIS ring. A high permeability, of order 10^5 , VITROVAC toroidal ring with inner diameter of 260 mm and 10 mm^2 is used for all CTs. (Courtesy: Mr.Achim Zschau)

At a certain instant, the induced voltage,

$$V(t) = I_{sec}(t)R_t.$$

From the definition of a transformer,

$$V(t) = I_b \frac{R_t}{N_t} = I_b S, \quad (5.1)$$

with N_t as the number of turns on the secondary winding and S as the sensitivity or calibration factor. Both the R_t and N_t should be considered for calculating the calibration factor.

For beam current measurement in SIS for different parts of rf cycle (Fig. 2.4) two different types of CTs are used. The passive pulse type fast CTs [83, 85], which can measure only pulsed beam currents, are used for multi-turn-injection and fast extraction observations. However, the DC-CTs based on the well-known fluxgate principle, which can account for the DC component [84, 86, 87] as well. They are used for the beam during accelerating ramp, the coasting beam and during the slow extraction. As all measurements in this work are performed at injection plateau, an information about the intensity of the coasting as well as the bunched beam is required. Therefore the DC-transformer shown in Fig. 5.1 b, is used for the measurements.

The beam signal from longitudinal pick-up (Sec. 5.2) is passed through the core of DC-transformer. The beam current I_b from $300 \mu\text{A}$ to 1 A can be measured here [83]. By definition, the response of a CT is limited only for an ac signal. But an adoption of appropriate electronics makes the measurement of dc current possible. DC-transformer in SIS (Fig. 5.1 b) consists of three high-permeability (10^5) VITROVAC toroidal rings. The

DT_ML-TRAFO-PROTOKOLL

HHD — S12 — $^{181}\text{Tl}^{61+}$ — 416.540 MeV/u

23. Apr 09 18:06:22

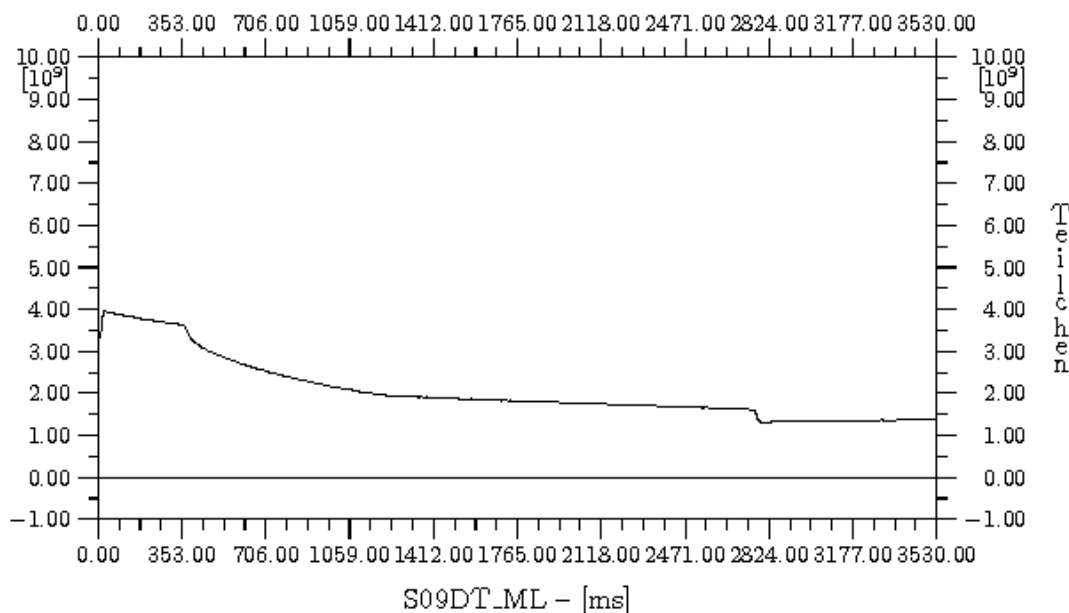


Figure 5.2: An example of the beam intensity, in the units of particles per cycle corresponding to time in ms, recorded in main control room.

first torus from the left, consisting of two coupled toroidal rings, is the DC transformer. The other two rings act as ac transformer for feedback and for controlling injection respectively. The two tori, with similar magnetic characteristics, of DC transformer consist of three types of windings each. These windings are used for the modulation, demodulation and for measurement purposes. Its detailed working principle is explained in these references [83, 85, 86, 87].

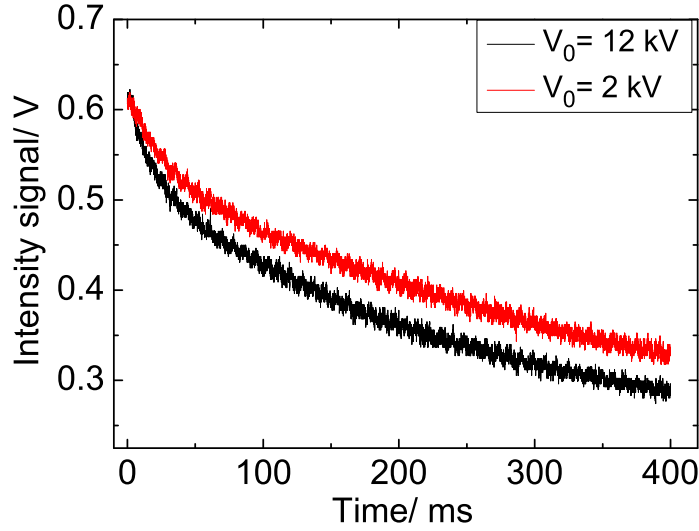


Figure 5.3: An example of the beam intensity, in units of voltage (induced in secondary winding of DC-CT) vs time in ms, recorded in rf experiment hall where the measurements were performed. Two curves for different rf voltages are showing the clear fluctuations in the beam intensity which is expected to be constant.

A time error is introduced due to the physical distance between the measuring instruments and intensity records made in main control room. To overcome this effect a continuous record of the beam intensity, along with the other measured quantities like gap voltages and beam signals, the direct outputs from the DC-CT is tapped during measurements. This simultaneous recording of signals is done by using a Lecroy oscilloscope (explained in Sec. 5.2). The beam current calculation by using the measured voltage (Eq. 5.1) needs the calibration factor, S . It is calculated for each experiment separately to include the effect of daily offset [84]. For this purpose, the intensity record from the main control room (Fig. 5.2) and from the direct measurement (Fig. 5.3), for a particular instant, are compared. In this way, an accurate value of beam intensity has been calculated corresponding to the other settings and measurements with the time resolution of $\approx 0.1\mu\text{s}$. Also, the beam intensity fluctuations can be compared and accounted for different cases shown in Fig. 5.3.

5.2 Beam position monitor

Beam Position Monitor (BPM) is one of the most frequently used non-destructive diagnostic device in nearly all types of accelerators. As the name indicates, it provides the center-of-mass of the beam for both transverse planes. Along with this, it monitors the longitudinal bunch shape as well. And this is the very purpose of using the BPM in this work.

It works on the principle of induction of charge on an insulated metal plate, placed in the electric field of the beam particles [88]. For time-dependent bunched beam, this charge

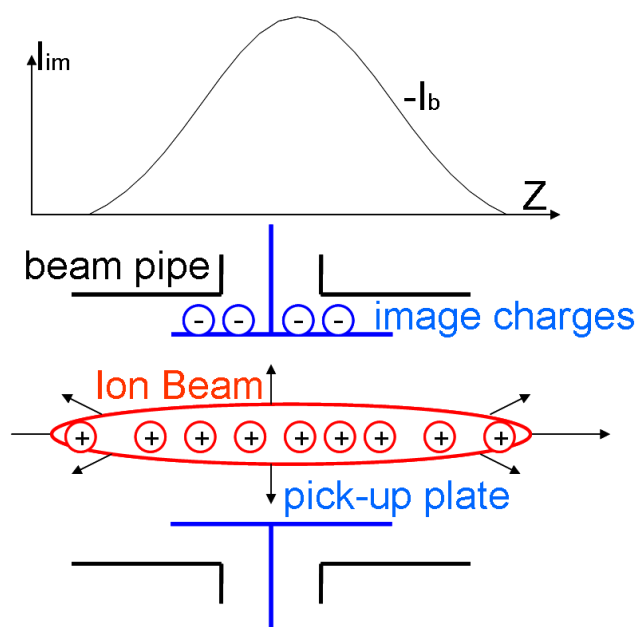


Figure 5.4: Principle diagram of longitudinal beam pick-up, showing the beam pipe with ion beam inducing the opposite ions on metallic pick-up plates. This signal is detected by using electronic circuit shown in Fig. 5.6 and longitudinal beam profile is displayed by using an oscilloscope.

is in the form of an alternating current (ac) signal as can be seen in Fig. 5.4. Considering the frequency range of the beam signal, this signal is coupled using rf technologies for monitoring or measurement purpose. Due to this principle of monitoring longitudinal bunch shape, it is also called electromagnetic pick-up.

BPMs are categorized based upon the method of realization of the working principle. Longitudinal beam pick-ups used in SIS are of ‘Shoe box’ type with linear cut as shown in Fig 5.5 a. The frequency range of it is 0.2 to 100 MHz, which covers the higher harmonics of the bunch frequency. It is a box-like arrangement of four metal plates which in simplest form resembles a diagonally cut shoe-box (Fig 5.5 b). As the beam passes by, it induces different electric charge on the metallic electrodes. The concept is to measure this induced

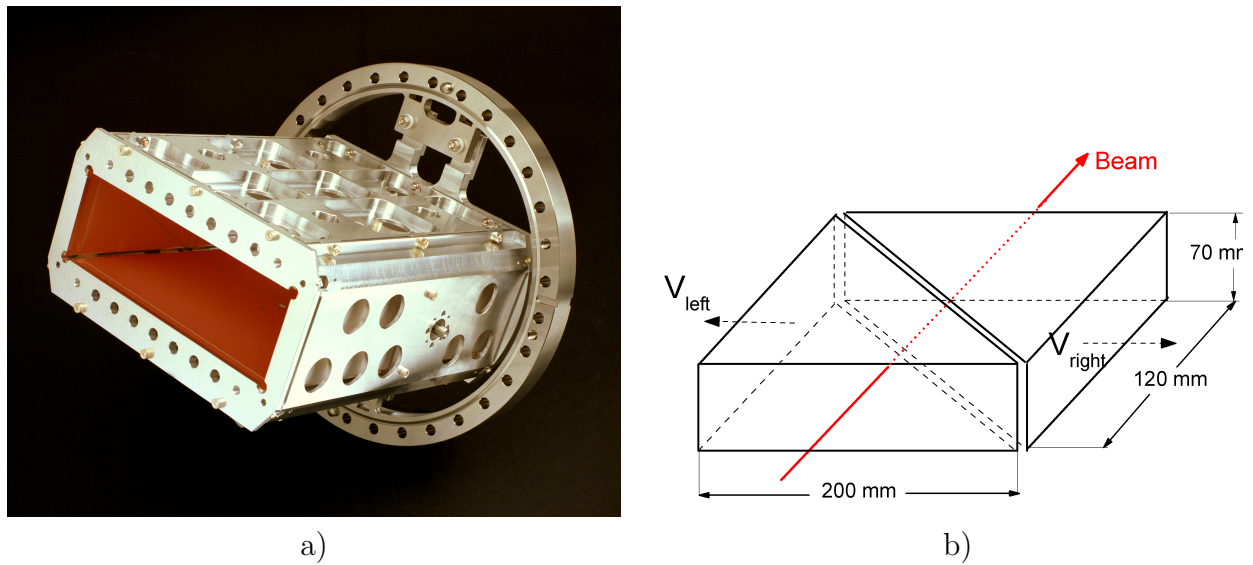


Figure 5.5: a) One of the BPM in SIS, installed in 1988. (Courtesy: Mr.Achim Zschau)
 b) The conceptual diagram of BPM shows the voltages picked by its left and right plates. From the amplified signal, sum signal is collected for the measurements.

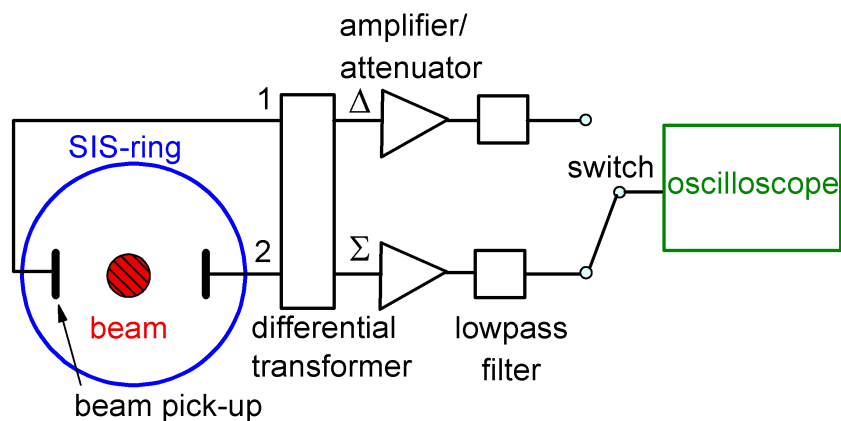


Figure 5.6: The Electronic scheme for longitudinal beam pick-up. The beam signal is detected by pick-up plates and collected by using a differential transformer. Then this signal is amplified or attenuated depending upon the level of its strength. Further all the signals below the cutoff frequency of pick-up [88] are filtered. The sum signal is collected, by using a switch, to observe the longitudinal beam profile in an oscilloscope.

charge or potential by the electric field of the beam on two opposite (left and right) metal plates (or electrodes). With higher potential on the nearer one (to beam) and lower on the opposite, the sum of the potentials $V_{left} + V_{right}$ remains constant and depends only upon

the beam current.

The processing electronics is an integral part of the BPM system and it should be so as not to influence the beam signal. The BPM system in SIS uses a broadband processing electronics as shown in Fig. 5.6. The record for the bunch shape benefits with high time resolution. The analog signal from individual plates is amplified or attenuated to bring it to the ADC input level. The final digital output from ADC has to be used to calculate the strength of sum or difference signals. These signals are analogously generated by a differential transformer [83]. The digital bunch signals are easy for handling and post processing.

The time-domain information of bunch signal is recorded by using “WaveRunner 4395A” Lecroy oscilloscope. The measurements are profitted from the segmented memory of these modern digital storage oscilloscopes, where the data can be recorded with the sampling rate up to 5 GHz. They can record up to 10000 traces, and each of them can be triggered individually. This property facilitates the recording for evolution of bunch form for times much more than synchrotron period. Keeping the memory capacity of oscilloscope in mind, the data is stored in binary format ('trc'). By using a software tool provided by Lecroy, this data is converted to ASCII format('txt'). Then by using a visual basic based programme [96], the point information is replaced by the corresponding time axis.

5.3 Schottky pick-up

The Schottky pick-up was first installed in ESR and is described in Ref.[90]. Recently a replica of this is mounted and tested for SIS as well [89]. The detecting probes for the

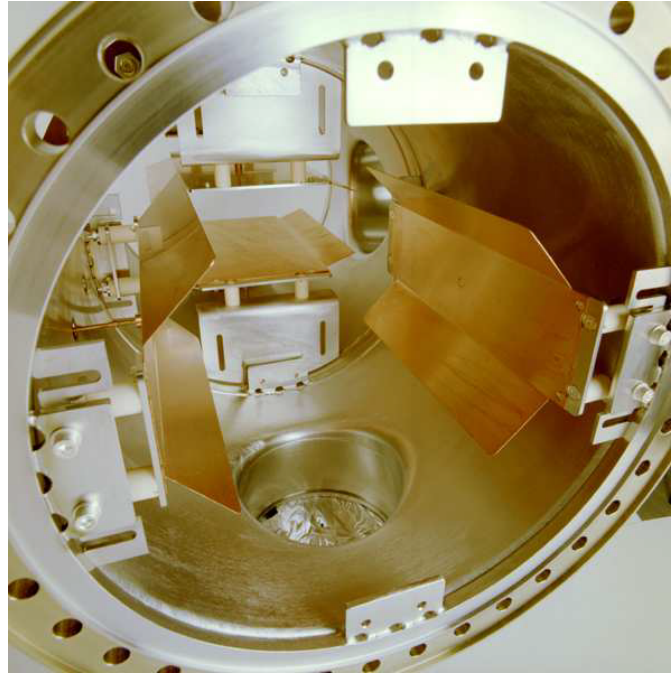


Figure 5.7: A photograph of Schottky pick-up in Experimental Storage Ring (ESR) at GSI. (Courtesy: Mr.Achim Zschau)

Schottky signal from the beam are two plate capacitors. The concave shaped plates, shown in Fig. 5.7, are oriented horizontally and vertically to form the capacitors in respective planes. The sensitivity of detector probe can be adjusted by varying the distance between the plates. This electrostatic pick-up detects the image currents induced by beam which depends on the beam velocity [91]. A schematic diagram of Schottky pick-up is shown in Fig. 5.8. During the measurements, a lower frequency cut off of 10 MHz is to be set so that the signal to noise ratio drops and comes in the non-linear region of amplifier characteristic [90, 93]. For longitudinal measurement the sum signal is measured by using a real time spectrum analyzer, RSA3303A, from Tektronix. Out of several operational mode of this device the real time mode is chosen because, only for this mode it can be triggered externally [92]. External triggering is required to synchronize the data acquisition to the required instant in the synchrotron cycle mentioned in Fig. 2.4.

The frequency span in the device can be chosen but in definite steps of 2, 5, 10-fold, and so on, of 100 Hz. The center of measurement and the measuring time (duration for data acquisition) can also be chosen. After triggering, the device acquires the data for the

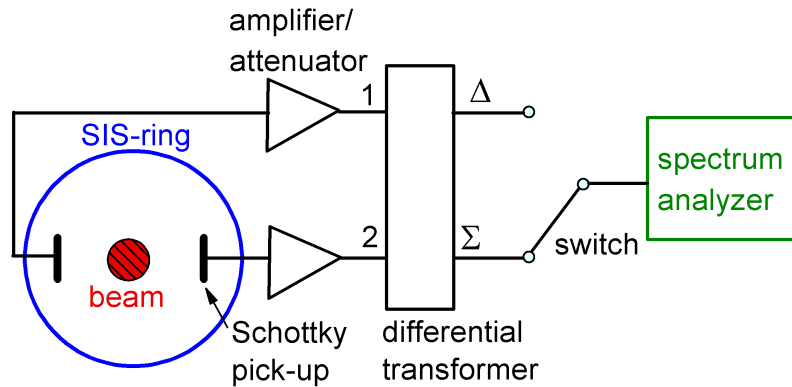


Figure 5.8: The electronic scheme for Schottky pick-up, showing that the beam signal is collected by this pick-up. Then the signal is amplified or attenuated depending upon the signal level. Further, for the information in longitudinal plane, the digital sum signal is selected by a switch and is observed using a spectrum analyzer.

whole measuring time, which was chosen from the injection till the end of the designed ramp (Subsec. 6.2.2).

The data in the spectrum analyzer is saved in binary format ('iqt'). By using ReadIQT, a software provided by Tektronix [92], these files are converted to ASCII ('txt') format. The span or frames can be chosen for the conversion and for further averaging as per the requirement. The number of frames in full data set, called block, is given by the ratio of measuring time to the frame time. Several hundreds of frames are to be averaged to extract a clear Schottky spectrum. A C++ programme is used for this purpose, the details about it are mentioned in Ref [75]. A mathematica programme [94] is developed and used to extract the rms momentum spread by using the averaged Schottky spectrum.

5.4 Digital Signal Processor System

A Digital Signal Processing (DSP) system (made in Sundance Multiprocessor Technology) has been programmed at GSI [98, 99] with the purpose of beam phase control and cavity synchronization. It is used to synchronize the cavities for double rf operation and to observe the additional phase information under the influence of beam loading.

A sketch of the DSP phase measurement system is shown in Fig. 5.9. With the purpose of beam phase control, specifically for correcting the dipole oscillations in bunch, the phase difference between a gap signal and the signal from longitudinal pick-up is used as an input signal. For cavity synchronization the gap signals from both ferrite cavities

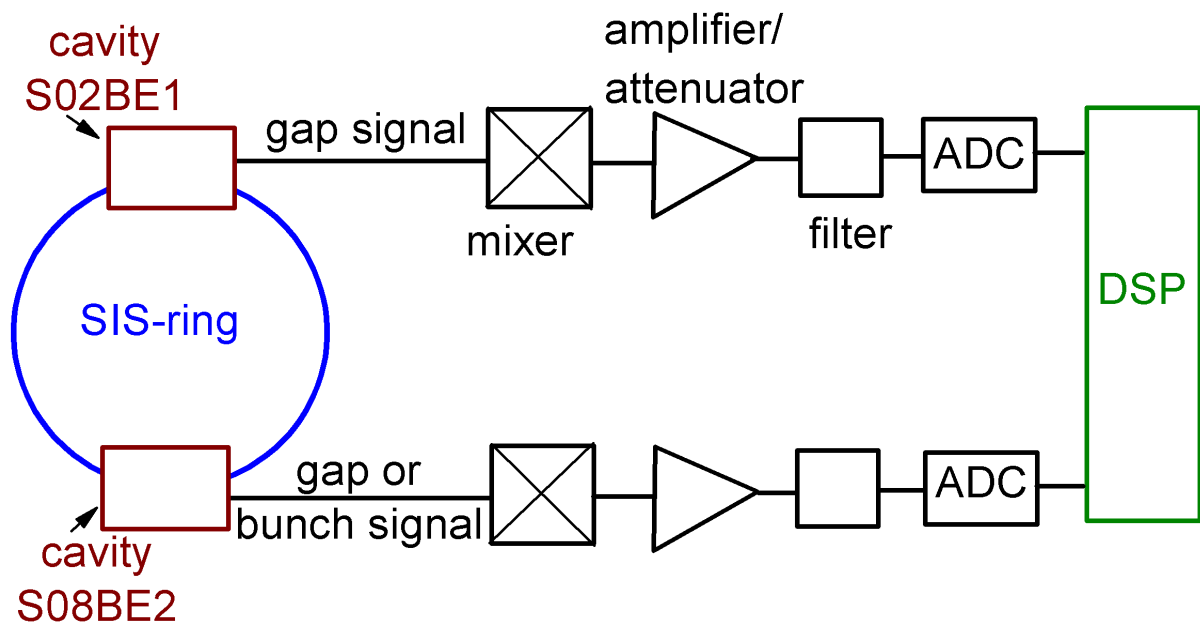


Figure 5.9: The scheme connecting the cavity or beam signals to DSP system in SIS. The phase difference, ϕ , between gap signals of the cavities (Fig. 2.2), is measured by DSP unit.

(Fig. 2.2) are compared and the phase difference between them is corrected [30]. After frequency conversion of the swept frequency signal to a fixed intermediate frequency (IF) and amplification, both signals are digitized and fed to a DSP unit which calculates the difference between signals numerically. The DSP system performs narrow-band detection which guarantees the correct phase measurement even for noisy signals. The accuracy of the phase detected by the DSP measurements system is better than $\pm 1^\circ$ [99].

Chapter 6

Adiabatic Capture in SIS

An unbunched charged particle beam i.e. coasting or dc beam in SIS is captured by ‘switching ON’ the rf voltage precisely slow enough so as to preserve the beam quality or the longitudinal emittance (Subsec. 3.3.1) during the whole capturing process. This is known as the adiabatic capture [50, 59] of the dc beam. Here, adiabatic capture study is aimed to assure the beam quality. While to study the longitudinal intensity effects (Sec. 4.1 and 4.2) remains the primary objective of this work, adiabatic capturing of coasting beam remains an essential pre-requisite to ensure that for any undesirable effect on beam quality and beam stability. In this context, an analysis of capture study carries a special significance before the study of the intensity effects.

Initially, several types of voltage-amplitude ramps based on the linear variation of different phase space parameters are explained and a factor quantifying the emittance dilution in the capturing process is introduced. It is followed by the theoretical and simulation studies on the influence of amplitude of initial voltage on the capturing process. Further, as the performance of the different ramps are tested in measurements and simulation, the measurement method and parameter settings are explained. Thereafter, the observations and results for both, single and double rf systems, are presented in the dedicated section for each.

6.1 Principle of capture study

The reference time scale for the particle motion in the longitudinal phase space is the period of synchrotron motion T_s (Sec. 3.2). For the adiabatic capture, the increase in the amplitude of the rf voltage V_0 should be slow enough to result in a linear variation of the phase space parameters, T_s and ω_s [50, 59, 61], which helps to preserve the emittance. In phase space, T_s (synchrotron period) is the property of an individual particle and ω_s (synchrotron frequency) is the property of collection of particles, which directly influences the bucket height (Eq. 3.14).

The appropriate choice and limiting values of the parameters of amplitude ramp i.e. ramping time t_{ramp} , time to ‘full-turn-ON’ for V_0 and its initial and final values, V_i and V_f

respectively, depends upon the specific accelerator and its settings. For example, the limited machine cycle (Fig. 2.4), decided by the required frequency of the particle extraction, restricts the higher limit of the t_{ramp} and a too fast capture results in the filamentation and emittance blow up (Subsec. 3.3.2). The number of particles captured sets the lower limit and the bunching factor (Subsec. 3.3.3) sets the higher limit for the final value, V_f of the rf voltage V_0 [50]. Apart from the above mentioned ramp parameters, the voltage amplitude vs time function i.e. V_0 vs t_{ramp} has a vital role to play in adiabatic capture [59]. Different types of ramps are defined on the basis of this relation.

6.1.1 RF amplitude ramps and dilution factor

Several functions are derived by using the different properties belong to the single particle (T_s) or to the collection of particles (ω_s) in phase space. With conditions like $dT_s/dt \gg 1$, $d\omega_s/dt \gg 1$ and a linear rise from V_i to V_f for the adiabatic capture. Using these conditions the iso-adiabatic, parabolic and linear types of ramps are derived and a **Dilution Factor** (DF) is introduced to compare their relative performance. DF quantifies the increase of the emittance in the capturing process, and hereby is the criterion for comparing the performance of the ramps.

Iso-adiabatic ramp

Here the condition of linear variations in T_s , with time is applied to derive the rf amplitude variations as follows:

$$\alpha_{ia} = \frac{1}{2\pi} \left| \frac{dT_s}{dt} \right| = \left| \frac{1}{\omega_s^2} \frac{d\omega_s}{dt} \right| \ll 1, \quad (6.1)$$

where α_{ia} is the coefficient introduced for the iso-adiabatic ramp. By using the condition in Eq. 6.1, the form of the amplitude ramp can be obtained. T_s is related to the rf voltage amplitude as $T_s = 2\pi AV^{-1/2}$ with $A = \sqrt{LRm^*/hq}$ and it can be expressed as a differential equation

$$\alpha_{ia} dt = \frac{1}{2} AV^{-3/2} dV. \quad (6.2)$$

Thus for the above mentioned ramp parameters, the α_{ia} is obtained as

$$\alpha_{ia} = A \frac{1}{t_{ramp}} \left(\frac{1}{\sqrt{V_i}} - \frac{1}{\sqrt{V_f}} \right)$$

and an indefinite integration of the relation in Eq. 6.2, gives the ramp form as $\alpha_{ia}t + C = AV^{-1/2}$. By using the α_{ia} , voltage amplitude at any instant on the ramp is obtained as

$$V(t) = \frac{1}{\left(\frac{t}{t_{ramp}} \left(\frac{1}{\sqrt{V_i}} - \frac{1}{\sqrt{V_f}} \right) + C \right)^2},$$

where, the constant C is calculated by applying a boundary condition $V(t_{ramp}) = V_f$ (or $V(0) = V_i$). By putting the constant C , the relation for the iso-adiabatic ramp

$$V(t) = \frac{V_i}{\left(1 - \frac{t}{t_{ramp}} \frac{\sqrt{V_f} - \sqrt{V_i}}{\sqrt{V_f}}\right)^2}, \quad (6.3)$$

is obtained, which is shown in Fig. 6.1 with α_{ia} of 0.1, for t_{ramp} of 100 ms against T_s of 0.6 ms.

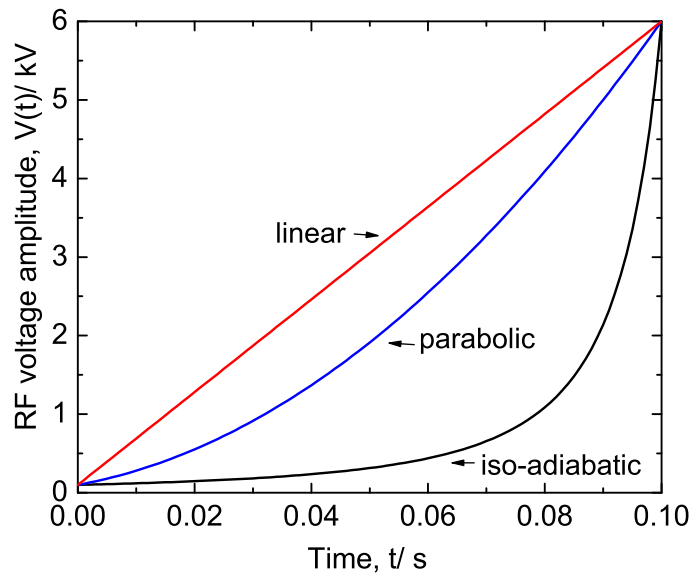


Figure 6.1: The iso-adiabatic, parabolic and linear ramps are drawn with $V_i = 100$ V, $V_f = 6$ kV and the ramping time $t_{ramp} = 100$ ms.

Parabolic ramp

This ramp assumes the condition of linear increase in the bucket height (Eq. 3.14), applied through the consideration of the linear variation in the ω_s with time i.e.

$$\alpha_{par} = \left| \frac{d\omega_s}{dt} \right| \ll 1, \quad (6.4)$$

where α_{par} is the coefficient introduced for the parabolic ramp. The ω_s is related to the amplitude of rf voltage as $\omega_s = 2\sqrt{V}/A$, this relation is expressed as a differential equation

$$\alpha_{par} dt = \frac{1}{2A} V^{-1/2} dV.$$

By integrating it to the limits of the mentioned ramp parameters, we get

$$\alpha_{par} = \frac{1}{t_{ramp}A}(\sqrt{V_f} - \sqrt{V_i}),$$

and to derive the voltage amplitude, an indefinite integration of the mentioned differential equation is done, which gives

$$\alpha_{par}t + C' = \frac{1}{A}\sqrt{V},$$

where C' is the constant derived by applying the similar boundary condition as that for the iso-adiabatic ramp (Eq. 6.3). By using the constant C' , the parabolic voltage amplitude ramp is expressed as

$$V(t) = \left(\sqrt{V_i} + \frac{t}{t_{ramp}}(\sqrt{V_f} - \sqrt{V_i})\right)^2, \quad (6.5)$$

which is shown in Fig. 6.1.

Linear ramp

A consideration of the linear increase in the amplitude of the rf voltage from V_i to V_f in time t_{ramp} , results in a linear ramp

$$V(t) = V_i + \frac{t}{t_{ramp}}(V_f - V_i), \quad (6.6)$$

which is shown in Fig. 6.1.

Dilution factor

In order to quantify the influence of these capturing ramp parameters on the longitudinal phase space area, a parameter called ‘**Dilution Factor**’ (**DF**) is defined here. It gives the dilution in the longitudinal phase space area of coasting beam before capture due to the capturing process and is the ratio of bunched beam area, S_{bunch} (Eq. 3.23), at the end of capture to the coasting beam area, S_{coast} (Eq. 3.22), in phase space (Fig. 6.2).

$$DF = \frac{S_{bunch}}{S_{coast}}. \quad (6.7)$$

In measurements, these areas are derived either by using the definition of rms emittance (Eq. 3.21) or depending on the type of fit, the definition of fitted emittances is used.

The experiments and ESME simulations (Sec. 4.6) have been performed to test these ramps (Eq. 6.3, 6.5 and 6.6) for different t_{ramp} by comparing the DF resulted from them and this way the ramp parameters are optimized for the adiabatic capture of dc beam in SIS.

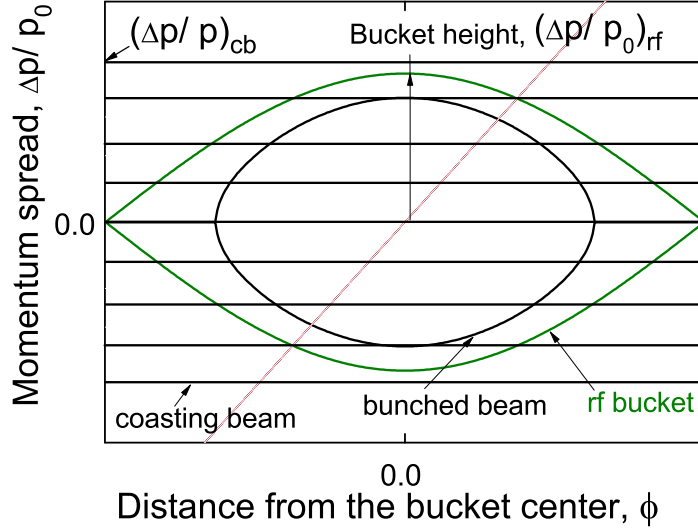


Figure 6.2: A qualitative demonstration of phase space showing the coasting and bunched beams and the bucket created by the initial voltage.

6.1.2 Initial voltage and momentum spread

Apart from the type of ramp and the ramping time, the initial voltage V_i is also an important parameter to be considered during the capturing process. An imperfection in the phase space (e.g. in Fig. 3.6) is caused by it, if the height of the bucket (Eq. 3.14) created by the V_i is higher than the momentum spread, $(\Delta p/p)_{cb}$, of the coasting beam before capture (Fig. 6.2) and results in a non-adiabatic capture. From the simulations (Fig. 6.3) it is observed that the dilution factor is not only a function of the V_i but also depends upon the $(\Delta p/p)_{cb}$ and indicates that for an adiabatic capture, the meticulous choice of V_i is important. A parameter connecting the V_i to the coasting beam properties, defining its choice for the given coasting beam is introduced as a **scaling parameter**,

$$\chi = \frac{\delta_{cb}}{(\Delta p/p_0)_{rf}}, \quad (6.8)$$

where δ_{cb} is the rms momentum spread of the coasting beam (Subsec. 3.3.1) and $(\Delta p/p_0)_{rf}$ is the bucket height (Fig. 6.2), created by V_i . Further,

$$\chi = \eta\beta c \sqrt{\frac{\pi m^* h}{10q}} \frac{(\Delta p/p)_{cb}}{\sqrt{V_i}},$$

with all the coefficients have the similar meaning as mentioned in Sec. 3.2. The simulations are carried out for the different ion species showed the relation of dilution factor with the

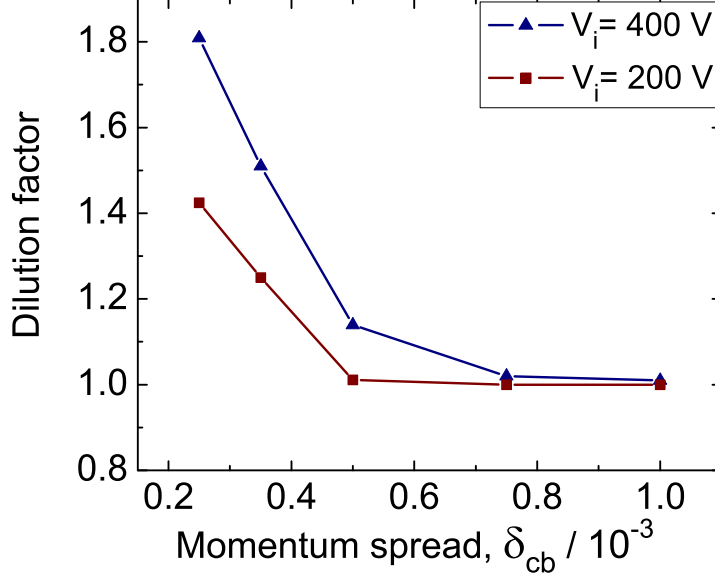


Figure 6.3: The dependence of dilution factor on momentum spread of coasting beam is varying with the amplitude of initial voltage.

parameter χ (Fig. 6.4), and

$$DF = \frac{S_{bunch}}{S_{coast}} = 1 + \frac{f(\chi)}{\chi}, \quad (6.9)$$

where $f(\chi)$ includes the imperfection in phase space introduced by the V_i and for $f(\chi) \leq 0$ there will be no emittance growth. It is defined as an empirical relation

$$f(\chi) = 0.3 - 0.7\chi,$$

for $\chi \leq \chi_{th}$, and found in good agreement with the simulation results (Fig. 6.4). Further, a threshold for χ i.e. $\chi_{th} \approx 0.43$ is defined so that, a coasting beam with any value $\chi > \chi_{th}$ has no influence of the initial voltage on its capturing process.

There are certain limitations with the choice of V_i i.e. the activation of different electronic circuits in SIS rf system demands for a minimum voltage of 100 V [36] restricts the lower limit for V_i . Also, the $(\Delta p/p)_{cb}$ has quite frequent fluctuations in SIS. Therefore, the above mentioned simulation and theoretical study is helpful to provide a limiting value of initial voltage for the given coasting beam parameters, which is further verified by the measurements.

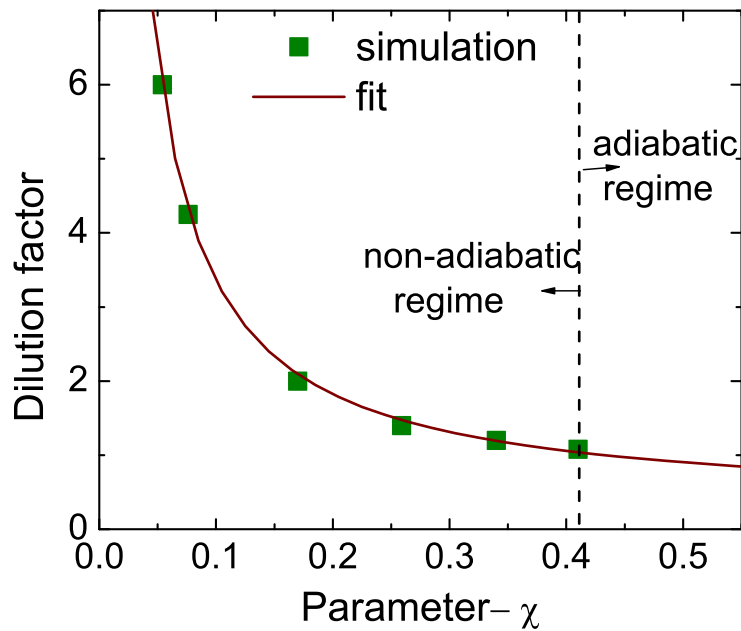


Figure 6.4: Simulations showing χ for different ion-species. A threshold value of separating the adiabatic and non-adiabatic regime is shown as 0.43, irrespective of the ion-species and the beam intensity.

6.2 Capture measurements

The coasting beam in SIS is captured in the stationary bucket formed at injection energy (Subsec. 3.2.2). The adiabatic capture study in this work is aimed to measure the emittance of the ion beam before starting and at the end of the capturing process at this constant energy. A change in the emittance in case of different types of ramps, represented by Eq. 6.3, 6.5 and 6.6, for a range of a ramping times have been compared. Along with the emittance change, bunch form and beam stability are also the important aspects to be assured for the adiabatic capture [56, 57]. Therefore, the beam signal and its evolution with time have been observed.

In upgraded SIS, srf system will be replaced by the drf one (Subsec. 3.3.3). Hence, the measurements for the capture have been performed with drf system as well. Two ferrite cavities working at different frequencies (Fig. 3.7) were ‘switched ON’ simultaneously and synchronized by using DSP system (Sec. 5.4).

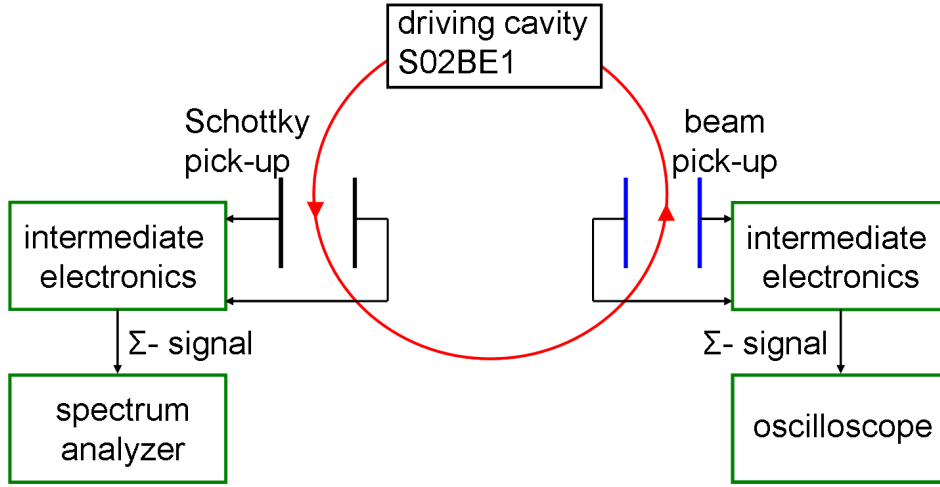


Figure 6.5: A schematic diagram showing the different longitudinal diagnostics and measuring instruments used during the capture study. The other ferrite cavity, S08BE2, in SIS ring (Fig. 2.2) is also activated for the double rf operation. It is kept short-circuited during srf measurements.

6.2.1 Measurement method

Emittance of the coasting beam is a function of its momentum spread. A Schottky signal from the coasting beam (Fig. 2.4) is collected before capture by using the Schottky pick-up in SIS ring (Fig. 5.7). A scheme for the capturing set-up is shown in Fig. 6.5. This is the frequency domain information from the beam in longitudinal direction for which the sum signal from the Schottky pick-up is collected through some intermediate electronics shown in Fig. 5.8. A Sony-Tektronix 3066 fast spectrum analyzer was used to observe this signal. The conversion to linear power scaling, averaging and fitting of an averaged signal to a certain distribution gives the momentum spread of the coasting beam. The details about this pick-up and the post processing of the data are mentioned in Sec. 5.3.

Emittance for a stationary bunch is a function of its bunch length (Eq. 3.23), which is derived by processing the longitudinal (sum) signal from beam pick up (BPM) in SIS ring (Fig. 5.5 a). The details about BPM, right from the data collection to its post processing, are explained in Sec. 5.2. This time-domain information of the beam signal is observed by using an oscilloscope as shown in Fig. 6.5. Both the instruments, the oscilloscope and the spectrum analyzer are triggered externally at the instant matched to the beam injection to SIS. The bunch form is monitored by using a Lecroy oscilloscope (Fig. 6.6) and to observe the beam stability, segmented memory feature of this oscilloscope (Sec. 5.2) is used.

Using the definition of the ramps in equations 6.3, 6.5 and 6.6, a data-table consisting of the voltage amplitude and time information is created. This data-sheet is fed remotely to the Arbitrary Waveform Generator (AWG) and the generated ramp is then fed to the driving cavity or cavities in case of drf system. The same oscilloscope (Fig. 6.6) is

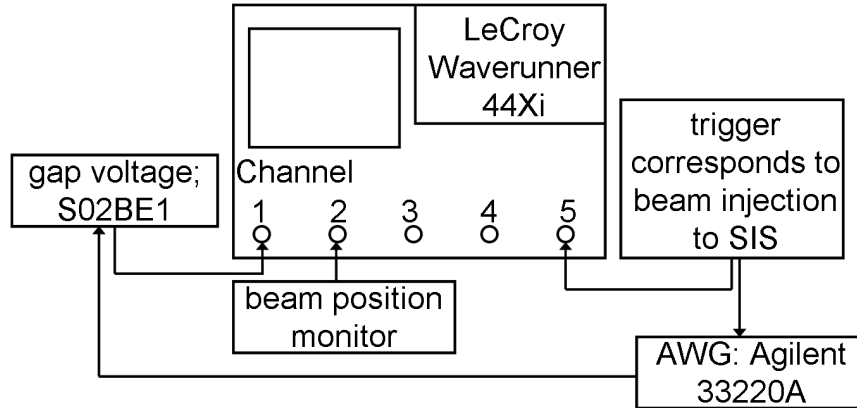


Figure 6.6: A block diagram showing the signals measured by using the oscilloscope. For double rf operation, the ramp is fed to the S08BE2 (in Fig. 2.2) cavity and then its gap-signal is measured, additionally.

used to observe the time domain information from the beam and the gap signals from the cavity (or cavities). After deriving both the coasting and bunched beam emittances from the measured data, a dilution factor is calculated by using Eq. 6.7. Same procedure is followed for all the three types of ramp and both the rf systems.

6.2.2 Settings of parameters

Machine, beam and cavity (or rf ramp) parameters are the main constituents of the measurement settings. These parameters, for the experiments with both the single and drf system, are shown in the Table 6.1. The beam intensity is kept constant but, to keep check on its fluctuations, it is constantly recorded during measurements. For each experiment the energy was kept constant and the frequency f_{rf} was matched to the corresponding beam energy. The energy and frequency mismatch is one of the sources of bunch oscillations which disturbs the bunch stability at capture [61].

Single and double rf ramp settings

A long injection plateau (Fig. 2.4) of 2 s is set to apply the self-designed rf amplitude ramps for capturing and bunching. Nearly 100 ms delay is provided, before initiating the capture, to collect the information from the coasting beam. The data from the bunched beam is collected on the flat-top followed by the capturing ramp. A de-bunching ramp leaves the coasting beam in the machine, which follows the further machine cycle as per the routine SIS operation (Fig. 2.4). Also a non-zero (100 V) initial voltage can be observed in the ramp (Fig. 6.7), which has to fulfill the biasing requirement of the control system in the rf cavity [36]. For bunch stability, the frequency of the amplitude ramps is matched to the energy, as mentioned in the Table 6.1.

Parameter	Single rf setting	Double rf setting
Ion species	Ar ¹⁸⁺ , Ta ⁶¹⁺	Ta ⁶¹⁺
Energy/ MeV/u	11.4, 11.149	11.149
Beam intensity/ ppc	$\approx 2 \times 10^{10}$, $\approx 4 \times 10^9$	$\approx 4 \times 10^9$
Harmonic number	4	4, 8
Rf frequency/ f_{rf} / kHz	857.9, 848.33	848.33, 1696.66
Initial voltage/ V_i / V	100 to 800	100
Final voltage/ V_f / kV	6	8, 4
Ramping time/ t_{ramp} / ms	2 to 20	10 to 100

Table 6.1: Machine, beam and rf parameters settings during the experiment. The energy is kept constant but has different value during each measurement. The ppc is the number of particles per cycle. The V_i is varied from the 100 to 800 V for the single rf system but the V_f is kept constant.

An example of rf amplitude ramp *for the srf system* is shown in Fig. 6.7. It is feeded to

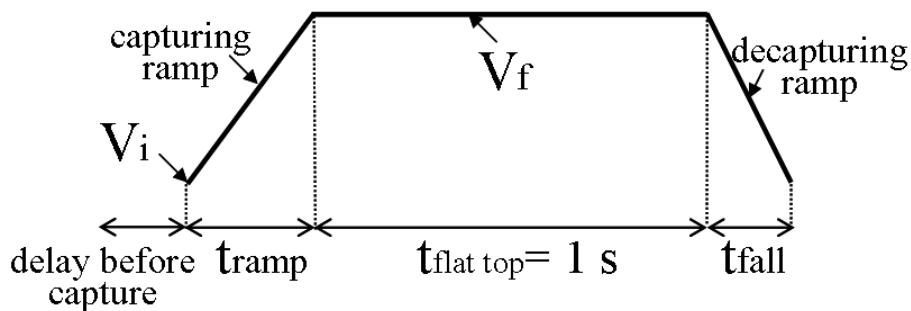


Figure 6.7: An example of rf cycle used for capture study showing a linear capturing ramp.

the driving cavity, i.e. S02BE1 in Fig. 6.5 and the other cavity in SIS ring (Fig. 2.2) is short circuited.

For the double rf system, the iso-adiabatic ramp mentioned in Eq. 6.3 is used separately

for both the cavities and both the ramps, representing harmonic 4 and 8 of f_0 , are started at the same instant (Fig. 6.8). To assure the stability of the double rf system, the two

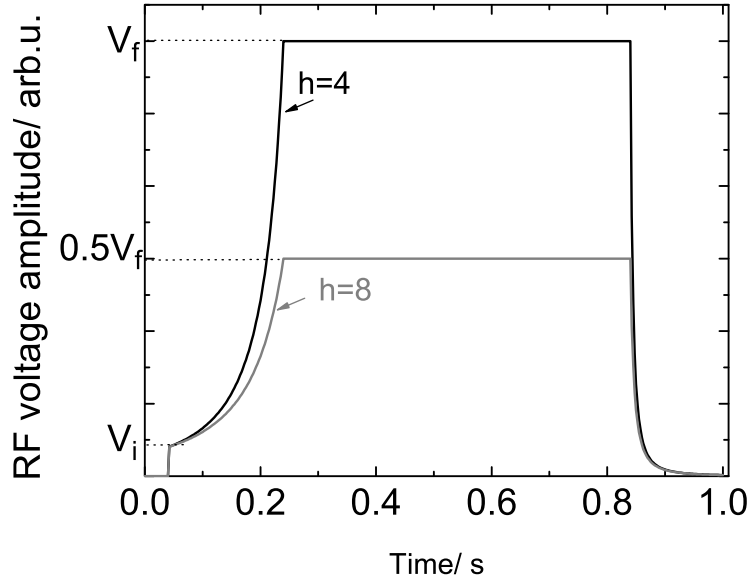


Figure 6.8: An example of the rf ramps used for the capture study with double rf system. Both ramps started simultaneously. For the upgraded SIS the harmonic numbers, $h=4, 8$ are replaced by $h=2, 4$.

cavities must work in synchronism [98, 99]. Therefore, a DSP system (Sec. 5.4) is used to correct the phase difference between the two cavity gap-signals and thus to synchronize them.

6.2.3 Simulation settings

ESME, the simulation code used in this study (Sec. 4.6) uses the parameters mentioned in the Table 6.1. The cavity settings for single and double rf systems are done separately and the synchronism of the cavities in case of double rf system is inherently adapted in it. The rf amplitude ramps, explained in previous section, are used here for capturing. The rms emittance (Eq. 3.21) in ESME, for the bunched beam, is calculated by limiting the bunch with the boundaries of 98%, which can influence the calculation of dilution factor here. In the simulations, the influence of the beam intensity is added by inserting both of the longitudinal intensity effects (Secs. 4.1 and 4.2).

6.3 Observation and results

In this section, the measurement and simulation results of the dilution factor for different type of ramps, their corresponding bunch forms and waterfall curves showing bunch evolution are presented for both the rf systems. Initially the ramp parameters are optimized for the srf system and then the influence of the V_i on the bunched beam, produced by this optimized ramp, is presented in the same section. At this stage, the parameters for the amplitude ramp will be optimized for the adiabatic capture with srf. Thereafter, similar observations are presented for the drf system, but only for the optimized ramp. Then the optimized ramp parameters for the drf systems are tested in simulations for SIS with the upgraded parameters (Sec. 2.11).

6.3.1 Single rf system

As mentioned in subsection 6.2.2, Schottky signal from the coasting beam was measured and fitted to a Gaussian function (Sec. 3.3) as shown in Fig. 6.9 a. The frequency in

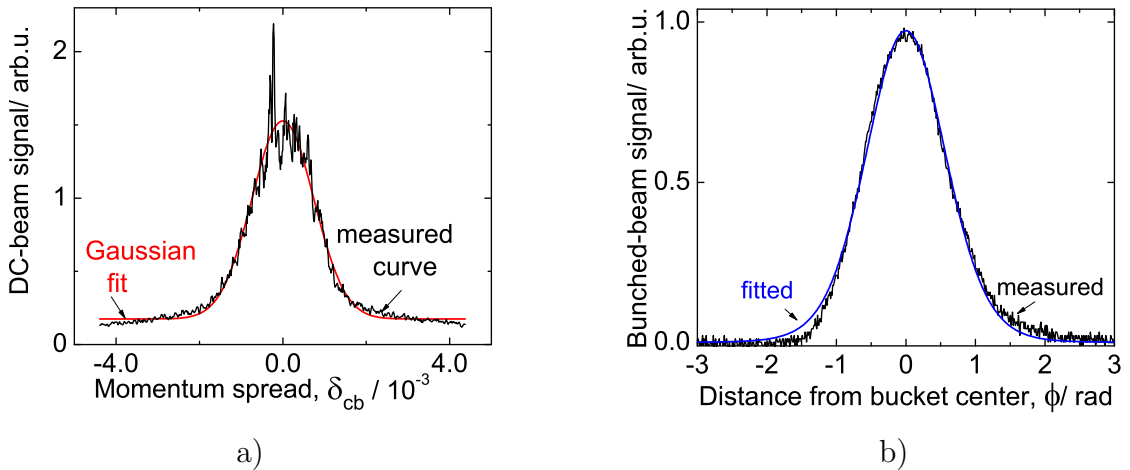


Figure 6.9: a) A Schottky signal from the coasting beam. b) A bunched-beam signal from the longitudinal pick-up is fitted to the corresponding Gaussian distribution.

abscissa in Schottky measurements is converted into the momentum spread (Eq. 3.9). It is plotted against the power that goes with the coasting beam. In SIS, the ion species, the beam intensity and its adjustment by varying the chopper window are the common sources of variations in the momentum spread [63]. As the ion species and beam intensity are kept constant and the chopper window was also fixed, the momentum spread was also nearly constant during the whole experiment.

The longitudinal beam signal as observed in the oscilloscope is shown in Fig. 6.9 b. Its abscissa is the bunch length and the ordinate is the bunch signal with magnitude

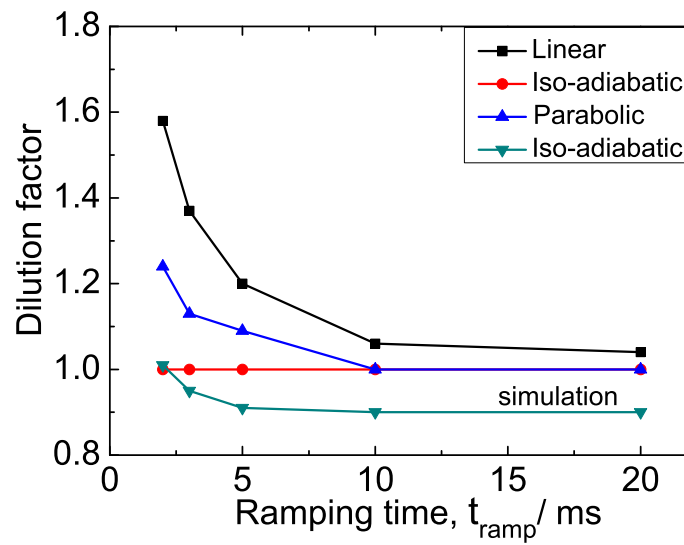


Figure 6.10: Measurement result showing variation in the DF with the t_{ramp} . One simulation result for the iso adiabatic ramp is added, and is showing that for the whole range of t_{ramp} the DF is ≤ 1 .

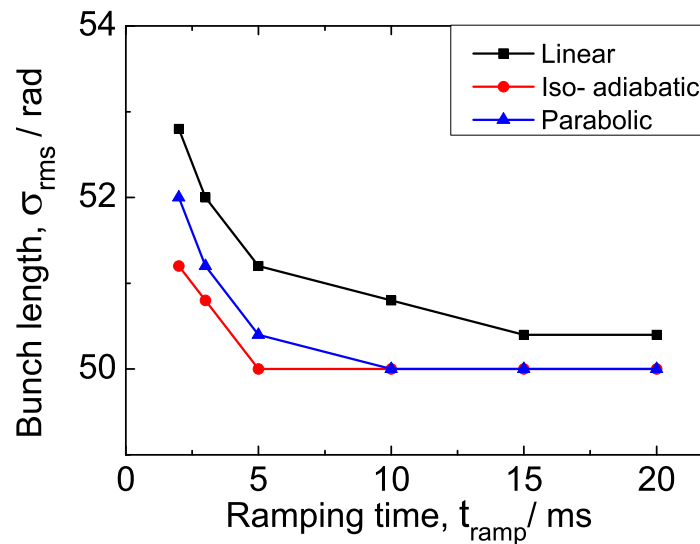


Figure 6.11: Simulation result showing variation in the rms bunch length, σ_{rms} with ramping time.

depending on the gain of the pick-up circuitry. The tails observed are restricted by the

lower sensing limit of the pick-up. The figure shows the Gaussian fitting of measurement data. It gives the rms momentum spread δ_{cb} , which in turn is used to calculate the rms emittance of the coasting beam.

By using these above emittances the dilution factor is calculated by using Eq. 6.7. It is plotted for several variables as shown in Fig. 6.10. Initially a high DF is observed for linear and parabolic ramps. Iso-adiabatic ramps give the lowest dilution factor of 1 for the whole range of variations in t_{ramp} including those low ramping times ($\simeq T_s$). In simulation, the dilution factor of < 1 is distinctively noticeable (Fig. 6.10). Particles inside the bunch

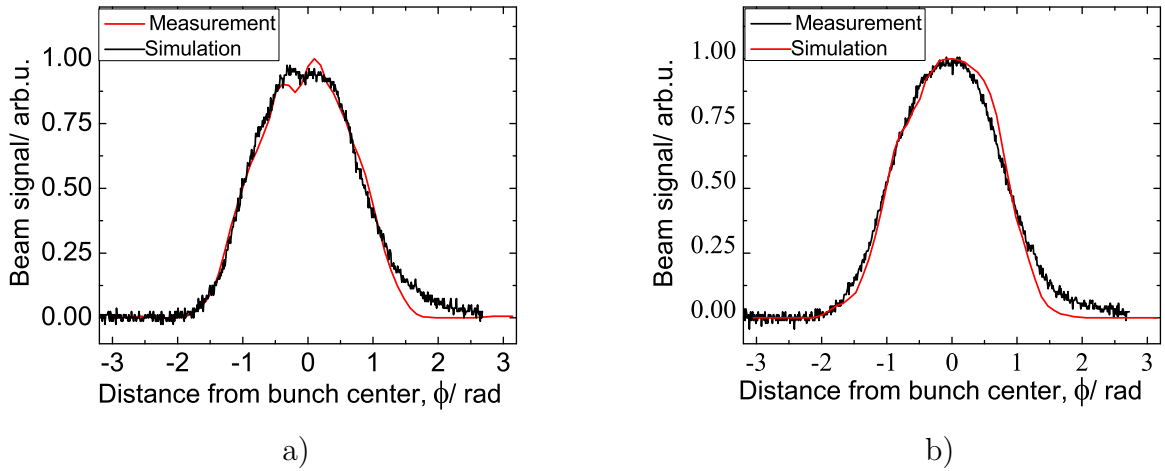


Figure 6.12: Bunch forms from measurements and simulations, a) For t_{ramp} of 3 ms and b) For t_{ramp} of 20 ms, with an iso-adiabatic ramp.

boundary are considered while the contribution of the particles beyond the boundary is not included in the calculations (Subsec. 6.2.3). This is because of the method used for calculating the rms emittance in ESME (Eq. 3.21). As no such boundary exists for the coasting beam, all the particles are accounted in the calculations for its phase space area. Therefore, the bunched beam area is lower than the coasting beam area and the DF is < 1 . In this condition, the bunch lengths, σ_{rms} are plotted for the different types of ramps and a range of t_{ramp} instead of the DF (Fig. 6.11). It is worth because for the constant $(\Delta p/p)_{cb}$, the DF depends only upon the bunch length (Eq. 3.23). The Fig. 6.11 is qualitatively supporting the measurements in Fig. 6.10 e.g. the linear ramp giving the largest σ_{rms} and for all $t_{ramp} > 10$ ms all ramps have nearly similar σ_{rms} .

Further, the bunch forms for different t_{ramp} are compared for both simulations and the measurements. In Fig. 6.10, the DF for the iso adiabatic ramp is ≤ 1 for a t_{ramp} of ≥ 3 ms, but, the bunch form for this case, shown in Fig. 6.12 a, is distorted. It is to be noted that 2 ms is quite often the choice for t_{ramp} for the capture in SIS [36]. For the ramping times ≥ 10 ms all ramps have approximately similar performance in terms of dilution factor and σ_{rms} (Figs. 6.10, 6.11). A clean bunch formed with iso-adiabatic ramp with t_{ramp} of 20

ms is shown in Fig. 6.12 b. The time evolution of the bunched beam is observed in the

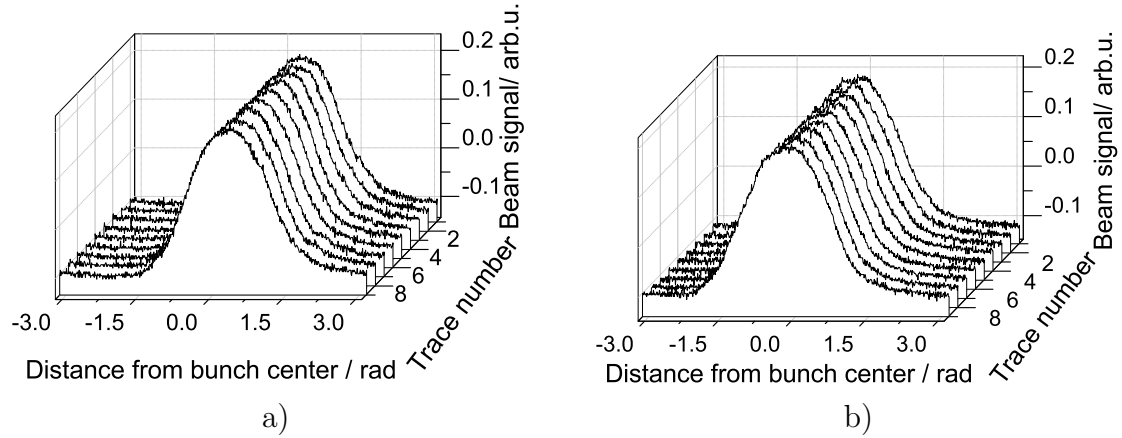


Figure 6.13: Different waterfall curves showing no oscillations in the bunched beam, where capturing is performed using the ramp parameters $t_{ramp} = 20$ ms, $V_i = 100$ V and $V_f = 6$ kV, with iso-adiabatic ramp in Fig.(a) and a linear ramp in Fig.(b).

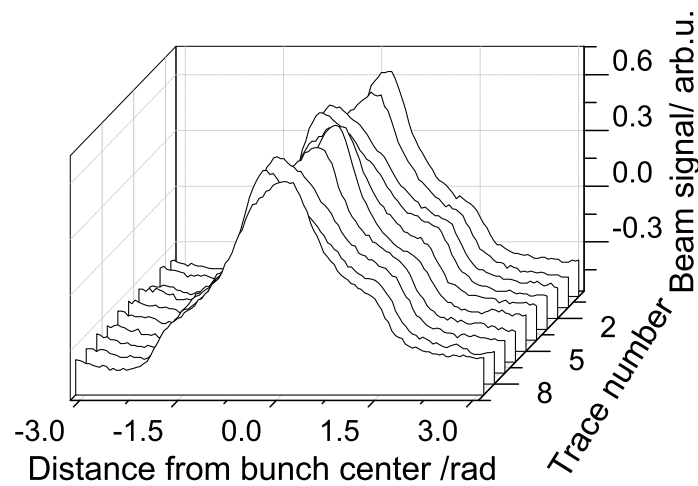


Figure 6.14: Oscillations in the bunch evolution with time are observed for Ta^{61+} (Table 6.1), which is captured by using an iso-adiabatic ramp with t_{ramp} of 50 ms and V_f of 6 kV.

waterfall curves shown in Fig. 6.13. Two examples for iso-adiabatic and linear type of ramps, with t_{ramp} of 20 ms, are shown in Fig. 6.13. An identical and stable bunch and the bunch evolution can be observed irrespective of the type of ramp. In the measurements with Ta^{61+} ion (Table 6.1), the oscillations in the bunch peak are observed (Fig. 6.14).

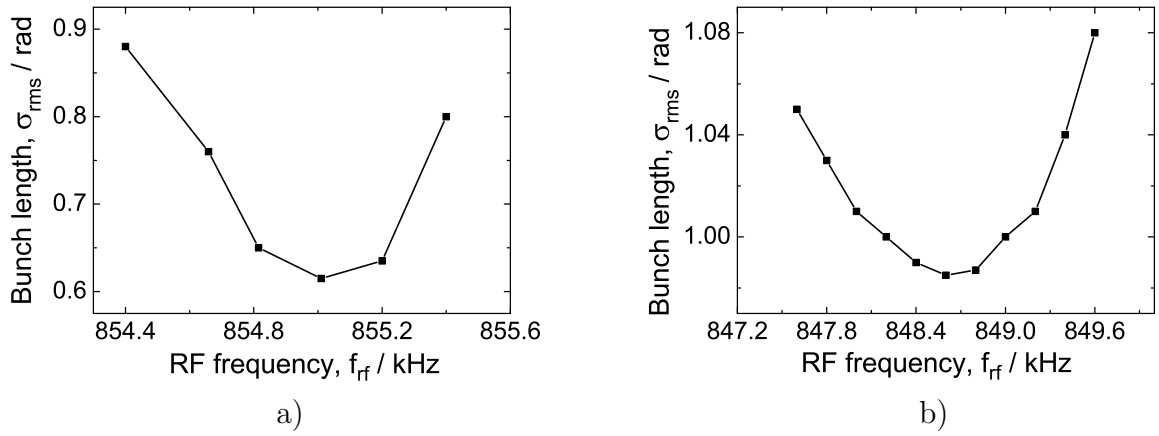


Figure 6.15: a) Illustrates the influence of frequency mismatch on the bunch-length variations in measurements for Ar^{18+} beam. b) A simulation showing the qualitative comparison of the relation between frequency mismatch and bunch-length from measurements (in Fig. a). These simulations are performed for the similar parameters as for Fig. 6.14. The simulation parameters are for Ta^{61+} . In both the above cases, the beams are captured by using the iso-adiabatic ramp.

For the given coasting beam (Fig. 6.9, Table 6.1), the system is well within the Keil-Schnell limit (Subsec. 4.4). It signifies that the bunch oscillations could have been introduced during the beam capturing.

The frequency of the capturing ramp, f_{rf} , is determined by the injection energy, E_{kin} and they must be matched to avoid any bunch oscillations [61]. For the E_{kin} of 11.149 MeV/u, the corresponding f_{rf} is 848.57 kHz. But from the corresponding gap-signal of the cavity, the frequency was found to be 848.33 kHz. This frequency difference (≈ 240 Hz) is understood as the most probable source of the oscillations (Fig. 6.14). The injection energy and rf frequency in SIS are set manually to match them to the extraction energy of UNILAC. Then the rf system along with the ferrite cavity in SIS adjusts the f_{rf} (and f_r) to this energy. The cavity has the bandwidth, f_{bw} (Fig. 2.8) of ≈ 4 kHz, and minor variations in the frequency seems quite feasible.

To further verify this influence of frequency mismatch on bunch, a separate experiment is performed with the varied rf frequency to impose the mismatch and its impact on the bunch. The bunch length variations are then plotted against the f_{rf} (Fig. 6.15 a). The minimum bunch length corresponds to the matched frequency and increases with the difference in either directions. This behavior is qualitatively supported by the simulations (Fig. 6.15 b) performed for the Ta^{61+} beam (Table 6.1).

Influence of the initial voltage

For the parameters mentioned in Table 6.1 with constant V_0 of 6 kV and t_{ramp} of 20 ms for the iso-adiabatic ramp, the variations in the bunch length with V_i are observed (Fig. 6.16). These variations increase with the perturbations introduced by V_i . A growth in the phase space is compared for a V_i of 100 V and 800 V. The simulations with the similar parameters

Initial voltage/ V	χ	Bunch length/ rad
100	0.86	0.78
300	0.5	0.79
800	0.3	0.87

Table 6.2: The scaling parameter χ (Eq. 6.8) is calculated for a constant momentum spread δ_{cb} of $5 \cdot 10^{-4}$ for different initial voltages. It can be seen that χ corresponding to 800 V is lower than its threshold value χ_{th} of 0.43 (Subsec. 6.1.2).

are supporting the measurements, particularly for a V_i of 100 V. It is because the δ_{cb} is taken from the fitting of the coasting beam corresponding to the V_i of 100 V and the same value is used for the other cases as well. The variations in the δ_{cb} , in reality, is the source of

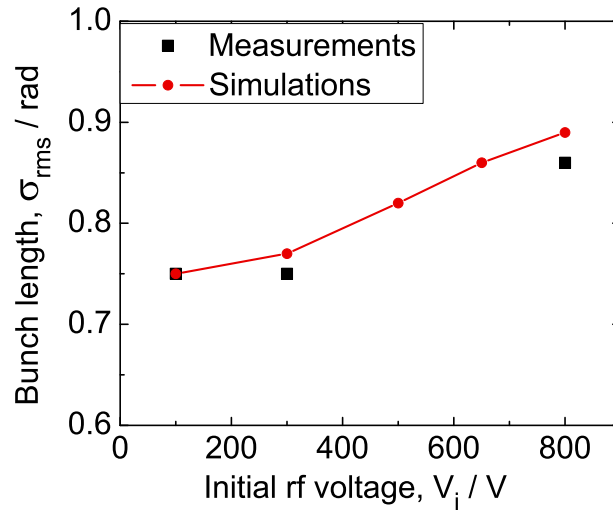


Figure 6.16: From the Table 6.2, the measured variations in the bunch lengths with V_i are plotted. They are compared with the corresponding values from the simulations.

minor deviations between the measurements and the simulations for the higher amplitudes

of V_i .

The scaling parameter χ , for the initial voltage V_i of 800 V (Table 6.2) is below its threshold value χ_{th} and distortion in the bunch form (Fig. 6.17) are supporting the outcomes explained earlier in Subsec. 6.1.2. On the other hand, a perfect bunch is observed

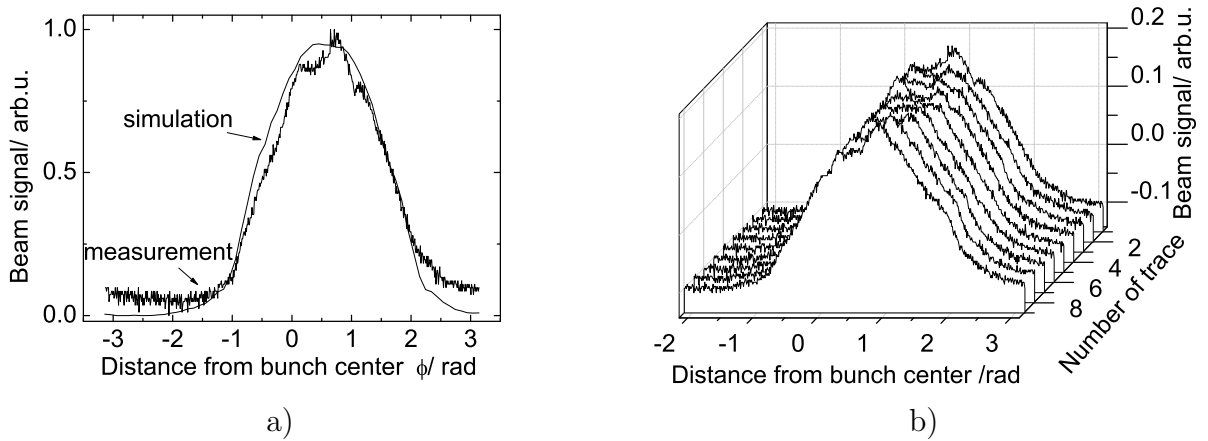


Figure 6.17: a) Bunch form for the ramping time of 20 ms with a V_i of 800 V. b) Waterfall curve for iso adiabatic ramp with ramping time of 20 ms and a V_i of 800 V.

for the lower V_i of 100 V (Fig. 6.12 b). Furthermore, the oscillations at the top of the bunch are observed for higher V_i (Fig. 6.17 b) against the one with the lower V_i (Fig. 6.13).

The above result shows that *for the given parameters (Table 6.1) and for the $t_{ramp} \geq 20$ ms, there will always be an adiabatic capture of the beam irrespective of the type of ramp. The matching of the rf frequency with the corresponding beam energy and the careful choice of initial voltage (scaling parameter χ) can be regarded as important prerequisites to propose the case for the adiabatic capture of the beam.*

6.3.2 Double rf system

For the measurements with double rf system some key inputs are referred from the single rf measurements. For example, the Dilution Factor and the bunch form distortions for $t_{ramp} \leq 10$ ms are observed in srf measurements (Fig. 6.10 and 6.12). Hence, drf mea-

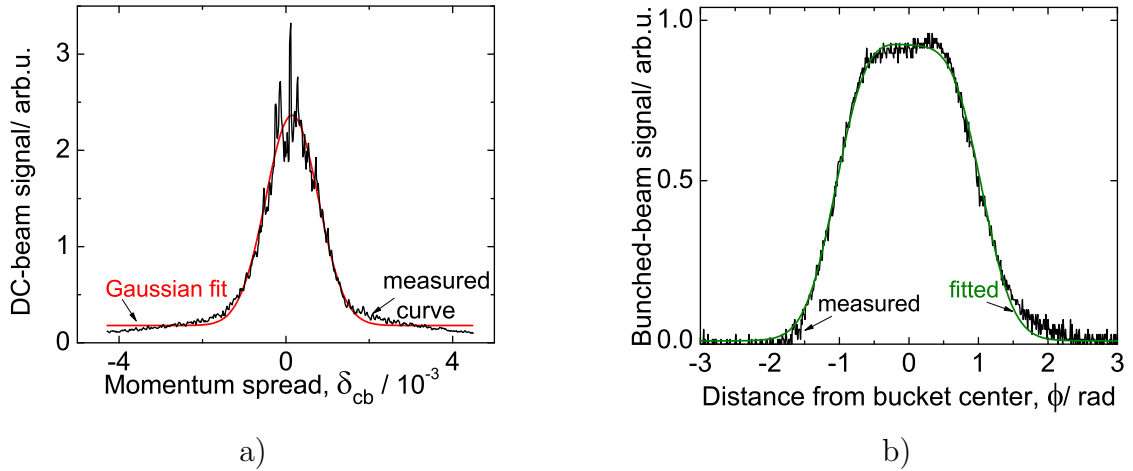


Figure 6.18: a) An example showing Gaussian fitting of the Schottky signal from the coasting beam and here the momentum spread of 6.4×10^{-4} . b) A bunched beam signal from the longitudinal pick-up is fitted to a corresponding distribution.

surements are started from the t_{ramp} of 10 ms. For this range of t_{ramp} all types of ramps exhibit similar performance (Fig. 6.10). Therefore, only one type of ramp, i.e. iso-adiabatic (Eq. 6.3) is tested here. An example of the ramp used in the measurement is shown in Fig. 6.8 and the measurement settings are shown in Table 6.1.

The coasting beam area is derived from the Schottky signal (Fig. 6.18 a) in the similar way as for the srf system. For bunched beam emittance as well, the method used for the srf is applicable, except that no Gaussian fit is possible for the BPM signal (Fig. 6.18 b). Therefore, the definition of rms emittance is applied to both the beams for calculating the DF. *Additionally, a flat bunch can clearly be observed, which strongly supports the goal of using the drf system in upgraded SIS for FAIR (Sec. 2.11).*

The variations in the bunch length, ϕ_m with the ramping time t_{ramp} are observed (Fig. 6.19) at the constant initial and final voltages (Table 6.1). A nearly constant ϕ_m is observed (Fig. 6.19) in measurements as well as in simulations, for all $t_{ramp} \geq 20$ ms. The comparison of ϕ_m , instead of DF, is due to the same reason as explained earlier for single rf (Subsec. 6.3.1). The simulations are performed with and without inclusion of the longitudinal intensity effects (Secs. 4.1 and 4.2), but no difference in the ϕ_m is observed. The bunch forms for t_{ramp} of 20 ms and 100 ms can be observed in Fig. 6.20. It shows that, any further increase in t_{ramp} above 20 ms brings no qualitative improvements in the bunch

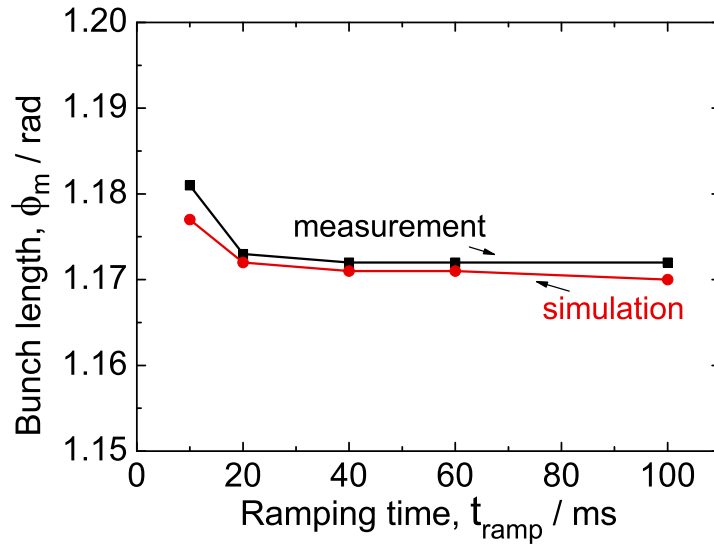


Figure 6.19: Measurements and simulations showing variations in the bunch length, ϕ_m with the t_{ramp} .

form. The Double rf bucket (Fig. 3.7) is aimed to create the larger and flat bunches in SIS,

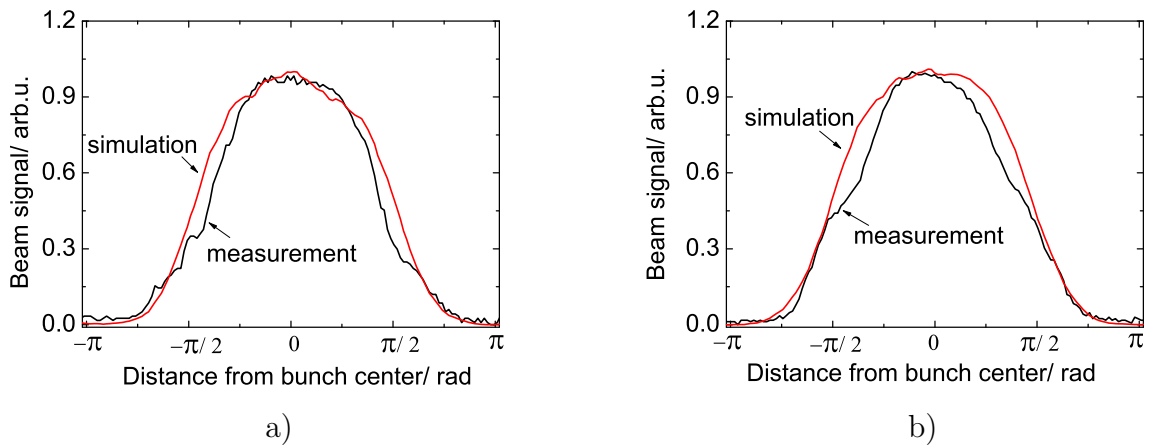


Figure 6.20: Bunch forms from measurement and simulation, for a ramping time of a) 20 ms and b) 100 ms.

and can be clearly observed. The measurements and simulations are in good agreement (Fig. 6.20) irrespective of the t_{ramp} . No trace of the influence of the beam intensity on the bunch form (Subsec. 4.5.2) is observed in this case (Table 6.1), which represents nearly the highest possible range of the beam intensity for Ta⁶¹⁺ ion-beam in the present SIS.

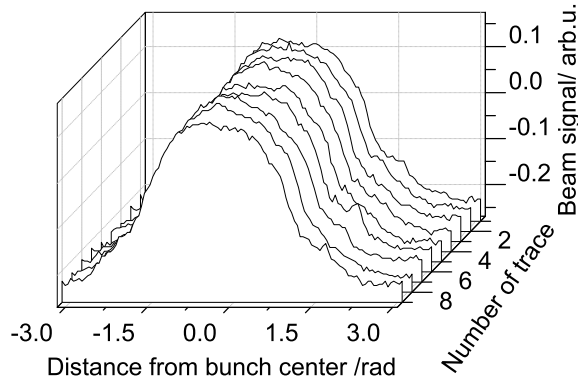


Figure 6.21: Waterfall curves showing a steady bunch evolution with time for 20 ms for the iso-adiabatic ramp for both cavities with other parameters are from the Table 6.1.

The waterfall for the t_{ramp} of 20 ms in Fig. 6.21 shows that the bunched beam with these optimized ramp parameters is quite stable.

Hence, *with the given measurement parameters (Table 6.1), an iso-adiabatic ramp with drf system will always be resulting in an adiabatic capture. And in the stable bunch with all $t_{ramp} \geq 20$ ms, no difference in the ϕ_m is observed due to the effects. It is also observed that the beam intensity exhibits no influence on the ϕ_m .*

6.3.3 Upgraded SIS

On the basis of the agreement of the simulation for the present SIS parameters (Table 6.1), the optimized ramp parameters are tested for the upgraded SIS (Table 2.4) with drf system

Beam and machine parameters	
Ion species	Ar ¹⁸⁺
Total Energy, E/ GeV	37.7
δ_{cb}	$5 \cdot 10^{-4}$
Q-factor (for h=2 /4 cavity)	0.5/ 20
f_r (for h=2 /4 cavity)/ MHz	0.43/ 0.86
V_0 (for h=2 cavity)/ kV	8

Table 6.3: The beam, machine and cavity parameters for simulating the beam capturing in upgraded SIS.

(Subsec. 3.3.3). For the drf system formed by the MA ($h=2$) and the ferrite ($h=4$) cavities, the iso-adiabatic ramp in Fig. 6.8 is feeded, with harmonic numbers of 2 and 4 instead of 4 and 8. Simulations with the consideration of the intensity effects (Sec. 4.1 and 4.2) are performed with the beam parameters mentioned in Table 6.3. The cavity and space charge impedances are taken from the Table 4.1. The details about the inclusion of the effects are mentioned in Sec. 4.6.

Figure 6.22 is illustrating the variations in the bunch length, ϕ_m with t_{ramp} . A significant change in the ϕ_m is observed for $t_{ramp} \leq 10$ ms irrespective of the beam intensity. It indicates that for this region the influence of the capturing parameters is prominent. But beyond this range a higher ϕ_m is observed due to the influence of the intensity effects. Additionally, irrespective of the beam intensity the ϕ_m is stabilized and becomes nearly constant for all $t_{ramp} \geq 20$ ms, which is the case in the present SIS (Fig. 6.19). The

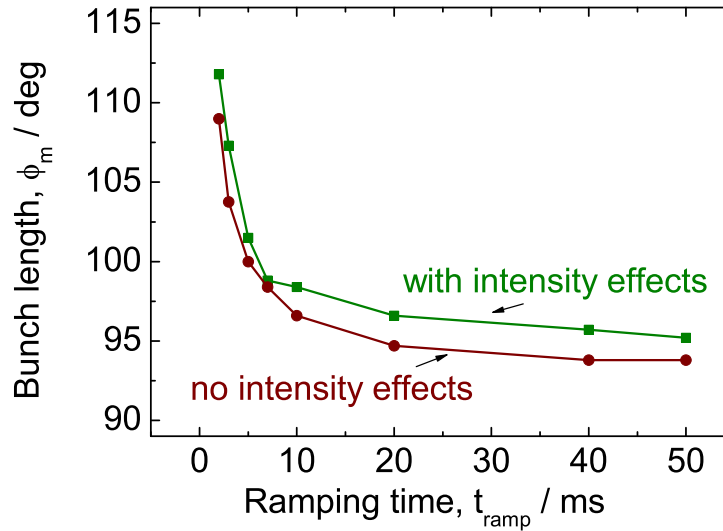


Figure 6.22: The simulated bunch length ϕ_m , is reducing with the increase in t_{ramp} . The beam is, with the parameters mentioned in Table 6.3, captured by a double rf system in upgraded SIS (Table 2.4). The cavity and space charge impedances are taken from the Table 4.1.

corresponding bunch form is shown in the following chapter, which is devoted for the beam loading study in SIS.

The key conclusions drawn from this capture study are,

- The optimized ramp parameters, particularly the t_{ramp} of 20 ms, are valid for the upgraded SIS as well.
- An influence of the beam intensity on the capturing process is visible in the upgraded SIS while the influence was insignificant for the present SIS.

Chapter 7

Beam Loading Measurements

This chapter is devoted for the measurement of the beam loading effect on a stationary bunch at injection energy in SIS. This bunch is formed from the coasting beam, by using the optimized rf amplitude ramps for the adiabatic capture (Chap. 6). The stability of the coasting beam in presence of the estimated longitudinal impedance is assured (Sec. 4.4) with the impedance taken from test cavity measurements (App. B). As it has been observed, the potential well distortion due to the beam loading effect estimated from the theory and simulations have their own limitations (Chap.4), the measurement of the effect is needed. The method used for the measurements offers an advantage that the shunt impedance of the cavity could also be extracted.

Further, the $h=2$ cavity (Table 2.5) is not yet installed in SIS and bunch compressor cavity (Table 2.3) is the only MA cavity available at present. Therefore, to study the influence of a MA cavity on the bunch, the bunch compressor cavity is used. The detailed principle and measurement method are explained in this chapter.

The chapter begins with the explanation of the measurement principle. Then the longitudinal beam diagnostic adapted for these measurements will be presented. Thereafter, sequentially, these measurements for the single and double rf systems will be presented in two separate sections. Each section will explain the machine settings and compare the results from the measurements, with simulations and, in some cases, also with theory.

7.1 Principle of measurement

Beam loading measurements in SIS ring (Fig. 2.2) with two ferrite and one compressor cavity (Sec. 2.3) is broadly divided in two parts of single and double rf operations. This division makes sense because the beam loading effect (Subsec. 4.1) depends upon the bunch form, which further depends upon the type of rf operation, and the type and amplitude of the impedance offered by the rf cavity.

For single rf operation, the beam is driven by either or both of the ferrite cavities. The magnetic and electric properties of the ferrite material and hence the shunt impedance R_s (Eq. 2.2) of the cavity depends upon the magnitude of the rf field [33, 31], which in turn

depends upon the amplitude of the gap-voltage, V_0 . As the beam loading effect directly depends upon R_s , its measurement for the ferrite cavity is divided in two parts.

- In first case the cavity is driven only by the beam and there is no external rf field across its gap. Such cavity is referred here as an ‘open cavity’. In this case the parallel equivalent circuit in Fig. 4.1 is reduced to the circuit shown in Fig. 7.1 a). If this cavity is tuned to the resonance (Fig. 2.8), then the R_s represents the maximum possible impedance offered by the ferrite cavity. It represents the extreme case of beam loading effect because the amplitude of the beam loading voltage V_b induced by the given beam current (Eq. 4.1) is maximum for these settings. With one open

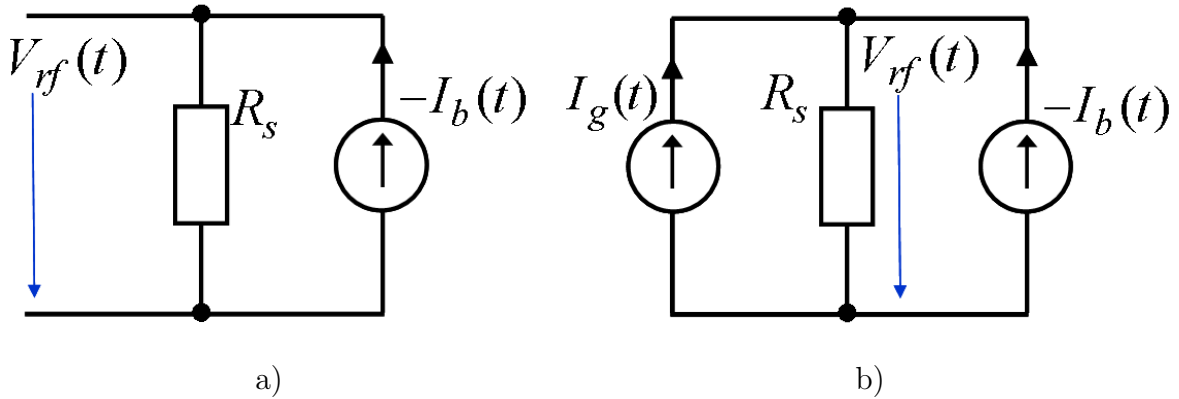


Figure 7.1: a) The settings for the open cavity which is externally tuned to the resonance. Here beam is driving the cavity and inducing the voltage across its shunt impedance. b) The settings for the driving cavity, which is tuned to the resonance by the RFCL. It is driven by the generator and the beam currents.

cavity in the ring, the beam is bunched by the other ferrite cavity referred here as the ‘driving cavity’.

- In second case the driving cavity (Fig. 7.1 b) is driven by both beam and the external rf power. This cavity is equipped with the amplitude and resonance frequency control loops (Subsec. 2.3.3). As this is the practical operating condition for the cavity, it represents the realistic case of the beam loading. For the same reason i.e. R_s being a function of V_0 , the aim was to measure the beam loading effect corresponding to the whole working range of V_0 .

For a certain machine and beam parameters (Table 4.1) along with the known value of R_s [37], the range of V_b (Eq. 4.18) is estimated. For the extreme cases of the beam intensity, this V_b was found too low (≤ 100 V) in comparison to the V_0 (Eq. 4.1). Therefore, it was not possible to measure this range of V_b in presence of the cavity control loops.

Another possibility to observe this effect was explored, when the control loops were

kept bypassed. An off-line (in absence of beam) experiment was performed to check the level of electronic noise in the cavity. This level was found in the range of estimated beam loading, which meant that bypassing of the control loops will introduce the noise in the gap-voltage in the range of V_b .

In this situation, the responses of the control loops are compared for the two different conditions of with and without beam in the SIS ring. As it is evident that the beam loading effect is present only in the machine with beam, a difference in the control loop responses is the measure of the beam loading effect. The controller output for the amplitude control loop (Fig. 2.9) and the bias current output in the resonance frequency control loop (Fig. 2.10) are the key outputs measured for this purpose.

A double rf operation (Subsec. 3.3.3) in the upgraded SIS is planned, where a high intensity beam will be driven by the Magnetic Alloy (h=2) and the ferrite (h=4) cavities. The principle of measurement of the beam loading effect for the ferrite cavity is mentioned above and the measurement for the planned h=2 cavity (Table 2.5) is not possible as of now, since the cavity is not yet installed in the ring. At present, the bunch compressor cavity (Table 2.3) is the only available MA cavity in SIS. And *it can be viewed as a broad-band cavity in relation to the open ferrite cavity*. The beam loading effect with this cavity is measured with the aim of estimating the influence of a broad-band cavity on the beam. The beam was bunched by the ferrite cavities and the bunch compressor cavity is kept opened so that it is driven only by the beam (Fig. 7.1 a).

To observe the influence of the beam-cavity interaction on the beam as well as on the cavities, the beam current, beam intensity, bunch form and the amplitude and phase of the cavity voltages are the important parameters to be measured. Along with these parameters, the momentum spread of the coasting beam before the beginning of the capture (Fig. 2.4) is needed as an input for the simulations. The method of measurements and the beam diagnostics adopted for it is explained in the following section.

7.2 Measurement method and instruments

The measurement scheme (Fig. 7.2) shows the arrangement of the different diagnostics and the instrumentation used for measuring the beam loading effect in SIS. The coasting and bunched beam measurements are similar to those in capturing measurements (Subsec. 6.2.1).

- The longitudinal beam signal is collected using the beam pick-up and through the intermediate electronics this signal is observed using an oscilloscope (Sec. 5.2).
- For the momentum spread δ_{cb} of the coasting beam before capture, the longitudinal Schottky signal from the beam is collected by the Schottky pick-up. Through the intermediate electronics it is observed by using a spectrum analyzer (Sec. 5.3).
- An external Digital Signal Processor (DSP) system (Fig. 7.2) is used to measure the phase difference between the two gap-voltages in the srf system and to synchronize

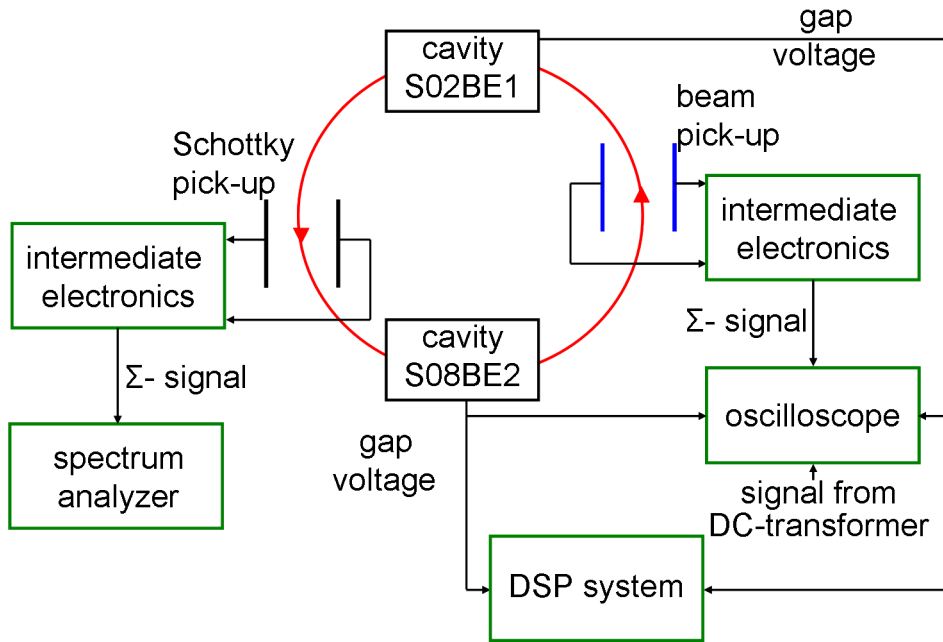


Figure 7.2: A schematic diagram showing how the quantities mentioned in Sec. 7.1 are collected and observed for the measurement of the beam loading effect in the SIS ring. The details about the diagnostics and instrumentation used for the measurements are explained in chapter 5.

the cavities in drf system (Sec. 5.4).

- Along with the well-known fast trafo (Fig. 5.2), a continuous recording (with an oscilloscope) of a voltage signal through the dc transformer is done (Fig. 7.3). The beam intensity from this voltage is derived as explained in Sec. 5.1.

The driving cavities are fed by the self-designed rf amplitude ramps for both the rf systems.

- The gap-signals from the cavities are collected using different amplifiers, where the higher amplification is reserved for the expected weak signal from the open cavity. These signals, along with the beam signal and the signal from the dc transformer are observed using an oscilloscope (Fig. 7.3).
- One of the oscilloscopes is used to observe and record the gap signals, beam signal from longitudinal pickup and beam intensity signal from a dc transformer. Second oscilloscope is used to record control loop outputs (Fig. 2.9, 2.10). The gap-voltages can be measured across any, left or right, half -gap of the cavity and the virtual ground (Fig. 3.1). A trigger unit [80](Fig. 7.3), comprising a counter, is synchronized with the circulating bunches and to the reference DDS [98, 97].

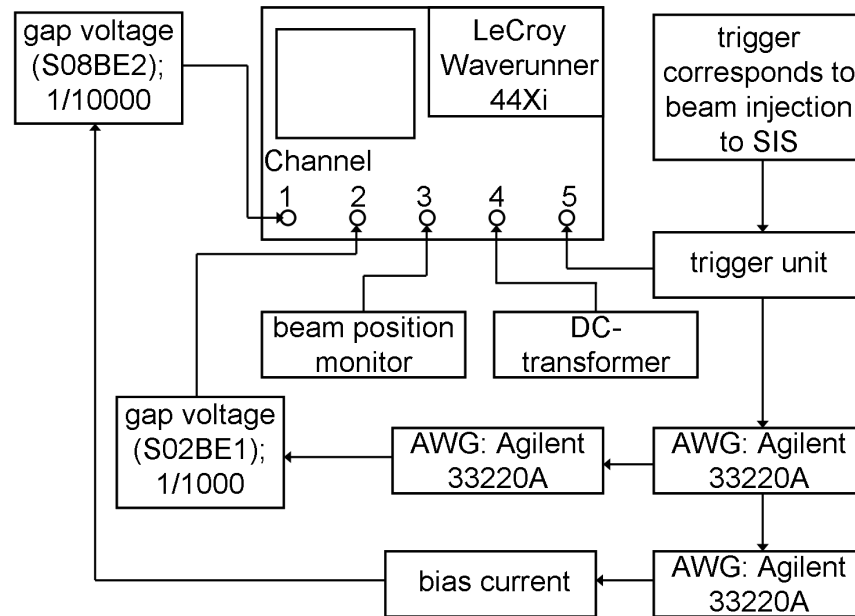


Figure 7.3: A block diagram showing the signals recorded by an oscilloscope. The oscilloscope is triggered to the event set by triggering unit. Depending upon the strength of the gap signal there is a possibility to choose the different amplifiers for tapping them.

- The trigger unit receives a trigger through the DDS and the instant corresponds to the beam injection in SIS. Then its counter is set the steps/delay between two measurements. For example, every 10th turn in SIS corresponding to the 40 rf periods (for $h=4$) is delivered from the DDS reference signal to the trigger unit. The output of this device triggers the oscilloscopes and all Arbitrary Waveform Generators (AWG). This scheme ensures the synchronism among all the measuring instruments.
- Two Agilent AWG have been used (Fig. 7.3) with the purpose of producing different rf amplitude ramps (Fig. 7.4) and to vary the DC bias (Fig. 2.6) current. And the third AWG is used to synchronize the above two to the trigger event. The required bias current was chosen by referring the results from the test cavity experiments (Fig. B.2). The ramps prepared in the form of Excel-sheets are loaded to the AWG remotely as mentioned in Chap. 6.
- For the drf system two Arbitrary waveform generators are used for feeding the rf ramp (Fig. 7.4) to the driving cavities and the third one is to synchronize the above two to the trigger event. No bias control is needed in this case of open compressor cavity.
- Along with the description of the each diagnostic device the post processing of the data is also explained in chapter 5.

7.3 Settings of the parameters

Table 7.1 displays the machine and beam parameters used for the measurements performed with different beam intensities and ion species. All the experiments are performed at the

Parameter	Single rf settings	Double rf settings
Ion species	Ur ⁷³⁺ , Ta ⁶¹⁺ , Ar ¹⁸⁺	Ta ⁶¹⁺
Energy/ MeV/u	11.2, 11.149, 11.38	11.149
Beam intensity/ ppc	$\approx 4 \times 10^8$, 4×10^9 , 2×10^{10}	$\approx 4 \times 10^9$
Harmonic number, h	4	4, 8
Rf frequency/ f_{rf} / kHz	849.5, 848.57, 857.2	848.57, 1697.15
Initial voltage/ V_i / V	100	100
Final voltage/ V_f / kV	2 to 12	8, 4
Ramping time/ t_{ramp} / ms	20	20

Table 7.1: Machine, beam and rf parameters settings for the measurements with both rf systems. An approximate number is mentioned for the beam intensity because of the fluctuations in it. The non-zero V_i (Subsec. 6.2.2) and the V_f at fundamental frequency are varied from 4 to 12 kV. The f_{rf} is extracted from the gap signal of the driving cavity.

injection energy to SIS. As f_0 cannot be adjusted, the rf frequency, $f_{rf}(=h f_0)$ is adjusted manually to the value corresponding to this energy (Fig. 6.15) to avoid the mismatch.

In the driving cavity, the different outputs of the control loops are tapped and compared for both the cases of with and without beam as mentioned in Sec. 7.1. Here, apart from the main machine with the required machine settings (Table 7.1), a virtual machine was set. This virtual machine had exactly similar rf and lattice settings [73] as for the main machine, but without the beam. During experiment, the data was collected by alternately switching over between both the machines.

The R_s is the impedance of the cavity along with the tetrode tube (Fig. 2.6) observed by the beam. Hence a DC working point of the tube, which decides its impedance, is important. There were following similar settings for the working point of tetrode tube (class-B operation) [37] for both the ferrite cavities

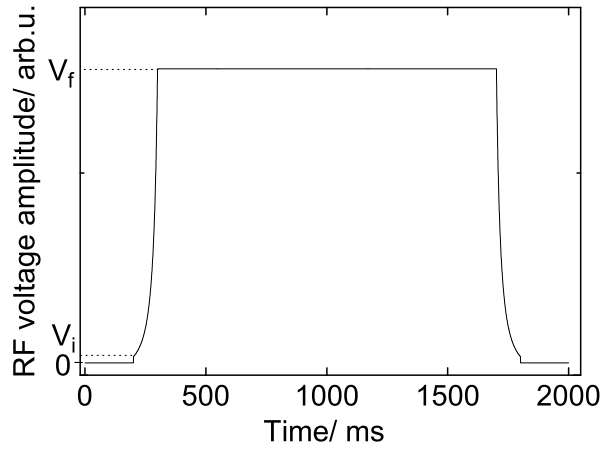


Figure 7.4: Illustrates the rf amplitude ramp used for the driving cavity ($h=4$) for single rf operation. For the double rf case the V_f is doubled for $h=2$ cavity and is halved for the $h=8$.

- Anode current, $I_a=4.5$ A and anode voltage, $V_a=13$ kV
- Screen-grid voltage, $V_g=1.8$ kV and control-grid voltage, $V_{gc}=-200$ V.

The rf amplitude ramps used for the driving cavity to form the stationary bucket (Subsec. 3.2.2) are aimed for the adiabatic capture (Chap. 6). An example of such an rf cycle for **the srf system** is shown in Fig. 7.4, where a long flat-top of 1400 ms is chosen. The level of this flat top shows the amplitude of V_0 which was varied during the measurements (Table 7.1). During this period, the bias current in open cavity is varied. A time delay of ≈ 100 ms is set to collect the Schottky signal (Fig. 7.2) from the coasting beam.

For **the drf system** in the present SIS, one cavity operates at $h=4$ and the other one at $h=8$, with parameters $\alpha=0.5$ and $n=2$ (Subsec. 3.3.3). The beam in this system experiences a constant impedance introduced by the opened compressor cavity. Settings for these open and the driving cavities are similar to that for the srf measurements (Fig. 7.1 a, b), except that no tuning arrangement is required for the bunch compressor cavity. For the adiabatic capture, both of the driving cavities are feeded with the separate rf amplitude ramps at their corresponding frequencies (Fig.6.8).

At different points, the measurement results are compared with the corresponding ESME simulations (Sec. 4.6). The separate files are used for inserting the cavity parameters for simulating the beam interaction in different rf systems. Along with the beam loading, the space charge effect is also included in the simulations unless it is stated otherwise. Any further addition or assumptions for observing a particular property or behavior is mentioned specifically in the respective section. The coasting beam, with a certain momentum spread, is captured adiabatically using the same ramp which is used in the measurements (Fig. 7.4).

7.4 Observations and results

For the parameters mentioned in Table 7.1, the corresponding variations in the beam loading voltage and its influence on the cavity and beam have been observed.

The beam loading parameter α_{bl} (Sec. 4.5) is defined for the uniformly distributed impedance in the ring and is not applicable for the ferrite cavity. It is used here only to define the level of beam intensity and is calculated numerically by using the R_s of the cavity in its mathematical definition (Eq. 4.25). Initially, the direct observations about the beam and gap-voltages are presented. It is followed by the results derived by processing the data. These results are presented along with the corresponding ESME simulations. Based upon the agreement of measurements with the simulation, the simulations are extended for the upgraded SIS.

7.4.1 For single rf system

The settings for both the ferrite cavities are shown in Fig. 7.1. Their gap-voltages V_b and V_{rf} respectively, along with the BPM signal, observed in the oscilloscope are shown in Fig. 7.5. The amplitude of the signals is normalized to the peak value of the respective quantity. The phase difference between these signals is found in good agreement with the

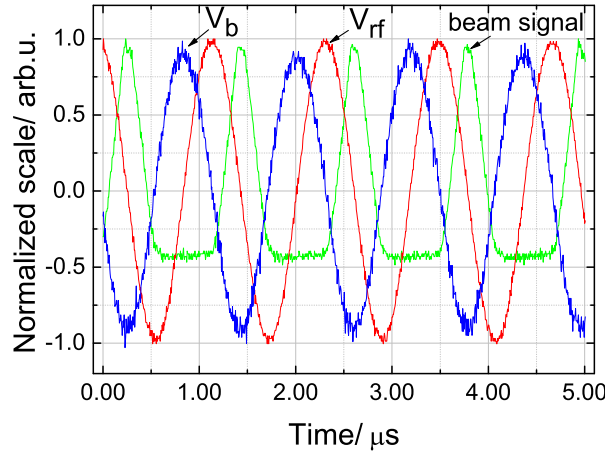


Figure 7.5: The waveforms showing the phase relations among beam current, beam loading and rf voltages for the measurements with the ion U^{73+} for the corresponding beam parameters mentioned in Table 7.1.

theory (Fig. 4.2). The beam signal shows all the four bunches formed by the rf signal with T_{rf} of $1.18 \mu s$.

This beam signal with a constant intensity is observed for various values of V_0 (Fig. 7.6 a). As expected, with the increase in V_0 the bunch length ϕ_m is reducing and consequently

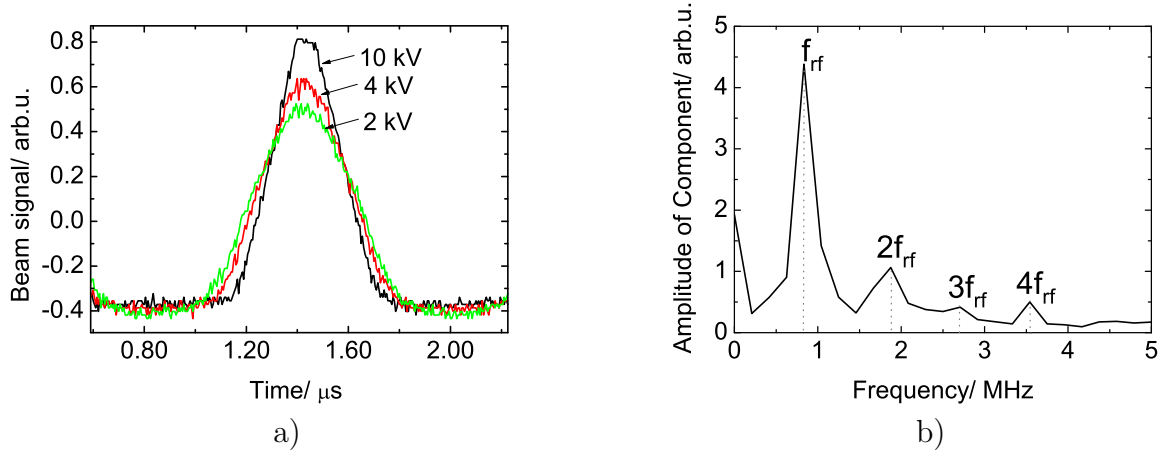


Figure 7.6: a) The bunch forms for different V_0 for the measurements with $U_{r^{73+}}$ beam (Table 7.1). b) The Fourier transform of the bunch with V_0 of 10 kV in Fig. 7.4.1 a, indicating the frequency components at first four harmonics of rf frequency f_{rf} . The most of the beam power goes with the component at fundamental rf frequency.

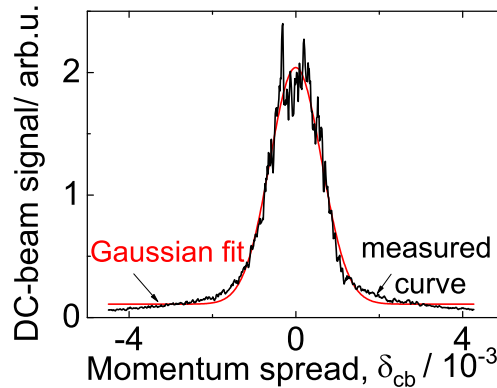


Figure 7.7: The fitting of a processed Schottky signal collected from the coasting beam.

the rf component of the beam current I_{rf} is increasing (Eq. 4.13). The bunches observed with the ϕ_m in the range of 0.4 to 0.55 μs against T_{rf} of 1.18 μs indicates the existence of long bunches ($\phi_m \approx T_{rf}$) in SIS.

Further, the Fourier transform of the bunch with V_0 of 10 kV (Fig. 7.6 a) shows that the bunch power is existing at the fundamental rf frequency $f_{rf}(=4f_0)$ and its 3 consecutive higher harmonics (Fig. 7.6 b). This spectra is dominated by the frequency component at f_{rf} i.e. 849.5 kHz. For the cavity tuned to this frequency and with $Q \approx 30$ (Fig. B.2) its rise time (Eq. 2.7) T_r is $\approx 11 \mu\text{s}$. This T_r being $\approx 10 \cdot T_{rf}$, it approves the consideration of the **steady-state beam loading** (Eq. 4.4) for the SIS ring.

The Schottky signal from the coasting beam is shown in Fig. 7.7. After processing, the averaged Schottky signal is fitted to a certain form of distribution to derive the momentum spread δ_{cb} (Sec. 5.3). In present case, it is fitted to a Gaussian distribution and gives the δ_{cb} of $6.4 \cdot 10^{-4}$. The noisy Schottky signal [75] is being interpreted as a source of the imprecise value of δ_{cb} . In addition, there were the variations in δ_{cb} with the ion species and the beam intensity [63]. These variations may introduce some degree of discrepancy in the measurements with the respective simulations, where the constant δ_{cb} is considered.

The bias current is swept from 10 to 13 A (Fig. B.2) to tune the cavity to resonance (Fig. 7.3). Thus, the open cavity is matched to the rf frequency (Subsec. 4.1.1) corresponding to the beam energy (Table 7.1). This tuning is performed during the flat-top of the rf

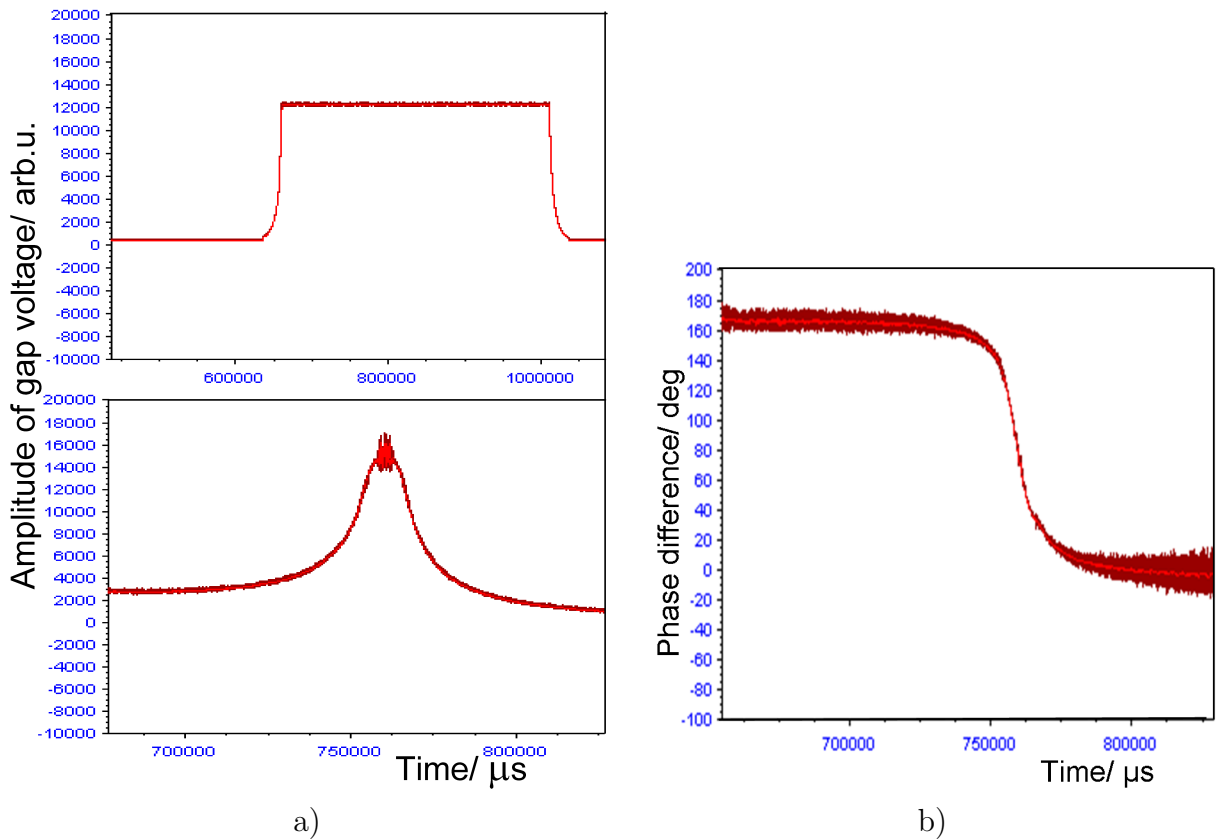


Figure 7.8: The screen shots from the DSP system shows a) The V_0 for the driving cavity (above), the amplitude of the V_b in the open cavity (below). The peak value of V_b (102 V) is achieved during the flat top of the V_0 (12 kV), where the cavity is tuned to resonance. b) The phase difference of 90° between V_{rf} and V_b is corresponding to the peak amplitude in the tuned cavity (Fig. 7.8 a(below)).

wave (Fig. 7.4). The gap-voltages across both the cavities are shown in Fig. 7.8 a. The peak amplitude of V_b is observed during the constant V_0 in the driving cavity. It approves the external tuning of the open cavity to resonance.

The phase difference between the gap-voltages is shown in Fig. 7.8 b. The instant corresponding to the phase of 90° matches exactly to the instant of peak amplitude of V_b (Fig. 7.8 a). Once the cavity settings were assured by these ‘online observations’ further measurements and the data recording (Sec. 7.2) were proceeded.

Observations across open cavity

The V_b induced in the open cavity (Fig. 7.1 a) by a stationary bunch (Fig. 7.6 a) depends upon the I_{rf} at different frequencies and their corresponding R_s (Eq. 4.18). During the measurement, it was observed that in the ferrite cavity most of the beam power is absorbed at f_{rf} (Fig. 7.6 b). Therefore, it is appropriate to consider the beam current only at this frequency. The I_{rf} varies with the beam intensity and the Γ factor (Eq. 4.16), which in turn depends upon the V_0 .

V_0 / kV	V_b / V	I_{dc} / mA	σ / deg	Γ	I_{rf} / mA	R_s / k Ω
3	50	11.8	75	0.86	10	5
4	53	11.8	67	1.03	12.1	4.4
5	55	11.8	65	1.07	12.6	4.4
6	57	10.7	63	1.11	12	4.8
10	70	9.2	57	1.24	12.4	5.6
12	102	12.86	55	1.28	16.4	6.3

Table 7.2: Results for the open cavity measurements. The rf voltage (V_0) is the voltage across driving cavity; V_b is measured across the open cavity; DC current, I_{dc} is indicating the beam intensity variations; rf current, I_{rf} (Eq. 4.16) is the current at the fundamental rf frequency, f_{rf} , for the cavity; the rms bunch length, σ_{rms} (Sec. 3.3) depends on the V_0 ; the shunt impedance R_s for the tuned cavity (in Fig. 7.1 a) is calculated here, by using the voltage across and the current through this tuned cavity.

As the beam intensity is not constant (Table 7.2), it is difficult to differentiate the influence of beam intensity and V_0 .

With the constant cavity and beam settings (Sec. 7.3), an increase in the amplitude of V_b with V_0 is observed (Fig. 7.9). Its proportional increase with V_0 is prevented by the fluctuations in the beam intensity. This relation (Fig. 7.9) is in good agreement with the

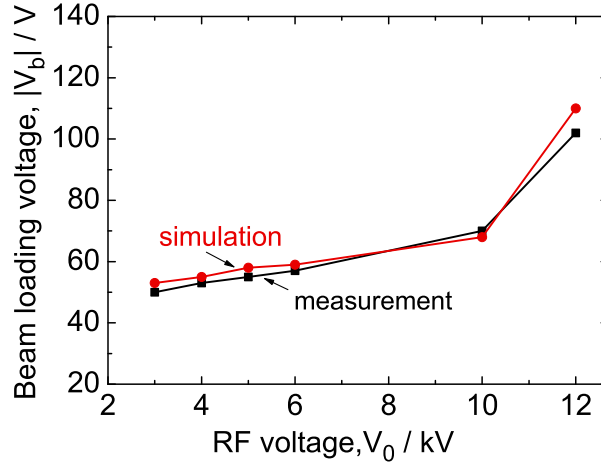


Figure 7.9: The measurements and simulations showing the variations in V_b with V_0 , for Ar^{18+} (Table 7.1), with $\alpha_{bl} = 0.17$ and $\alpha_{sc} = 0.1$.

Type of cavity	Q_0	f_r / MHz	R_s / $k\Omega$
Open	40	0.86	5
Driving	10	0.86	0.001

Table 7.3: The simulation settings of the technical parameters for the cavities in srf operation in present SIS.

simulations performed with the similar settings. The beam loading effect is added by using the cavity parameters in Table 7.3. Among these parameters,

- the resonance frequency $f_r = f_{rf}$ for both the cavities
- the R_s for the open cavity is taken from Table 7.2 and for the driving cavity it is 1Ω (as the V_b is too low as compared to V_0 in driving cavity with control loops)
- the Q-factor for the open and driving cavity are taken from the test cavity measurements (Fig. B.2).

To cope up with the variations in the δ_{cb} , the final bunch length is compared with the bunch length from the measurements. The dependence of the bunch length on V_0 (Eqs. 3.12 and 3.16) is shown in Fig. 7.6. Several known and unknown impedances in beam surrounding are responsible for inducing the voltages against external rf voltage and hence the rms bunch length, σ_{rms} (Eq. 4.23), is bit higher in measurements than in the simulations. Also a coasting beam with constant δ_{cb} is captured in simulation, which is not always the case in reality [63]. Similar to the low intensity Ur^{73+} beam (Fig. 7.6 a) the σ_{rms} is varying with V_0 in the range of 55° to 75° . This Ar^{18+} beam is with the highest range of beam intensity in

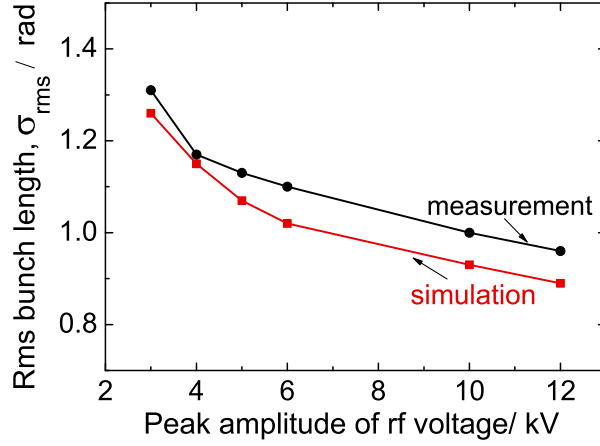


Figure 7.10: The variations in σ_{rms} with V_0 , for Ar^{18+} (Table 7.1), in the measurements and simulations.

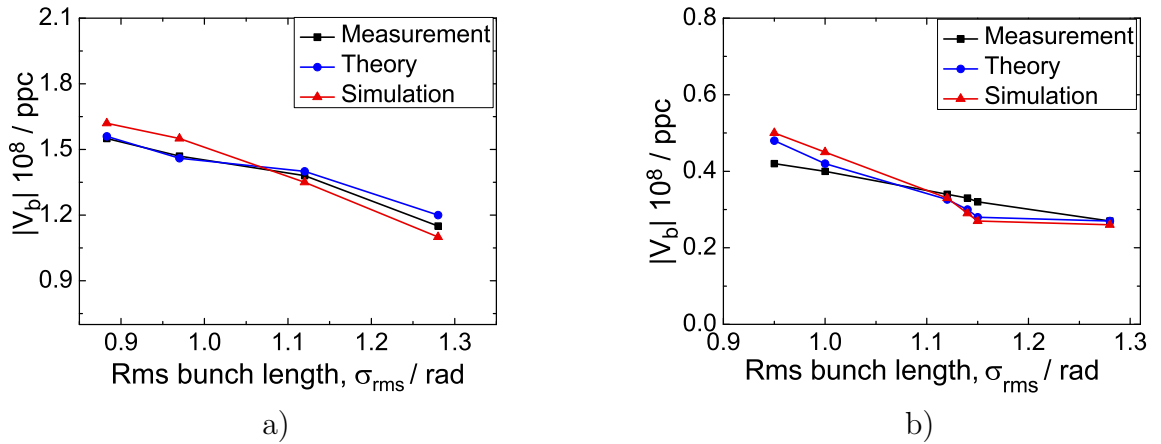


Figure 7.11: Observations for a) Ta^{61+} with $\alpha_{bl} = 0.09$ and $\alpha_{sc} = 0.05$ b) Ar^{18+} with $\alpha_{bl} = 0.17$ and $\alpha_{sc} = 0.1$.

present SIS and supports the assumptions of the long bunches and the steady-state beam loading (Eq. 4.4) for this higher range of beam intensity as well.

The relation in Fig. 7.10 is used to summarize the amplitude of V_b corresponds to V_0 . To avoid the influence of fluctuations in beam intensity (in Table 7.2), the amplitude of V_b is averaged to the corresponding intensity and then it is compared for the different bunch lengths (Fig. 7.11). The theoretical value of V_b /ppc is calculated (Eq. 4.15) for σ_{rms} , R_s and the I_{dc} from the measurements (Table 7.2). The calculations are sensitive to these

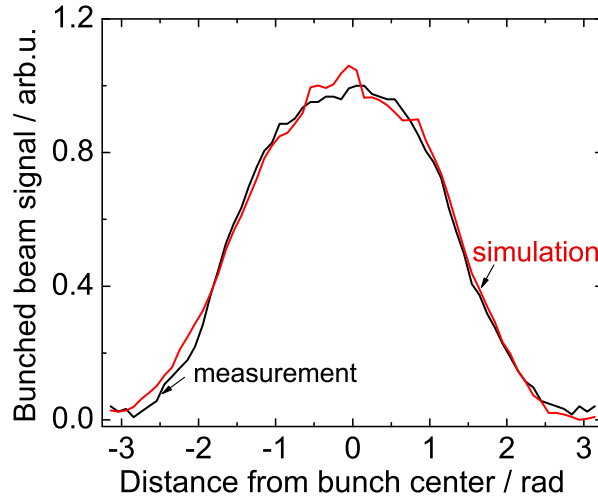


Figure 7.12: The bunch forms from the simulation and measurement for Ar^{18+} beam with the parameters in Table 7.1.

parameters and are the source of the minor deviations from their corresponding values in the simulation and measurement.

The factor V_b/ppc is used to compare the amplitude of V_b for the different range of beam intensity (Fig. 7.11 a and b). For an intensity range with $\alpha_{bl} = 0.09$ and $\alpha_{sc} = 0.05$ (in Fig. 7.11 a) the percentage variation in V_b/ppc is 35%. But, with $\alpha_{bl} = 0.17$ and $\alpha_{sc} = 0.07$ (in Fig. 7.11 b) the variation is 50%. A significant difference in the response within this short intensity range (Table 7.1) can be observed. *The bunch forms in Fig. 7.12 indicate that the beam loading and space charge effects for the present SIS parameters are successfully simulated in ESME. Hence, it approves the extension of this study for the upgraded SIS with higher beam intensity.*

Keeping all the parameters like amplitude of rf voltage, harmonic number and bunch length constant (Table 7.1), the relation in the Fig. 7.11 is extrapolated for the SIS with upgraded beam intensity for Ar^{18+} (Fig. 7.13). In this case, the intensity parameters α_{bl} and α_{sc} are 1.73 and 0.98 respectively.

As shown in Fig. 7.14 the beam observes a variable amplitude of the shunt impedance R_s . The variations in the gap voltage V_b (Table 7.2) are not significant enough to influence the properties of the ferrite material [33, 31]. Therefore, V_b can not be the source of the variations in R_s .

The resonance frequency of the cavity, which is not constant, also influences the R_s (Eq. 2.5). The RFCL is not active in this cavity and the bias current is adjusted externally to tune this cavity to the frequency of the beam signal. Therefore, the frequency variations in the beam directly reflect in it. As the cavity, in turn, is quite sensitive to the fluctuations in frequency (Fig. B.2), they are understood as the source responsible for the variations in

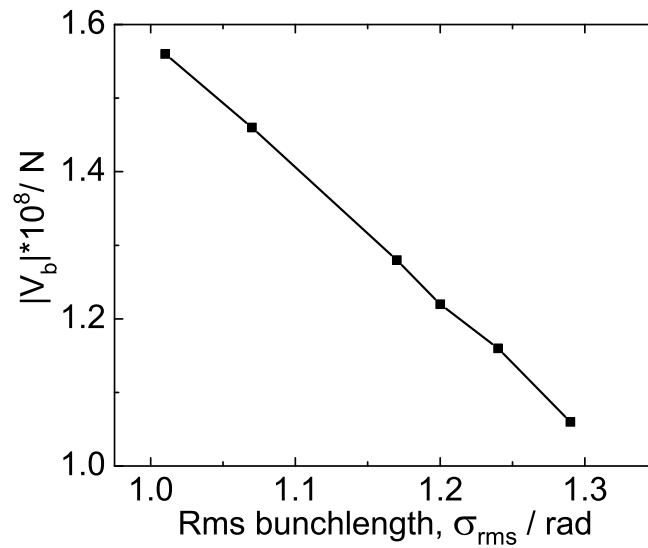


Figure 7.13: Amplitude of the beam loading voltage with SIS upgrade parameters (Table 2.4) with $\alpha_{bl} = 1.73$ and $\alpha_{sc} = 0.98$.

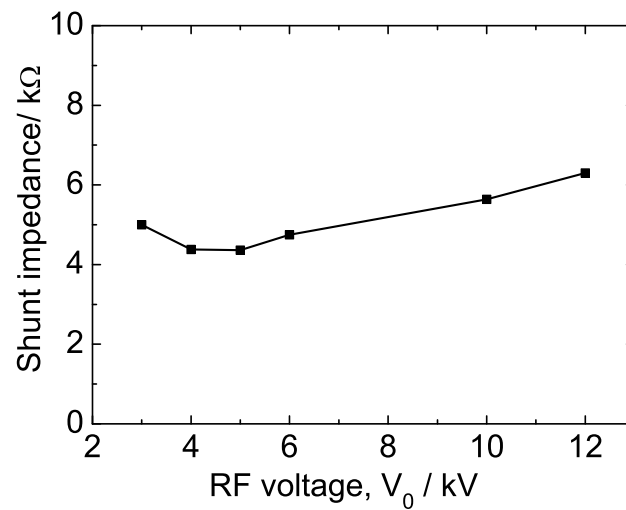


Figure 7.14: Variations in the shunt impedance with V_0 , for the open cavity with fixed-working-point of the tetrode tube.

R_s (Fig. 7.14).

A significant beam loading effect can influence the synchronous phase (Sec. 4.1). In order to observe the phase influence, in terms of synchronous phase ϕ_s , the phase difference

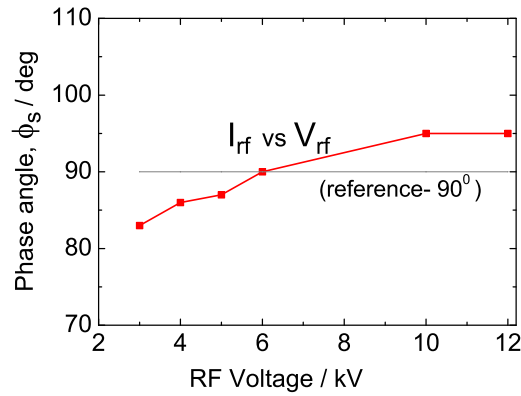


Figure 7.15: The curve is showing the phase angle between the beam current I_{rf} and rf voltage V_{rf} . Some minor deviations from its ideal value of 90° are observed.

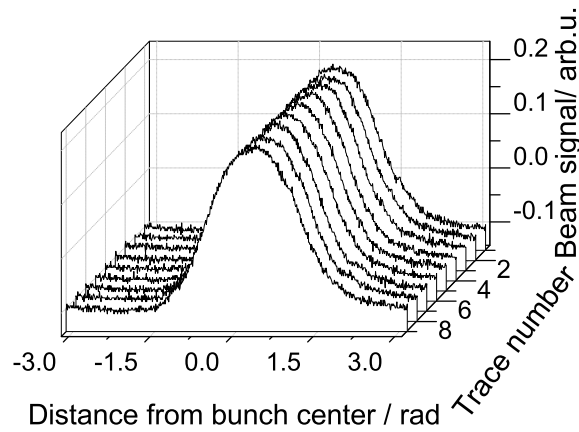


Figure 7.16: An example of the waterfall curves showing a stable bunch evolution with time for a duration of greater than a synchrotron period T_s .

between the beam current I_{rf} and the gap-voltage of the driving cavity V_{rf} have been extracted using the oscilloscope data (Fig. 7.5). The average ϕ_s of 89° (Fig. 7.15) against its ideal value of 90° (Fig. 4.2) is observed. The measurement and observational errors are understood as the source of the deviations ($\approx \pm 10\%$) in the ϕ_s . Also, the length of the cables used to collect the data from the beam pick-up and from the cavities have an influence on this phase information.

From the above measurements, it is fair to conclude that the stability of the beam is intact or uninfluenced with this possibly extreme case of beam loading, with the opened ferrite cavity representing the highest possible R_s .

This result is supported by the stable and uniform evolution of the bunch form (Fig. 7.16).

The waterfall curves are showing the bunch evolution with time for a V_0 of 3 kV. These curves are recorded by using the segmented memory of Lecroy oscilloscope (Sec. 5.2) for the duration of more than the synchrotron period, T_s . After post processing, it is represented as waterfall curve shown in Fig. 7.16.

The uninfluenced ϕ_s (Fig. 7.15) indicates that the control loops in the driving cavity should work independently (Subsec. 4.1.1) and should remain uninfluenced from the beam loading effect which will in any case be lower than the extreme case in the open cavity.

Observations across control loops in driving cavity

For the driving cavity (Fig. 7.1 b), an influence of the beam loading is observed by measuring different outputs of the cavity control loops (Subsec. 2.3.3). The controller output of amplitude control loop (Fig. 2.9) and the bias current output of resonance frequency control loop (Fig. 2.10) are collected in the presence as well as in the absence of beam. As all the measurements are performed at constant frequency f_{rf} and constant voltage

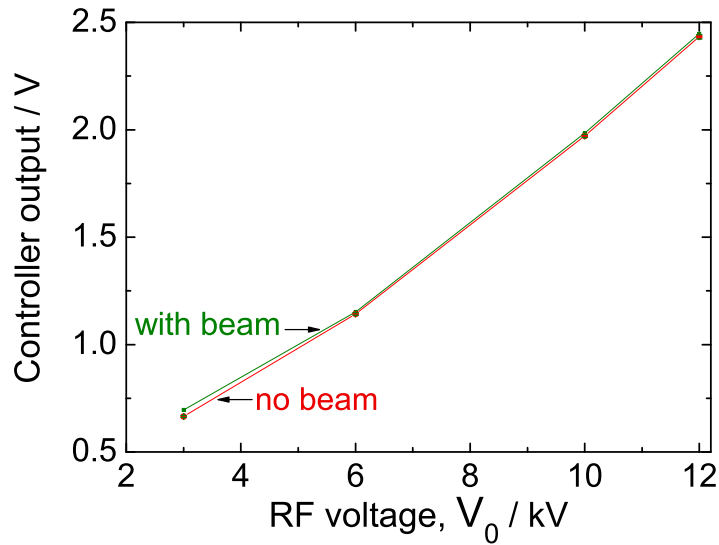


Figure 7.17: The response of controller in amplitude control loop with respect to the cavity gap-voltage for both the cases of with and without beam in SIS ring.

V_0 (for flat top in Fig. 7.4 a), the beam is the only possible source of variations in the outputs of these loops. An increase in the controller output due to the presence of beam is shown in Fig. 7.17. The error bars in this figure are referring the average noise level in the controller output. The controller has a complicated function of adder, subtractor or multiplier and its exact characteristic curve is not available. Therefore, its response to the gap-voltage (the curve labelled as ‘no beam’ in Fig. 7.17) is used to characterize its generalized response. This behavior is referred to correlate the change in the controller

V_0 / kV	V_b / V	$R_s / \text{k}\Omega$
0	75	4.8
5	37	3.2
10	29	2.3
12	25	1.8

Table 7.4: The shunt impedance R_s is calculated for different gap-voltages V_0 by using the derived beam loading voltage V_b from Fig. 7.17. These V_b and their corresponding I_{rf} are mentioned in Table 7.2.

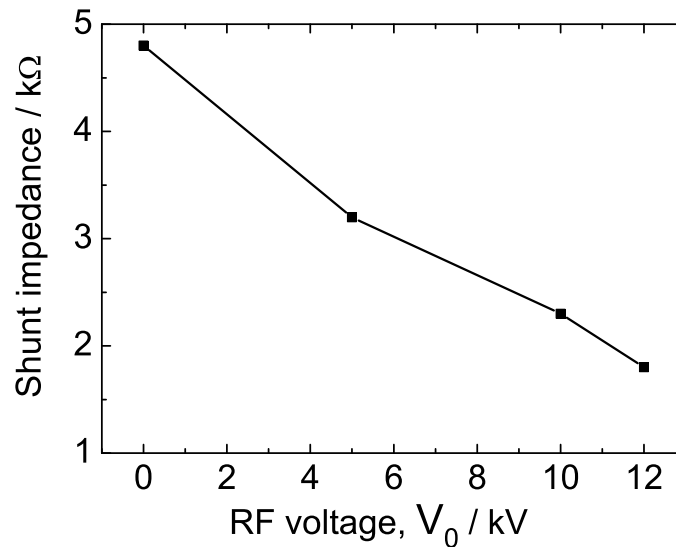


Figure 7.18: The measurement results showing the relationship between the shunt impedance of the driving cavity and the amplitude of gap-voltage V_0 .

output with the corresponding change in the amplitude of the gap-voltage. The presence of the beam being the only difference in both the cases the change in gap-voltage is equivalent to the V_b . By using this voltage V_b (Table 7.4) and the corresponding I_{rf} (Table 7.2) the shunt impedances of the driving cavity, corresponding to different values of V_0 , are calculated (Fig. 7.18). A nearly linear fall in the R_s is observed, which is expected from

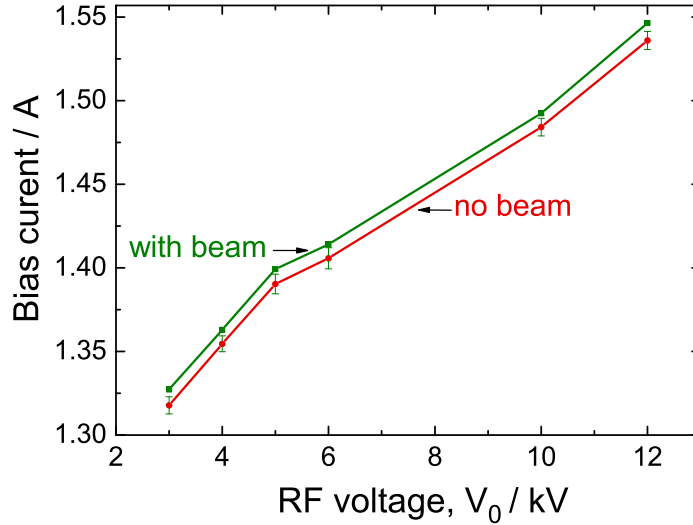


Figure 7.19: Showing an increase in the bias current output of RFCL. Incremental bias current of $\approx 10 - 12\text{mA}$ is equivalent to a frequency offset of 1 kHz (Fig. B.2).

its definition (Eq. 2.2) and from the behavior of the ferrite cavity [33, 31]. *This relation indicates that it is important to consider the amplitude of the gap-voltage V_0 to estimate the shunt impedance R_s of the ferrite cavity.*

An increase in the bias current (Fig. 2.10) with the presence of beam is shown in Fig. 7.19. It would be more precise to call it a shift in the current due to its constant change irrespective of the V_0 or V_b . From the Equations 4.15 and 4.2, the maximum amplitude of the V_b (Table 7.4) can introduce a detuning of 1° . On the contrary, the offset current of ≈ 10 to 12mA (Fig. 7.19) is equivalent to a detuning of 10° . It is found that instead of the beam loading, the DC beam current I_{dc} (Table 7.2) is responsible for this shift. The I_{dc} is shifting the operating point of the cavity on hysteresis curve [31, 33] of the ferrite material of this cavity, which is reflecting as a shift in the resonance frequency of the cavity.

7.4.2 Double rf system

In this case both the ferrite cavities are used as the driving cavities and the interaction of the beam with the opened compressor cavity is studied. This cavity is used as an open cavity (Fig. 7.2 a) and the V_b is measured across its gap. The measurement settings are mentioned in Sec. 7.3. For the beam capturing, the same rf amplitude ramp (Fig. 6.8) is used for both the cavities. For the simulations, the δ_{cb} is extracted from the Schottky

$V_0/$ kV	$V_b/$ V	$I_{dc}/$ mA	$\phi_m/$ deg	Γ	$I_{rf}/$ mA	$R_s/$ k Ω
4, 2	6.4	3.6	143	0.86	3.8	1.67
6, 3	11.2	5.8	141	1.03	6.5	1.72
8, 4	9	4.6	136	1.07	5.4	1.68
12, 6	9.4	4.4	131	1.11	5.3	1.73

Table 7.5: All symbols are denoting the similar parameters as for the srf case. V_0 is mentioned for both the cavities with harmonic 4 and 8 respectively and with $\alpha=0.5$ (Subsec. 3.3.3). Significant variations in I_{dc} are influencing the other parameters.

signal in the similar way as for the srf system (Fig. 7.7).

The compressor cavity possesses a constant shunt impedance R_s , therefore at the constant beam intensity, the maximum amplitude of V_b should ideally depend only on V_0 (Eq. 4.18). In measurements, the beam intensity was kept constant. But the frequent and heavy fluctuations in it are observed (Table 7.5) like srf system. These intensity variations effectively modify the relation between V_b and V_0 as shown in Fig. 7.20. Here, the I_{dc} as well as the V_b , both are normalized to their respective peak values. The exact values of the measured and derived parameters are mentioned in Table 7.2, where the R_s is in good agreement with its designed value of 1.7 k Ω (Table 2.3). It is calculated in the similar way as for the ferrite cavity (Fig. 7.1 a) in the srf system (Fig. 7.14).

One of the main purposes of using the double rf system (Subsec. 3.3.3) in upgraded SIS is to have flat bunches (Sec. 2.11), as it could be observed (Fig. 7.21) for the present arrangement. The bunch length, ϕ_m , is varying by $\approx 12^\circ$ for the whole range of V_0 (in Table 7.2). On the contrary, for the same range of V_0 in srf system these variations are around 45° (Fig. 7.10). *It shows that, unlike srf system, for the drf system with the given settings the amplitude of gap -voltage has much less influence on the bunch length.*

The extent of the beam loading effect is unclear due to the fluctuations in the beam

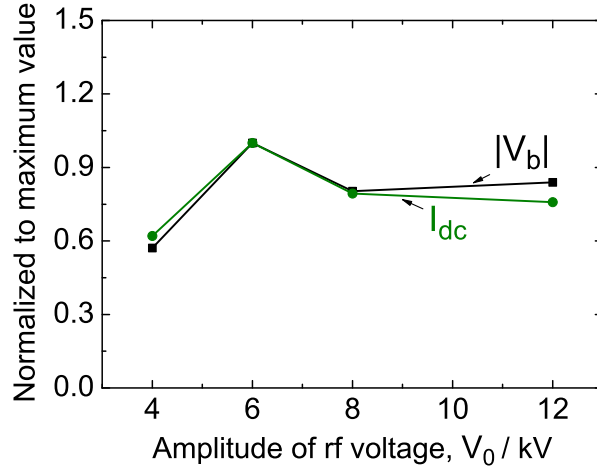


Figure 7.20: Amplitude of beam loading voltage with respect to amplitude of bunching rf. The peak amplitudes of V_b and I_{dc} both are normalized to their maximum values (Table 7.2). In abscissa, the V_0 is mentioned for the cavity with $h=4$ (Subsec. 3.3.3).

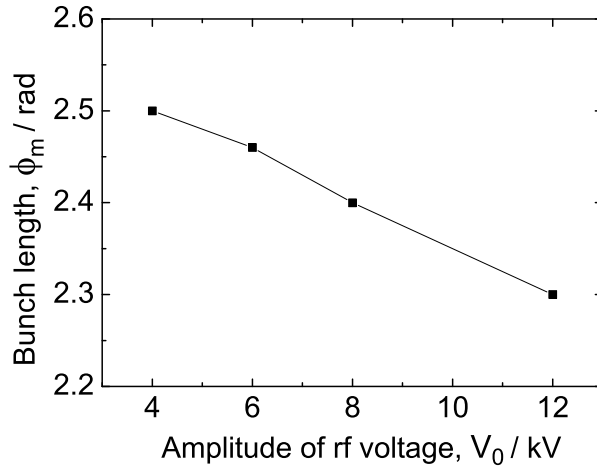


Figure 7.21: The variations in ϕ_m against the V_0 , for the $h=4$ cavity.

intensity (Fig. 7.20). Therefore, the peak amplitude of V_b is normalized to the beam intensity (Fig. 7.22).

The simulations are performed with the similar settings (Table 7.1) and the coasting beam is captured by using the same rf amplitude ramp (Fig. 6.8) as in measurements. The initial phases for the driving cavities are inserted as 0° and -180° respectively. The settings for the other cavity parameters are mentioned in Table 7.6. The $1\Omega R_s$ for the ferrite cavity is based on the observations with the single rf (Subsec. 7.4.1), where no beam loading effect is

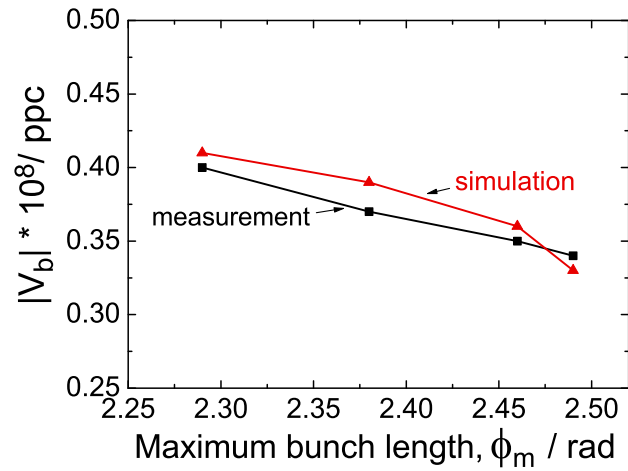


Figure 7.22: Beam loading amplitude normalized to the beam intensity with respect to the half-bunch length in the drf system.

Type of cavity	Q_0	f_r / MHz	R_s / k Ω
Driving (Ferrite)	10	0.86	0.001
Driving (Ferrite)	10	1.72	0.001
Open (MA)	5	0.86	1.7

Table 7.6: The simulation settings of the technical parameters for the cavities in drf operation in present SIS.

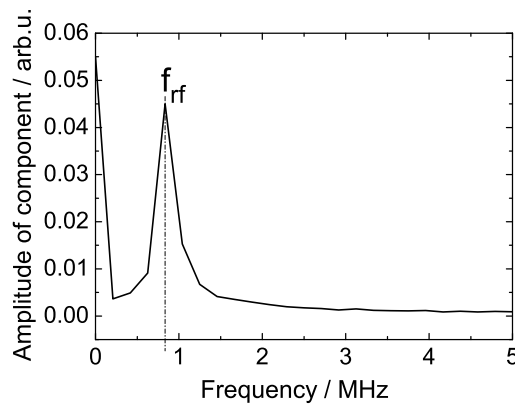


Figure 7.23: An example of the Fourier transform of the bunch signal in the double rf system. It shows the dominance of the component at the fundamental rf frequency f_{rf} .

V_0 / kV	α_{bl}	α_{sc}	ϕ_m / rad	A
4, 2	0.03	0.04	2.49	0.008
6, 3	0.02	0.036	2.46	0.007
8, 4	0.02	0.036	2.38	0.007
12, 6	0.01	0.02	2.29	0.004

Table 7.7: Beam loading, space charge coefficients, half-bunch length and Intensity parameter in drf measurements. All the symbols are denoting the similar parameters as for the srf case.

observed in the driving cavity with the control loops (Subsec. 2.3.3). As Fourier transform

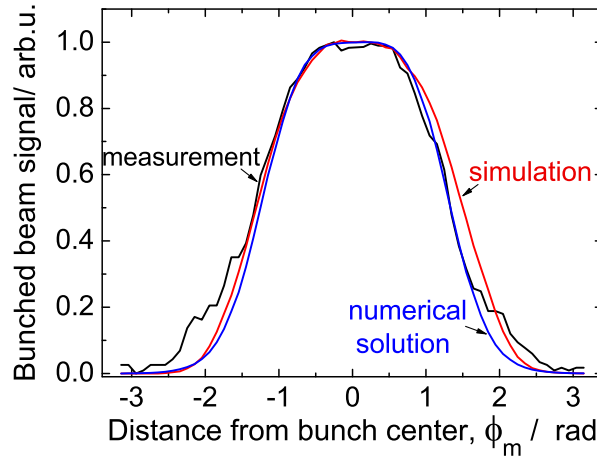


Figure 7.24: The bunch form extracted by analyzing the BPM signal in measurements and its corresponding bunch forms from the simulation and the numerical solution (Eq. 4.28).

of the bunch has only one frequency component at f_{rf} (Fig. 7.23), the beam current I_{rf} is dominated particularly by this frequency component. Thus the compressor (MA) cavity will offer the impedance at f_{rf} , as it is driven only by the beam.

In the relation shown in Fig. 7.22, the variations in V_b/ppc are too low ($\approx 10\%$) for the whole range of ϕ_m . It indicates the constant beam loading for the broad-band cavity irrespective of ϕ_m (or V_0) because the magnetic properties of the core material (MA) are uninfluenced from V_0 . The relation from the simulations in Fig. 7.22 are found in good

agreement with the corresponding measurement. The minor differences can be interpreted as observational errors in the measurements. Further, the corresponding bunch forms are shown in Fig. 7.24. An influence of the beam loading (Subsec. 4.5.2), if it is significant enough, is expected in the middle region of the flattened bunch in Fig. 7.24. But, it is clearly evident from the results summarized in Table 7.7 that *the beam loading effect in this case is not strong enough to influence the particle distribution. The bunches from the measurement, simulation and from the numerical solution (Eq. 4.28) are matching well.*

7.4.3 For upgraded SIS

In the planned double rf system, the MA and ferrite cavities will work at harmonic 2 and 4 respectively with α of 0.5 (Subsec. 3.3.3). The beam and cavity parameters are same as

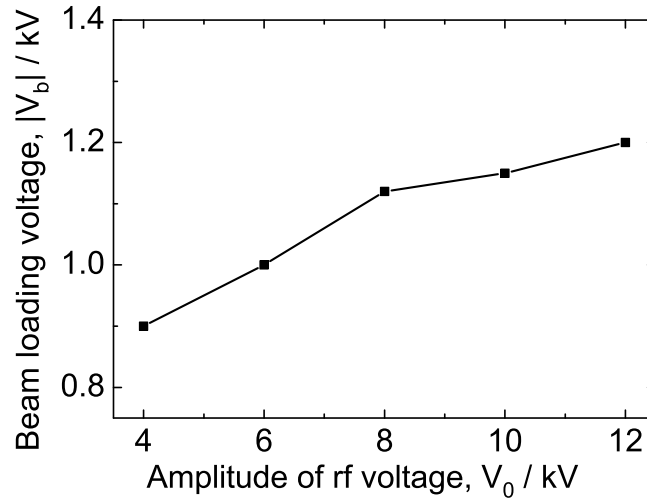


Figure 7.25: Illustrates the variations in V_b with V_0 (in $h=2$ cavity) for the double rf system in upgraded SIS (Sec. 2.11). This behavior corresponds to the parameters, α_{bl} , α_{sc} and A , mentioned in Table 4.3.

for the capture study (Table 6.3). The variations in the amplitude of the V_b in the $h=2$ cavity with respect to V_0 are shown in Fig. 7.25. It is for a constant beam intensity of $5.8 \cdot 10^{11}$ for Ar^{18+} ions. Here, the beam loading effect is remarkably large to produce $\approx 50\%$ of beam loading voltage V_b for the rf voltage V_0 of 2 kV. Also, in contrast to the Fig. 7.20, a significant variations ($\approx 30\%$) in the beam loading are observed for the constant beam intensity and with constant R_s (independent of V_0) for this $h=2$ cavity. The difference in the harmonic numbers h i.e. 4 and 2 for the present and upgraded SIS respectively, can be the source of this behavior.

The bunch representing this case with the parameters α_{bl} , α_{sc} and intensity parameter, A (Table 4.3) is shown in Fig. 7.26. In comparison to the bunch forms for the present SIS

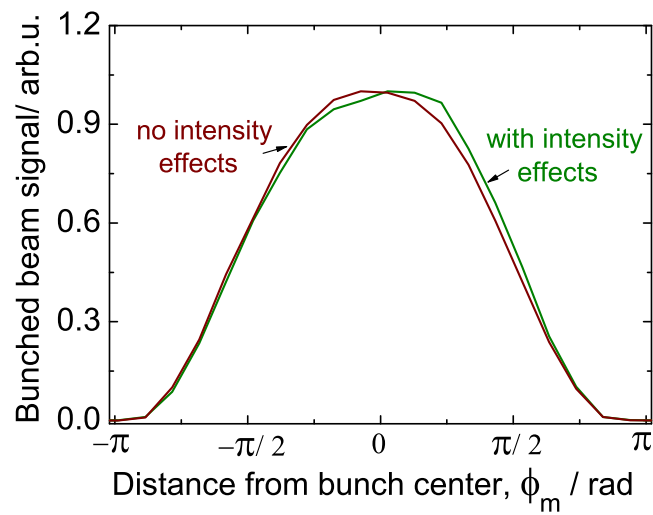


Figure 7.26: The particle distribution with and without the consideration of the intensity effects in the upgraded SIS.

(Fig. 7.24) and the one with no intensity effect (Fig. 7.26), a tilt in the middle part of the bunch is observed (Subsec. 4.5.2). *It indicates a significant beam loading effect due to the $h=2$ cavity in the upgraded SIS with the double rf system.*

Chapter 8

Summary and Outlook

In the present work, longitudinal beam loading effect due to the ferrite and the broad-band cavity is investigated. An interaction of the high-intensity beam with the cavity impedance results in the absorption of beam power in the cavity. It influences the longitudinal particle motion, the particle distribution and as a result, affects the beam stability. The numerical solution and simulation of the beam loading along with the space charge effect, for an adiabatically captured beam in both single and double rf buckets, in the present SIS are found in good agreement with the measurement. Taking these results as the reference, the effects are simulated and predicted for the upgraded SIS.

The particle simulation is carried out in particle-in-cell code ESME. The longitudinal phase space development in the capturing process and emittance or bunch lengths under the influence of the different rf ramps are observed. The beam loading and space charge, both beam intensity effects, with the consideration of the perfectly conducting beam pipe have been included successfully.

The Keil-Schnell criterion, defining the condition for the stability of the coasting beam interacting with its surroundings, was found well above the limits of space charge and cavity impedances for the given beam parameters in the present SIS. But for the upgraded SIS, the space charge, broad-band and ferrite cavity impedances were all exceeding the limits for the same beam parameters but with the upgraded beam intensity. In this case, the beam or the cavity parameters are to be adjusted to prevent the longitudinal instability in the coasting beam.

Dedicated measurements have been performed to assure the adiabatic capture of the coasting beam in SIS, which is accomplished by optimizing the rf amplitude ramp parameters for the single as well as double rf systems. In both the cases, *the optimized ramping time of 20 ms is found which is within the limited time allotted for the beam capturing in the machine cycle.* This machine cycle depends upon the required frequency of beam extraction.

The bunch oscillations were observed and the mismatch between rf frequency and beam energy was understood as their source. In a supplementary measurement as well as in simulations, a significant influence of this mismatch on the bunch length was observed. *This study highlights the importance of matching the frequency corresponding to injection*

energy to the rf frequency for an adiabatic capture.

A scaling parameter χ is defined to assure the adiabatic capture of the coasting beam with the chosen value of the initial voltage; as it can not be zero due to the practical limitations. The flat and stable bunches were observed in the double rf bucket where the two ferrite cavities were synchronized by a dedicated digital signal processing system. *During the capturing process in the present SIS, no influence of the beam intensity on the beam has been observed but a significant difference in the bunch length or emittance in the upgraded SIS has been observed in simulations.*

An intensity parameter combining the beam loading and space charge effects is introduced to define the slope in the middle of the particle distribution. The parameter shows that the beam loading induces a tilt and space charge can compensate for it. *From the numerical solution and the ESME simulation, this slope or tilt was found insignificant for the present SIS parameters, but they predict a significant slope for the upgraded SIS. The beam intensity-dependent deformation of the particle distribution was observed and matched well with the theoretical estimation.*

Several experiments have been performed with different beam and machine (SIS) settings to measure the beam loading effect. A steady-state type of beam loading is predicted by using the measurement results from the ferrite test cavity, which was later confirmed through the experiments in SIS. It was found that the most of the beam power was absorbed at the fundamental rf frequency for single as well as double rf driven beam. *It confirms the dominance of this fundamental frequency component for the narrow-band ferrite cavity.*

The shunt impedance of the ferrite cavity matched well with the impedance of its prototype. This shunt impedance, as expected, varies with the amplitude of the rf voltage due to the change in the permeability of the ferrite core. It signifies *the importance of the amplitude of the rf voltage in the cavity to pick the right value of the shunt impedance offered by it to the beam.* The method used to derive the shunt impedance is verified, as the impedance for the bunch compressor cavity derived using it is matched to the designed value of impedance for this cavity.

The amplitude of the beam loading voltage for the opened ferrite cavity, which represents the extreme case of the shunt impedance, is found too low to influence the bunch in a single rf bucket. *The synchronous phase angle was constant during the whole range of the rf amplitude variations.* The minor fluctuations in it are attributed to the measurement and observational errors. The beam intensity, in this case, was in the range of the highest possible level. In this condition, *the control loops in the driving cavity were found uninfluenced with the beam loading effect.* In the resonance frequency control loop measurements *the influence of the beam current on the operating point of the ferrite cavity was observed.*

For the double rf system, the bunch compressor cavity was used as a source of the well known broad-band impedance in the ring and had no influence on the beam. The simulations for the planned harmonic 2 system with ferrite and broad-band magnetic alloy cavity in the upgraded SIS, shows a significant tilt in the middle part of the bunch in comparison to the one with no intensity effects. It indicates that *the preventive measures will be needed to compensate for the beam loading effect in the upgraded SIS.*

The beam loading effect for the present SIS was found too low to influence the beam but is an important issue of concern in case of the upgraded SIS. *While the influence of this effect for the upgraded SIS can perhaps be predicted qualitatively, the exact time development of the instability behavior, including emittance growth, can be best determined in further study and experiment.*

Appendix A

Symbols and Abbreviations

Table A.1: List of symbols. Variables subscripted with 0 refers to the nominal value of the physical parameter represented by the variable. Δ indicates a shift in the quantity represented by the subsequent parameter.

Symbol	Explanation
A	intensity parameter, including beam loading and space charge effects
a	radius of the cross section of a uniformly distributed continuous beam
α	ratio of the amplitudes of the rf voltages at the fundamental rf frequency and at its higher harmonic in double rf system
α_{bl}	beam loading coefficient, shows the beam loading potential in comparison to the external rf potential
α_{ia}	iso-adiabatic coefficient, defined for the iso-adiabatic rf amplitude ramp
α_p	momentum compaction factor
α_{par}	parabolic coefficient, defined for the parabolic rf amplitude ramp
α_{rf}	rf coefficient
α_{sc}	space charge coefficient, shows the space charge potential in comparison to the external rf potential
b	radius of a circular beam pipe
β	velocity divided by c
β_c	coupling coefficient defining power transfer between two rf components
\vec{B}_φ	azimuthal magnetic field of beam, $B_\psi = \vec{B}_\psi $
C	equivalent capacitance of the rf cavity
C_g	gap capacitance of the rf cavity
c	$= 2.998 \cdot 10^8$ m/s, speed of light in vacuum
$\Delta\phi$	deviation in the phase of the charged particle on the rf voltage wave
ΔE	deviation in the energy of the non-synchronous particle
ΔL	deviation in the orbit length of the non-synchronous particle
$\Delta\omega$	deviation in the revolution frequency of the non-synchronous particle
Δp	deviation in the momentum of the non-synchronous particle

$(\Delta p/p)_{cb}$	maximum momentum spread of the coasting beam
$(\Delta p/p_0)_{rf}$	height of the bucket created by the rf voltage
$(\Delta p/p)_{rms}$	rms momentum spread of the bunched beam
$\Delta\phi$	deviation in the phase position of the non-synchronous particle with respect to the rf wave
$\Delta\tau$	deviation in the revolution period of the non-synchronous particle
$\Delta\theta$	deviation in the phase of the non-synchronous particle in the synchrotron ring
ΔU	deviation in the electrical energy of the particle while crossing the rf cavity
Δv	deviation in the velocity of the non-synchronous particle
δ	$= (p - p_0)/p_0$, normalized momentum distribution, $\dot{\delta}$ is its derivative
δ_{cb}	rms momentum spread of the coasting beam
E	total energy of the non-synchronous particle
E_0	total energy of the synchronous particle
E_r	radial electric field due to space charge effect
E_w	electric field on the beam pipe wall
E_z	longitudinal electric field due to space charge effect
E_{kin}	kinetic energy
\vec{E}	electric field, $E = \vec{E} $
E_p	$= m_p c^2 = 938.3 MeV$, energy of a proton at rest
e	$= 1.602 \cdot 10^{-19} C$, elementary charge, charge of proton or electron
ϵ_{rms}	rms value of longitudinal emittance
ϵ_0	$= 8.854 As/Vm$, electric constant
η	$= 1/\gamma_T^2 - 1/\gamma^2$, slip factor
F	form factor
f	frequency in Hz
f_0	revolution frequency of the synchronous particle
f_r	resonance frequency of the cavity
f_{bw}	frequency bandwidth of the cavity
f_{rf}	frequency of the rf voltage
f_s	synchrotron frequency of particle
\hat{g}	$= \text{Im}(r_0)$
γ	Lorentz factor
γ_t	transition point of a synchrotron
Γ	fraction of the beam current appears as the rf current
h	harmonic number; harmonic of the revolution frequency, f_0
I_a	anode current of the tetrode tube
I_b	beam current
I_{bias}	dc bias current in the ferrite cavity
I_g	current from the rf generator

I_{dc}	dc component of the beam current
I_1	beam current at fundamental rf frequency
I_n	beam current
I_{rf}	rf component of the beam current
I_{sec}	current in the secondary winding of the CT
L	circumference of the synchrotron ring
L_{eq}	a lumped parameter, representing the inductance of the cavity, in parallel equivalent circuit of the rf cavity
L_g	length of the cavity gap
m_0	$1.673 \cdot 10^{-27}$ kg, proton mass
m^*	effective proton mass
N_b	number of particles per bunch
N	number of particles per cycle; ppc
n	harmonic of the rf frequency f_{rf}
ω	$= 2\pi f$, angular frequency in rad; analogously with any prefix or subscript
p	momentum; analogously with any prefix or subscript
ϕ	phase of the synchrotron oscillation
$\dot{\phi}$	$= \phi/t$
$\phi_{bl}, \dot{\phi}_{bl}$	change in the phase corresponding to the peak line density, due to the beam loading effect
ϕ_{rf}	phase of the synchrotron oscillation
ϕ_s	phase position of the synchronous particle on the rf wave
ϕ_m	maximum bunch length; maximum phase excursion of the particle in the bunch
Ψ	momentum distribution
ψ	betatron phase
Q_0	unloaded quality factor of the rf cavity
Q	$Q_0/(1 + \beta_c)$, unloaded quality factor of the rf cavity
q	atomic number of the charged particle; equal to number of protons in nucleus less number of electrons in the shells
R	$= L/2\pi$, mean synchrotron radius
R_{cav}	shunt impedance of the rf cavity alone
R_g	impedance at the last stage of the coupling transformer transformer
R_s	shunt impedance of the rf cavity along with the R_g
S_{coast}	phase space area of the coasting beam
S_{bunch}	phase space area of the bunched beam
σ	standard deviation of a distribution
σ_{rms}	rms bunch length of the longitudinal
T_r	$= 2Q/\omega_r$, rise time of the rf cavity
T	$= 1/f$, time period in second; analogously with the subscripts, 0,s and rf
T_{tr}	transit time factor
t	time
τ	revolution period of the non-synchronous particle

θ	$= \theta_0 + \omega_0 t$, azimuthal angle
t_{ramp}	ramping time; time to switch on the final amplitude of the rf voltage during beam capturing at injection
V_0	maximum amplitude or peak value of the rf voltage
V_b	beam loading voltage
V_{rf}	$= V_0 \sin \omega_{rf} t$, instantaneous value of the rf voltage
V_a	anode voltage of the tetrode tube
V_g	screen grid voltage of the tetrode tube
V_{gc}	control grid voltage of the tetrode tube
V_s	space charge voltage of the tetrode tube
v	particle velocity
X_s	reactance representing the longitudinal space charge effect
χ	scaling factor relating the initial voltage with coasting beam
Y	$= (1/ V) \int V(\phi) d\phi$, potential corresponding to the respective voltage (with different subscripts)
Z_0	$= 377 \Omega$, impedance of vacuum
Z^{\parallel}	longitudinal impedance; analogously with any prefix or subscript
z	subscript for longitudinal coordinate

Table A.2: List of abbreviations.

Abbreviation	Explanation
ac	alternating current
ACL	Amplitude Control Loop
AWG	Arbitrary Waveform Generator
BPM	Beam Position Monitor
Chap.	Chapter
CT	Current Transformer
dc/ DC	Direct Current
DDS	Direct Digital Signal
drf	double rf
DSP	Digital Signal Processing
Eq.	Equation
ESR	‘Experimentier SpeicherRing’
FAIR	Facility for Antiproton and Ion Research
Fig.	Figure
GSI	‘Helmholtzzentrum für Schwerionenforschung GmbH’
MA	Magnetic Alloy
NA	Network Analyzer
ppc	particles per cycle
rf/ RF	Radio Frequency
RFCL	Resonance Frequency Control Loop
Sec.	Section
SIS-18 or SIS	‘SchwerIonenSynchrotron 18’
srf	single rf
Subsec.	Subsection

Appendix B

Test Cavity Measurements

Due to the technical reasons the cavity in the SIS ring (Fig. 2.2, 2.6) is accessible only during the shutdown period. Therefore, several experiments are performed on its prototype to gain more understanding about its behavior which is necessary from the beam loading measurements point of view. The prototype of the cavity is similar to the ring cavity (Table 2.2) except the lower capacity of its power supply [36]. Several important parameters of the cavity such as the dependence of resonance frequency, f_r on the bias and anode currents (I_{bias} and I_a), Q value (Eq. 2.1), rise time, T_r (Eq. 2.7) and shunt impedance R_s (Eq. 2.3) have been measured. An example of the experimental setup used for these measurements and some relevant results, from the beam loading measurements point of view, are explained below.

B.1 Experimental set-up

A Sony-Tektronix 87512A Network Analyzer (NA) supplying rf power to the cavity in reflection arrangement is shown in Fig. B.1. As its output impedance of 50Ω is mismatched to the high impedance of the cavity [32], most of the power is reflected back to the NA. This power is quantified by using the reflection factor, $\Gamma_{ref} = \text{reflected power}/\text{incident power}$, along with the coupling coefficient

$$\beta_c = 1/(1 + \Gamma_{ref}) \quad (\text{B.1})$$

[32, 100]. For two different experiments, bias and anode currents are varied alternately while keeping the other one constant. The corresponding response of the cavity, in terms of its resonance frequency, Q factor and shunt impedance, is observed (Fig. B.2). In both the cases, the bandwidth f_{bw} (Eq. 2.8) and the resonance frequency f_r are observed from the resonance curve (Fig. 2.8) in the NA and are used to calculate the Q factor. By using this Q factor and the rf power from the NA, the coupling coefficient β_c (Eq. B.1) and Q_0 (Eq. 2.1) are calculated.

Further, the shunt impedance R_s is calculated by using Q_0 , and the gap-capacitance C_g , which is measured by the perturbation method [100]. Following are the key highlights of the results (Fig.B.2).

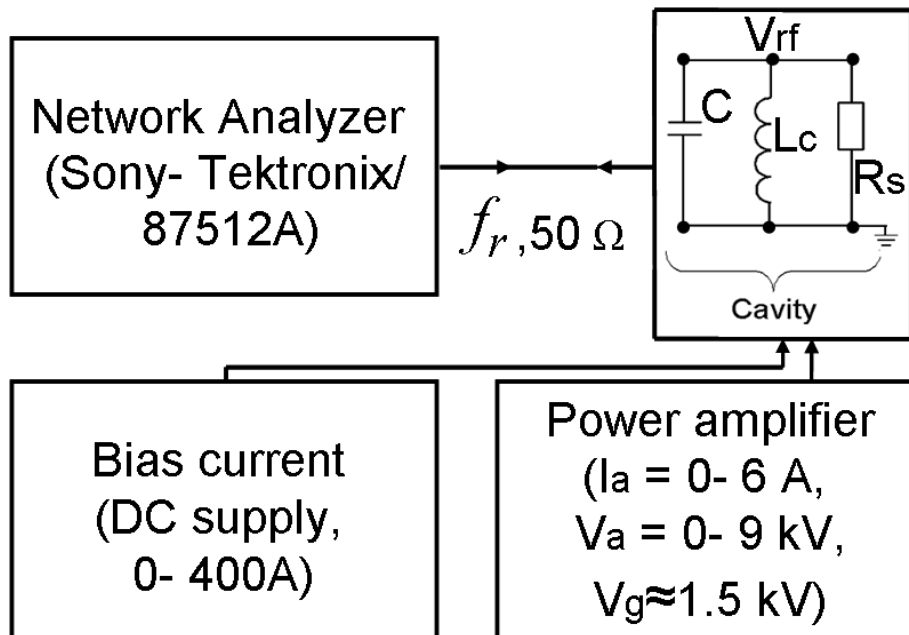


Figure B.1: Block diagram showing setup for the measurements with the test cavity. NA is supplying rf power to the cavity at frequency, f_r and with the coupling impedance of 50Ω in reflection mode [32]. DC current, I_{bias} is supplied to the bias-winding (Fig. 2.6) of the cavity. Also, the anode current, I_a of the power amplifier is adjusted to vary its working point by keeping anode and screen-grid voltages constant.

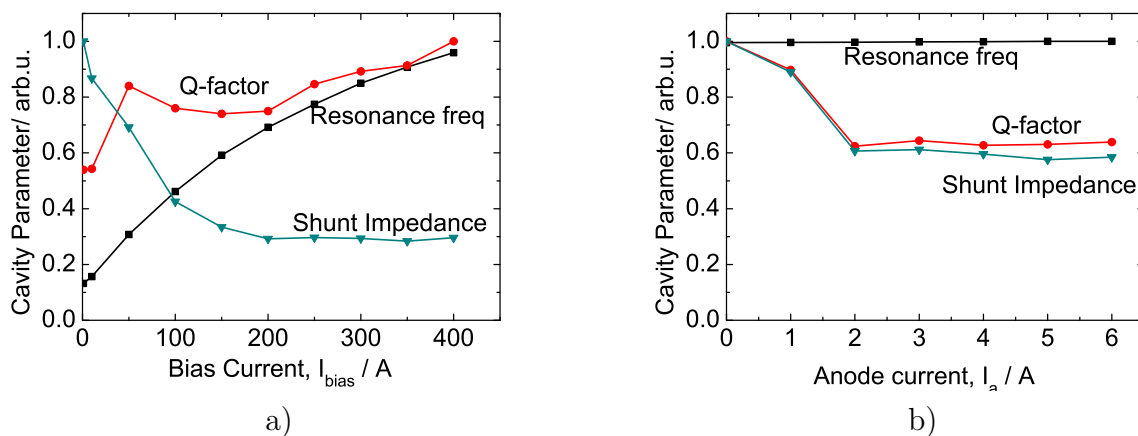


Figure B.2: Variations in the resonance frequency, Q factor and shunt impedance with a) I_{bias} keeping $I_a=0 \text{ A}$ b) I_a keeping $I_{bias}=50 \text{ A}$.

- All the parameters are normalized to the respective maximum values.
- The f_r is fully controlled by the I_{bias} [31] and is almost independent of the variations in I_a (Fig. B.2 b).
- The I_{bias} of 10 - 13 A (Fig. B.2 a) is the range corresponds to the frequency (at injection energy) at which all the beam loading measurements are performed. A change of nearly 1 A corresponds to the 100 kHz in this region, as the f_r is varying from 0.65 to 5.5 MHz.
- The connection of the power amplifier (tetrode tube) causes its impedance to appear in parallel to the cavity and thus effectively reduces the cavity impedance (Fig. B.2 b). As soon as the tube impedance settles to a fixed-working-point, R_s is also stabilized to a fixed value. Similarly, Q_0 is transformed into the loaded quality factor Q .

Some useful results are summarized in the Table B.1. The R_s from the test cavity

Serial No.	$I_{bias}/$ A	$I_a/$ A	$f_r/$ MHz	Q	$R_s/$ k Ω
1	0 – 400	0	0.67 – 4.84	43 – 80	14 – 4.2
2	50	0 – 6	1.57 – 1.58	52 – 33	8.1 – 4.7

Table B.1: Summary of the experimental results from the test cavity. In the first row, the results are with the fixed dc-working-point of the tetrode tube and variable I_{bias} . In the second row the results are for variable I_a with constant I_{bias} .

(Table B.1) and from the SIS cavity (Fig. 7.14) are in the same range. The minor deviations can be attributed to the difference in the cavity settings.

Bibliography

- [1] P.J. Bryant. *A Brief History and Review of Accelerators*, CERN, 1994.
- [2] <http://www.gsi.de/library/GSI-Report-2006-15>
- [3] H.H. Gutbrod (Editor in Chief) I. Augustin, H. Eickhoff, K.-D. Groß, W.F. Henning, D. Krämer, G. Walter. *FAIR Baseline Technical Report*, <http://www.gsi.de/fair/reports/btr.html>, 2006.
- [4] <http://www.gsi.de/documents/DOC-2008-May-86-1.pdf>
- [5] K. Blasche, B. Franczak. *The Heavy Ion Synchrotron SIS*. In Proc. of EPAC, 1992.
- [6] P. Spiller, U. Blell, O. Boine-Frankenheim, H. Eickhoff, P. Forck, G. Franchetti, B. Franczak, H. Klingbeil, C. Omet, H. Reich, H. Ramakers, A. Redelbach, U. Scheeler, P. Schüt. *SIS18 Status Report* ,GSI Scientific Report 2006.
- [7] S.Y. Lee. *Accelerator physics*. World Scientific. Second Edition, 2004.
- [8] J. Le Duff. *Longitudinal dynamics*. CAS on Intermediate Level Accelerator Physics Course. Daresbury, 16-28 Sep2007.
- [9] W. Pirkel. *Longitudinal beam dynamics*, CERN Accelerator School: 5th Advanced Accelerator Physics Course, Rhodes, Greece, 20 Sep - 1 Oct1993, pp.233-257.
- [10] K.Y. Ng. *Physics of Intensity Dependent Beam Instabilities*. World Scientific, 2006.
- [11] H. Wiedemann. *Particle Accelerator Physics*, Third Edition. Springer, 2007.
- [12] M. Reiser. *Theory and design of charged particle beams*. Wiley. New York, USA, 1994.
- [13] D.A. Edwards and M.J. Syphers. *An Introduction to the Physics of High Energy Accelerators*. John Wiley and Sons, New York, 1993.
- [14] E.M. McMillan. “*The synchrotron - a proposed high-energy particle accelerator*”, Phys. Rev., Letter to the editor, 68 (September1945), 1434.
- [15] V. Veksler. J. of Phys, USSR, 9 (1945), 153–158.

- [16] K.Y. Ng. *Lecture Notes on Physics of Intensity Dependent Instabilities*. USPAS, Jan2002.
- [17] D. Boussard. *Beam loading (particle accelerators)*. CERN Accelerator School: 5th Advanced Accelerator Physics Course, Rhodes, Greece, 20 Sep - 1 Oct1993, pp.415-436.
- [18] A. Gamp. *Servo control of RF cavities under beam loading*. CERN Accelerator School: RF Engineering for Particle Accelerators, Oxford, UK, 3 - 10 Apr1991, pp.396-415.
- [19] K. Harkay et al. *Beam loading Effect in APS Booster*. ANL/ ASD/CP 90024.
- [20] P. Baudrenghien. *Low-level RF systems for synchrotrons. : part I: The low-intensity case*. CERN Accelerator School: Radio Frequency Engineering, Seeheim, Germany, 8 - 16 May2000, pp.146.
- [21] D. Boussard. *Control of cavities with high beam loading*. IEEE Transactions on Nuclear Science, Vol. NS-32, No. 5, Oct1985, pp.1852-56.
- [22] P. Baudrenghien. *Low-level RF systems for synchrotrons. : part II: High Intensity Compensation of the beam induced effects*. CERN Accelerator School : Radio Frequency Engineering, Seeheim, Germany, 8 - 16 May2000, pp.175-209.
- [23] F. Pedersen. *Beam loading effects in the CERN PS booster*. IEEE Trans.Nucl.Sci. NS-22(1975), Vol.3, pp.1906-09.
- [24] R. Garoby. *Low level RF and feedback*. Joint US-CERN-Japan Accelerator School on Frontiers of Accelerator Technology, Tsukuba, Japan, 9 - 18 Sep1996, pp.455-489.
- [25] D. Boussard. *Beam loading*. Proc. CERN Accelerator School, Oxford, 1985, CERN 97-03 (1997).
- [26] K.W. Robinson. *Radiofrequency Acceleration II*. CEA (MIT-Harvard)-11. 10 Sep1956. Technical information division, Berkley. 1 Jun1961.
- [27] K.W. Robinson. *Stability of Beam in Radiofrequency System*. CEA (MIT-Harvard)-11. 27 Feb1964.
- [28] G. Kalisch. *Erzeugung und Untersuchung gepulster Schwerionen-Strahlen höchster Phasenraumdichte im Experimentier-Speicherring der GSI*, PhD Thesis, Technische Universität Darmstadt, 1993, GSI-94-05, Jan1994, ISSN 0171-4546.
- [29] G. Rumolo. *Theory and Experimental Verification of the Longitudinal Instability of Cooled Coasting Beam at the Heavy Ion Storage Ring ESR*, PhD Thesis, University of Naples, Italy, 1999.
- [30] H. Klingbeil. Lecture notes. "http://www.temf.de/fileadmin/Lehre/Dokumente/HK_HF_Beschleunigung.pdf".

- [31] I.S.K. Gardner. *Ferrite dominated cavities*. CERN Accelerator School: RF Engineering for Particle Accelerators, Oxford, UK, 3 - 10 Apr1991, pp.349-374.
- [32] H. Klein. *Basic Concepts I*. Proceedings, Advanced Accelerator Physics, Vol.I, pp.97-124. Oxford, 1985.
- [33] Q.A. Kerns, G. S. Tool and J. E. Katz. *Ferrite Measurements for Synchrotron RF Accelerating System Design*. IEEE1965, pp.185- 190.
- [34] M. Puglisi. *Conventional rf cavity design*. CERN Accelerator School: RF Engineering for Particle Accelerators, Oxford, UK, 3 - 10 April1991, pp.156-197.
- [35] G. Dôme. *Theory of Rf Acceleration*. Proceedings, Advanced Accelerator Physics, VolI, pp.110-158. Oxford, 1985.
- [36] H.G. König, GSI. *Private communication*.
- [37] K. Kaspar, H.G. König. *Development of Fast Feedback System for the GSI SIS Cavities*. EPAC 2000 Vienna, 26- 30 June/ Poster TUP 5A08.
- [38] U. Laier, GSI. *Private communication*.
- [39] The ESME Homepage: <http://www-ap.fnal.gov/ESME/> .
- [40] J. MacLachlan. *Fundamentals of particle tracking for longitudinal projection of beam phase space in Synchrotrons*. FermiLab note, FN-481, 15 Apr1990, Batavia, Illinois.
- [41] J. MacLachlan. *Longitudinal phase Space Tracking With Space Charge and Wall Coupling Impedance*. FN-446. February1987.
- [42] S. Stahl and S.A. Bogacz. *Simulation of Coupled Bunch Mode Growth by A High Q Resonator*. Proceeding 13th IEEE Particle Accelerator Conference at Chicago, USA (20-23 Mar1989), pp.1175-77.
- [43] R. Averill et al. *Application of third harmonic of the accelerating frequency in Cambridge Electron Accelerator*. Proceeding of 8th International Conference on High Energy Accelerators, CERN, Geneva, Switzerland, pp.301
- [44] A. Hofmann and S. Myers. *Beam dynamics in a double RF system*. Proc. of the 11th Int. Conf. on High Energy Acc. ISRTH- RF/80-26 (1980).
- [45] S. Koscielniak. *Stability Analysis of a Beam Loaded Double R.F. System*. TRIUMF, 4004 Wesbrook Mall, Vancouver, B.C.Canada.
- [46] C. Carli, M. Chanel. *Creation of Hollowbunches by Redistribution of Phase Space Surfaces*. Proceedings of EPAC 2002, Paris, France.

- [47] E.N. Schaposhnikova. *Bunched Beam Transfer Matrices in Single and Double RF Systems*. European Organization for Nuclear Research CERN. CERN SL/94-19 (RF).
- [48] A. Hofmann. *Beam Instabilities*. CAS - CERN Accelerator School: Course on Synchrotron Radiation and Free-Electron Lasers, Brunnen, Switzerland, 2 - 9 Jul2003, pp.139-185
- [49] A. Hofmann. *Landau damping CERN Accelerator School Intermediate accelerator physics*. DESY, Zeuthen, Germany 15 – 26 Sep2003
- [50] P. Huelsmann, O. Boine-Frankenheim, H. Klingbeil, G. Schreiber. *Consideration Concerning the RF System of the Accelerator Chain SIS12/18- SIS100 for the FAIR project at GSI*. GSI Scientific Report 2004.
- [51] H. Klingbeil, P. Hülsmann. *Status of FAIR RF System Development*. GSI Scientific Report 2006.
- [52] O. Boine-Frankenheim. “Collective effects” activities at GSI and TUD as part of the EU-design study “DIRACsecondary beams”. www.linux.gsi.de/~boine/CARE/Day2/Boine1.ppt.
- [53] C.E. Nielsen, A. M. Sessler. *Longitudinal Space Charge Effects in Particle Accelerators*. Rev. Sci., Instr. Vol.36, 1965, pp.429-436.
- [54] V.K. Neil, A.M. Sessler. *Longitudinal Resistive Instabilities of Intense Coasting Beams in Particle Accelerators: The Helical Insert*. CERN 68-1, CERN, Geneva, Switzerland, 1968.
- [55] O. Boine-Frankenheim, T. Shukla. *Space Charge Effects in Bunches for Different rf Wave Forms*. Phys. Rev. ST Accel. Beams 8, 034201, 2005.
- [56] E. Ezura, S. Takeda, K. Kudo and M. Kondoh. *Longitudinal Behaviour of Beam in KEK Booster*. IEEE Transaction Nuclear Science, Vol. NS-26, No.3, June1979, pp.3538-40.
- [57] R.D. Kohaupt. *Single Beam Instabilities in PETRA*. IEEE Transaction Nuclear Science, Vol. NS-26, No.3, June1979. pp.3480-81.
- [58] C.G. Lilliequist and K.R. Symon. Deviations from adiabatic behaviour during capture of particles into an R. F. Bucket. MURA Internal Report. MURA-491. Madison, Wisconsin. 20July1959.
- [59] J.A. Maclachlan. *Rf capture in the NAL Booster*. National Accelerator Laboratory. TM-303. 17May1971.
- [60] J. Gareyte, L. Magnani, F. Pedersen, F. Sacherer and K. Schnidl. *Beam dynamics Experiments in PS Booster*. IEEE Transactions on Nuclear Science, Vol. NS-22, No.3, Jun1975, pp.1855-58.

- [61] M. Kirk, H. Damerau, I. Hofmann, O. Boine-Frankenheim, P. Spiller, and P. Hülsmann. *Phase space growth during RF capture in the GSI heavy ion synchrotron SIS-18*. Laser and Particle Beams (2003), 21, 85–89. Printed in the USA.
- [62] O. Boine-Frankenheim, I. Hofmann. *Simulation and observation of nonlinear longitudinal space-charge phenomena in coasting beams*. Numerial Instruments and Methods in Physics Research A 441 (2000) 28-35.
- [63] S. Appel. *Optimization of the Injection into SIS-18*. PhD work in progress, in Beschleuniger Physik group at GSI.
- [64] P.M. Lapostolle. *Possible Emittance Increase through Filamentation due to Space Charge in Continuous Beams*. IEEE Trans. Nucl. Sci., NS-18, 1971, pp.1101-04.
- [65] F.J. Sacherer. *RMS Envelope Equations with Space Charge*. IEEE Trans. Nucl. Sci., NS-18, 1971, pp.1105-07.
- [66] S. Stahl and C. Anckenbrandt. *Simulation of the Capture process in the Fermilab Booster*. Proceeding 1987IEEE Particle Accelerator Conference at Washington(16-19 Mar1987), pp.1117-19.
- [67] P. Spiller, K. Blasche, O. Boine-Frankenheim, M. Emmerling, B. Franczak, I. Hofmann, S. Lund, U. Ratzinger. *Generation of High Power Heavy Ion Beams at GSI*. Proceedings of Particle Accelerator Conference, New York, 1999.
- [68] C.G. Montgomery, R.H. Dicke, E.M. Purcell. *Principles of Microwave Circuits*. McGRAW-HILL BOOK COMPANY, INC., New York. 1947.
- [69] R.E. Collin. *Foundations for Microwave Engineering* (Second Edition-2000). Wiley-IEEE Press.
- [70] H. Kollmus, M.C. Bellachioma, M. bender, A. Kraämer, J.Kurdal and H. Reich-Sprenger. *Vacuum Issues of SIS18 Upgrade at GSI*. In Proc. of EPAC06, Edinburgh, Scotland, 2006.
- [71] C. Omet. *Kollimatorsystem zur Stabilisierung des dynamischen Restgasdruckes im Schwerionensynchrotron SIS18*. PhD thesis, Technische Universität Darmstadt, 2008.
- [72] O. Boine-Frankenheim. *Introduction to the physics of high current ion beam in accelerator and storage rings*. <http://www-linux.gsi.de/boine/vorlesung/skript/sso1.ps/>, 2001. GSI, Darmstadt.
- [73] A. Parfenova. *Linear and Nonlinear Matrix and its Application to the SIS18 Synchrotron*. Johann Wolfgang Goethe Universität in Frankfurt am Main, 2008.
- [74] O. Chorniy. *Measurement and Interpretation of the Bunched Beam Transfer Function in SIS-18 with Space Charge*. PhD thesis, Technische Universität Darmstadt, 2008.

- [75] S. Paret. *Transverse Schottky Spectra and Beam Transfer Functions of Coasting Ion Beams with Space Charge*. PhD thesis, Technische Universität Darmstadt, 2010.
- [76] G. Franchetti, I. Hofmann, W. Bayer, F. Becker, O. Chorniy, P. Forck, T. Giacomini, M. Kirk, T. Mohite, C. Omet, A. Parfenova, P. Schütt. *A Proof-of-principle Experiment on Space Charge Driven Nonlinear Resonance Trapping in the SIS18 Synchrotron*. Phys. Rev. ST Accel. Beams 13, 114203, 2010.
- [77] U. Blell, J. Florenkowski, U. Kopf, C. Mühle, M. Petryk, I. Petzenhauser, P. Spiller, A. Batrakov, S.A. Onischenko, G.E. Ozur. *Development of the injection and extraction systems for the upgrade of SIS18*. In Proc. of PAC07, Albuquerque, New Mexico, United States of America, 2007.
- [78] B.W. Montague. *Basic Hamiltonian Mechanics*. CAS - CERN Accelerator School: 5th Advanced Accelerator Physics Course, Rhodes, Greece, 20 Sep - 1 Oct1993, pp.1-14.
- [79] M. Weiss. *A Short Demonstration of Liouville's Theorem*. CERN 87-10, CERN Accelerator School on Advanced Accelerator Physics, Denmark, 1986, pp.162-163.
- [80] K.P. Ningel, RF Synchrotron Group, GSI. *Private communications*.
- [81] C. Ohmori, E. Ezura, M. Fujieda, Y. Mori, R. Muramatsu, H. Nakayama, Y. Sato, A. Takagi, M. Toda, T. Uesugi, M. Yamamoto, and M. Yoshii, KEK, M. Kanazawa and K. Noda, NIRS. *High Field-Gradient Cavities Loaded With Magnetic Alloys For Synchrotrons*. Proceedings of the 1999 Particle Accelerator Conference, New York, 1999.
- [82] H. Koziol. *Beam Diagnostics for Accelerators*. CAS - CERN Accelerator School: 5th General Accelerator Physics Course, Jyväskylä, Finland, 7 - 18 Sep1992, pp.565-599.
- [83] P. Forck. *Lecture Notes on Beam Instrumentation and Diagnostics*. Joint University Accelerator School. Jan- Mar2009.
- [84] H. Reeg, GSI. *Private communication*.
- [85] H. Reeg, N. Schneider. *Current Transformers for GSI's KeV/u to GeV/u Ion Beams-an Overview*. In Proc. of DIPAC01-ESRF, Grenoble, 2001.
- [86] K. Unser. *Beam Current Transformer with D.C. to 200MHz Range*. IEEE Trans. Nucl. Sci., 3rd IEEE Particle Accelerator Conference, Washington, USA, 5-7 March1969, pp.934-938.
- [87] K. Unser. *A Toroidal DC Beam Current Transformer With High Resolution*. IEEE Trans. Nucl. Sci., NS-28, June1981, pp.2344-46.
- [88] P. Kowina, W. Kaufmann, J. Schölles and M. Schwickert, GSI. *Optimization of "Shoe-Box Type" Beam Position Monitors Using The Finite Elements Methods*. Proc. of DIPAC05, Lyon, pp. 114, 2005.

-
- [89] P. Moritz. LINAC RF group, GSI. *Private communication*.
- [90] Uwe Schaaf. *Schottky-Diagnose und BTF- Messungen an gekühlten Strahlen im Schwerionenspeicherung ESR*. PhD thesis, Univesität Frankfurt, 1991.
- [91] R.E. Schafer. *Characterstic of direction coupler beam position monitors*. Transactions on Nuclear Science, NS-32, 1985.
- [92] Tektronix. User Manual, RSA3303A.
- [93] F. Caspar, CERN. *Private communication* during CAS, Daresbury, Oct2007.
- [94] Mathematica: <http://www.wolfram.com/products/mathematica/index.html>
- [95] D. Boussard. *Schottky Noise and Beam Transfer Funtion Diagnostics*. Proc. CERN Accelerator School, Oxford, 1985, CERN 97-03 (1997).
- [96] K.P. Ningel. Synchrotron RF Group, GSI. *Private communication*.
- [97] M. Bousonville, GSI, Darmstadt, P. Meissner, TU Darmstadt. *RF Reference Signal Distribution System for FAIR*. Proceedings of EPAC08, Genoa, Italy.
- [98] H. Klingbeil. *Digitale Kavitätensynchronisation*. GSI internal note, version1.10, GSI, Darmstadt, 2004.
- [99] H. Klingbeil. *A Fast DSP-Based Phase Detector for Closed-Loop RF Control in Synchrotrons*. IEEE Trans. Inst. Meas., Vol. 54, 2005, pp.1209-13.
- [100] G. Dôme. *RF Theory*. CERN Accelerator School: RF Engineering for Particle Accelerators, Oxford, UK, 3 - 10 April 1991, pp.01-96.

Acknowledgements

I express my sincere thanks to Prof.Dr.T.Weiland for accepting me as a PhD student. It is indeed a great privilege to be his student.

I am indebted to Deutscher Akademischer Austausch Dienst (DAAD) for providing the financial support through DAAD-Helmholtz foundation throughout this work.

I express my deep sense of gratitude to Prof.Dr.I.Hofmann for arranging the financial support, through DAAD-Helmholtz foundation, for this PhD work. I am thankful for his great patience and valuable guidance at critical junctures.

Words are inadequate to express my sincere thanks to Dr.P.Hülsmann for his consistent and invaluable support. His precious guidance helped me a lot to capture the key concepts and develop meaningful insights especially in the experimental part of this studies. I regard his great patience throughout the course of this work.

My special thanks goes to Prof.Dr.O.Boine-Frankenheim for his constructive criticism and useful suggestions, which helped me a lot in developing meaningful understanding in theoretical aspects of accelerator physics. During the supervision of my M.Tech. project, he has motivated and enlighten me by giving an insight in this entirely new field of accelerator physics for me.

A special big thanks to Prof.Dr.J.MacLachlan, from Fermi National Laboratory, USA, for his remote but prompt support in working with ESME. Our mutual communication helped me a lot in solving critical problems in simulating the longitudinal collective effects in ESME.

My sincere thanks to Dr.F.Casper and Dr.A.Hofmann for the precious discussions during CERN Accelerator School and afterwards. Those discussions provided really distinctive inputs to this work.

Many thanks are addressed to Dr.H.Klingbeil for giving me an opportunity to perform the experimental part of the studies. Being leader of the Synchrotron-RF group, he managed to provide a friendly and comfortable working environment for me.

I feel highly indebted to Dr.O.Chorniy for his constant technical support and deep concern throughout this work and for his time to read and comment on chapter drafts.

I owe a lot to Dr.K.P.Ningel for his active involvement in arrangement of machine experiments. Without his support it was impossibly difficult to conduct the experiments.

This report is especially benefitted a lot from the many insightful remarks and suggestions from Dr.U.Laier.

Much thanks to Dr.H.G.König for providing me the access to test cavity and regards for

his great patience in entertaining my infinite number of queries.

I would also like to thank Dr.B.Zipfel for his involvement in the experiments and for his precious and timely suggestions.

My special thanks goes to all my colleagues who took the time to share their ideas or correspond with me along the way, including Dr.G.Franchetti, Ms.M.Mehler, Dr.G.Schreiber, Dr.M.Kirk, Dr.S.Paret, Mr.M.Zelensky, Mr.R.Balß, Mr.T.Winnefeld, Dr.E.Mustafin, Dr.C.Dimopoulou, Dr.A.Parfenova, Ms.A.Mierau, Mr.Gopenath, Mr. R.Singh and Ms.S.Appel.

I would like to acknowledge many GSI and TEMF colleagues for their fast and competent response to any scientific, technical, administrative and computer related problems.

I am grateful to Dr.P.Forck, Dr.P.Kowina, Mr.P.Moritz and specially to Mr.H.Reeg for providing me the key information about the beam diagnostics.

I am thankful to Dr.P.Spiller for providing the beam time for the experiments. For setting up the synchrotron for the measurements, I thank Dr.U.Scheeler, Dr.P.Schütt, Dr.W.Bayer, people from the synchrotron operation group and the operators.

A special mention deserves my mother and other family members for their constant encouragement and moral support. A heartily thanks goes to my friends Ms.Heike Recktenwald and Mr.Uwe Minde for their unconditional moral support and for always being there for me and my family during this crucial period of last few years.

Being a young mother, soon this project was transformed into a family project, which was impossible to be accomplished without the commitment of my husband, Mr. S.S.Mohite, and an uncommon maturity of my little angel 'Dhruv'.

Erklärung

Gemäß §9 der Promotionsordnung der TU Darmstadt

Ich versichere, dass ich die vorliegende Dissertation selbstständig und nur unter Verwendung der angegebenen Quellen verfasst habe. Die Arbeit hat bisher noch nicht zu Prüfungszwecken gedient.
